UNIVERSITÀ DEGLI STUDI DELLA TUSCIA DI VITERBO

Department for Innovation in Biological, Agro-Food and Forest System

DIBAF

PhD in Forest Ecology - Cycle XVIII

Monitoring productivity of plant ecosystems: integration of optical, flux and ecophysiological measurements

AGR/05

Candidate

Enrica Nestola

Signature…………….

PhD Coordinator

Prof. Paolo De Angelis

Signature…………….

Supervisor

Dr. Carlo Calfapietra

Signature ……………

A.A. 2016/2017

Contents

Abstract

1. General Introduction……………………………………………………………………1
   - 1.1 Eddy covariance…………………………………………………...………………….…3
   - 1.2 Optical sampling: Remote and Proximal Sensing………………………...……….…..4
   - 1.3 Ecophysiological techniques ……………………………………..…………..…8
   - 1.4 State of the art…………………………………………………...……….....…10
   - 1.5 Objectives and thesis structure…………..……………………………...…………11
2. Monitoring grassland seasonal carbon dynamics, by integrating optical and eddy covariance measurements
   - 2.1 Introduction………………………………………………………………..………13
   - 2.2 Materials and Methods……………………………………..……………………..16
     - 2.2.1 Study Site and Experimental Design…………………..……………………..16
     - 2.2.2 NDVI Measurements……………………………..……………………..18
       - 2.2.2.1 NDVI $_{680,800}$ from spectrometer measurements……………….………18
       - 2.2.2.2 Proxy NDVI Measurements……………………………….………..19
       - 2.2.2.3 MODIS NDVI Measurements……………………………….……...…21
     - 2.2.3 CO$_2$ Flux Measurements…………………………………….……......22
     - 2.2.4 Biomass estimation……………………………………………….………..23
     - 2.2.5 fAPAR and APAR calibration………………………………….…………24
     - 2.2.6 Filtering and Averaging Process…………………………………….….….25
     - 2.2.7 Gap Filling…………………………...………………….………25
   - 2.3 Results..…………………….…………………………...…………….……...26
   - 2.4 Discussions……………………..………………..……………………………... 33
   - 2.5 Conclusions……………...……………………………………………….……..38
3. Optical indices combined with carbon fluxes, fluorescence-based parameters and pigment analyses for the description of a *Fagus sylvatica L.* forest
   - 3.1 Introduction……………………..……………………………………….………40
   - 3.2 Materials and Methods…………………………………………………………….42
     - 3.2.1 Study site and experimental design……………….………...………………...42
     - 3.2.2 Flux measurements and meteorological data……………………………………43
     - 3.2.3 Optical measurements………………………………………………………44
     - 3.2.4 Leaf level measurements……………..…………………………….…………47

3.2.4.1 Fluorescence measurements……………………………………………47
3.2.4.2 Pigment determinations……………………………………………48
3.2.4.3 Leaf nitrogen content……………………………………………49
3.2.5 Data analysis……………………………………………49
3.3 Results and Discussions……………………………………………50
3.3.1 Characterization of meteorological variables, temporal patterns of fluxes, pigment and fluorescence measurements……………………………………………50
3.3.2. Relations between spectral indices and NEE, pigment concentration, fluorescence parameters and nitrogen……………………………………………61
3.3.3. Carotenoid spectral indices as indicators of stress and senescence………………69
3.4 Conclusions……………………………………………72

4. Validation of three fAPAR products in a deciduous beech forest site in Italy

4.1. Introduction……………………………………………74
4.2. Remote sensing product……………………………………………76
4.2.1 GEOV1……………………………………………77
4.2.2 MODIS C5……………………………………………77
4.2.3 MODIS C6……………………………………………78
4.3. Materials and Methods……………………………………………78
4.3.1. Study site……………………………………………78
4.3.2. Temporal and spatial sampling……………………………………………78
4.3.3. Ground measurements and Instruments……………………………………………81
4.3.3.1. PAR measurements from Apogee……………………………………………81
4.3.3.2. PAR Measurements from PASTIS……………………………………………81
4.3.3.3. Gap fraction estimation from DHP……………………………………………81
4.3.4. Calculation of ground fAPAR……………………………………………83
4.3.4.1. Estimation of fAPAR from Apogee (fAPAR$_{APOGEE}$)……………………83
4.3.4.2. Estimation of fAPAR from PASTIS (fAPAR$_{PASTIS}$)……………………83
4.3.4.3. Estimation of fAPAR from DHPs……………………………………………84
4.3.5. Validation approach……………………………………………84
4.3.5.1. Empirical transfer function……………………………………………85
4.3.5.2 Spatial Aggregation……………………………………………87
4.3.5.3 Correlation analysis……………………………………………88
4.4. Results……………………………………………89
4.4.1. Consistency of ground fAPAR estimates……………………………………………89

4.4.2. High-resolution ground-based maps……………………………………….…….92
4.4.3. Validation of satellite fAPAR products…………………………………….……94
4.4.3.1 Temporal consistency………………………………………………….………94
4.4.3.2 Accuracy Assessment………………………………………………….………95
4.5. Discussion……………………………………………………………………….……..96
4.5.1. Consistency of ground fAPAR estimates…………………………………….……..97
4.5.2. Accuracy Assessment…………………………………………………………….……98
4.6. Conclusions……………………………………………………...………………..98
General conclusions…………………………………………………………………………100
Acknowledgments……………………………………………………………………………..102
References…………...……………………………………………………………………...103

Abstract

Monitoring productivity of plant ecosystems is essential to evaluate the response of different ecosystems to ongoing disturbance and climate change. Always more studies focus on the integration of different techniques for monitoring ecosystems dynamics. Eddy covariance greatly improved the understanding of carbon exchanges between terrestrial ecosystems and the atmosphere. At the same time, the advent of remote sensing offered new possibilities for monitoring broader vegetation patterns over continental regions and yearly timescale. Between these two widespread approaches, the integration of proximal sensing within the flux tower sites currently represents a tool to understand physiological details operating at finer temporal and spatial scales. In any case, ground truthing at the experimental sites keep providing a critical validation of different techniques across biomes. The general aim of this research is exploiting the combination of different methodologies to describe vegetation productivity and plant status using mainly three approaches: 1) eddy covariance technique, 2) remote and proximal sensing and 3) field sampling. The research is carried out in two very different ecosystems, a grassland site in Alberta, Canada and a deciduous broadleaf forest in central Italy. The specific objectives of the study are to: 1) evaluate the seasonal productivity of the prairie grassland using a combination of remote sensing, eddy covariance, and field sampling (Chapter 2); 2) investigate the functionality of the deciduous broadleaf forest using simultaneous determinations of optical measurements, carbon flux data, leaf eco-physiological and biochemical traits during two growing season with different meteorological conditions (Chapter 3) and 3) validate three fAPAR (the fraction of photosynthetically active radiation absorbed) satellite products against ground fAPAR references to determine their accuracy in the deciduous beech forest site (Chapter 4).

In Chapter 2, we evaluated different ways of parameterizing the light-use efficiency (LUE) model for assessing net ecosystem fluxes at a two grassland sites in Alberta during 2012 and 2013. Three variations on the NDVI (Normalized Difference Vegetation Index), differing by formula and footprint, were derived and all three NDVIs provided good estimates of dry green biomass, confirming their utility as metrics of productivity. NDVI values from the different methods were also calibrated against fAPARgreen (the fraction of photosynthetically active radiation absorbed by green vegetation) measurements to parameterize the APARgreen (absorbed PAR) term of the LUE (light use efficiency) model for comparison with measured fluxes. The best results were obtained by splitting the data into two stages, a greening and senescence phase, and applying separate fits to these two periods. By incorporating the dynamic irradiance regime, the model based on APARgreen rather than NDVI best captured the high variability of the fluxes and provided a more realistic depiction of missing fluxes.

The experiment presented in Chapter 3, was carried out in the Mediterranean beech (*Fagus sylvatica* L.) forest of Collelongo and is focused on two growing seasons (2014-2015) having different meteorological conditions, with July 2015 characterized by higher monthly temperature and reduced precipitations compared to July 2014. Spectral indices computed at canopy level were used to track changes in CO_2 fluxes and in the physiological status. Mainly optical indices related to structure were found to better track carbon fluxes variation for both 2014 and 2015, thus suggesting that structural parameters are essential drivers at the forest site. Moreover, seasonal patterns of chlorophylls (Chl a and Chl b), carotenoids (b-carotene, lutein, neoxanthin and xanthophyll cycle components) and fluorescence parameters were investigated to evaluate which optical indices better predict changes in photosynthetic pigment levels and energy dissipation mechanisms. Optical indices related to carotenoids composition were indicators of the shifting pigment composition related to stress (July) and senescence (October) during 2015. Thus, spectral indices resulted to be reliable proxies for monitoring carbon fluxes and vegetation dynamics in healthy and stressed vegetation.

Chapter 4 was aimed to validate three fAPAR satellite products, GEOV1, MODIS C5, and MODIS C6, against ground references at the same beech forest in Italy during 2014 and 2015. Three ground reference fAPAR, differing for temporal (continuous or campaign mode) and spatial sampling (single points or Elementary Sampling Units-ESUs), were collected using different devices: 1) Apogee (defined as benchmark in this study); 2) PASTIS; and 3) Digital cameras for collecting hemispherical photographs (DHP). A bottom-up approach for the upscaling process was used. Radiometric values of satellite images were extracted over the ESUs and used to develop empirical transfer functions for upscaling the ground measurements. The resulting high-resolution ground-based maps were aggregated to the spatial resolution of the satellite product to be validated considering the equivalent point spread function of the satellite sensors, and a correlation analysis was performed to accomplish the accuracy assessment. The temporal courses of the three satellite products were found to be consistent with both Apogee and PASTIS, except at the end of the summer season when ground data were more affected by senescent leaves, with both MODIS C5 and C6 displaying larger short-term variability due to their shorter temporal composite period. The three green fAPAR satellite products under study showed good agreement with ground-based maps of canopy fAPAR at 10 h and very low systematic differences.

1. General introduction

Carbon cycle topic is the common denominator of ecology, oceanography and geochemistry researches due to its central role in the biogeochemical processes. Terrestrial biosphere plays an important role in the global carbon cycle whereas carbon is removed from the atmosphere via photosynthesis by plants [1]. The process by which plants use sunlight to produce organic matter from carbon dioxide through photosynthesis is defined as vegetation productivity [2]. Ecosystems carbon dynamics are extremely important in the context of climate change due to their capacity to control the Earth system in a globally significant way [3]. In fact, terrestrial ecosystems can release or absorb relevant greenhouse gases such as carbon dioxide (CO_2), methane and nitrous oxide and control exchanges of energy and water between the atmosphere and the land surface [4]. Considerable amounts of carbon are stored in living vegetation and soil organic matter, and release of this carbon into the atmosphere as CO_2 would critically impact the global climate [4]. The biogeochemical carbon cycle in the ocean and on land will likely continue to respond to climate change and rising atmospheric CO_2 concentrations created during the 21st century [5]. Thus, the link between carbon cycle and global climate change highlights the importance of studying plant ecosystems, not only for their essential role as a carbon sink, but also because climate extremes can potentially impact terrestrial ecosystems causing a shift from a carbon sink towards a carbon source [6].

An area may be a carbon sink if carbon is stored faster than it is being released. Differently, an area is called carbon source if the production of atmospheric carbon from that area exceeds the rate at which carbon is being fixed there. In terrestrial ecosystems, whether an area is a sink or a source depends mostly on the balance between the rate of photosynthesis and the combined rate of respiration and burning [7]. Their role in carbon sequestration varies as the plants have the ability to act as either a carbon sink by removing carbon or as a source by donating carbon to the atmosphere [8]. Ecosystems capacity of acting as carbon sink changes depending on vegetation type. In 2009, the United Nations Environment Programme (UNEP) produced a detailed summary that show the amount of carbon stored (t C/ha) by the different natural ecosystems (Figure 1.1). Ecosystems as tundra and boreal forest are dense in C, which is mainly accumulated in the soil pool, particularly in the permafrost layer for tundra and in soil and litter for boreal forest. The temperate forests, where vegetation growing and decomposition is rapid, have been estimated to store between 150 and 320 tonnes per hectare [9] (Figure 1.1). About the 60% of the carbon stored by this biome is constituted by plant biomass, principally in the form of large woody above-ground organs and deep root systems [9].

Interestingly, Janssens et al. [10] found that European temperate forests are estimated to be taking up 7–12% of European carbon emissions, thus highlighting the potentiality of this kind of ecosystem. Nevertheless, persistent droughts, disturbances such as fire and insect outbreaks, worsened by climate extremes and climate change put the mitigation benefits of the forests at risk [11].

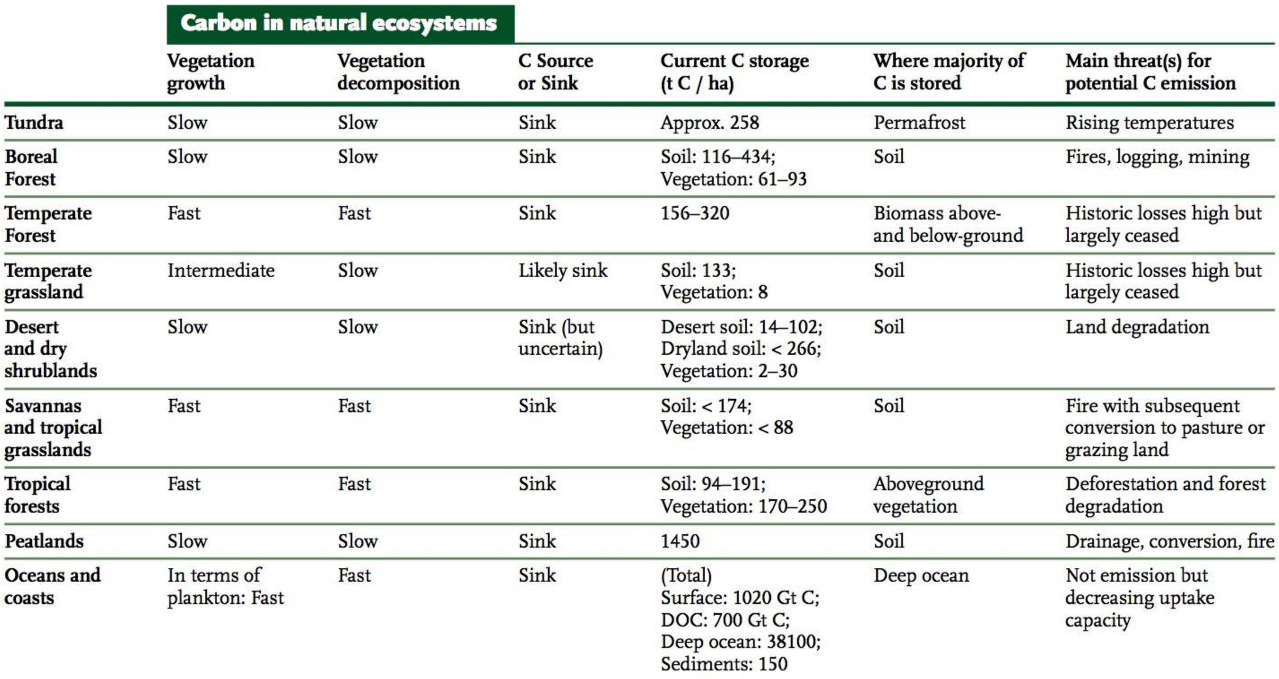

Carbon in natural ecosystems

	Vegetation growth	Vegetation decomposition	C Source or Sink	Current C storage (t C / ha)	Where majority of C is stored	Main threat(s) for potential C emission
Tundra	Slow	Slow	Sink	Approx. 258	Permafrost	Rising temperatures
Boreal Forest	Slow	Slow	Sink	Soil: 116–434; Vegetation: 61–93	Soil	Fires, logging, mining
Temperate Forest	Fast	Fast	Sink	156–320	Biomass above- and below-ground	Historic losses high but largely ceased
Temperate grassland	Intermediate	Slow	Likely sink	Soil: 133; Vegetation: 8	Soil	Historic losses high but largely ceased
Desert and dry shrublands	Slow	Slow	Sink (but uncertain)	Desert soil: 14–102; Dryland soil: < 266; Vegetation: 2–30	Soil	Land degradation
Savannas and tropical grasslands	Fast	Fast	Sink	Soil: < 174; Vegetation: < 88	Soil	Fire with subsequent conversion to pasture or grazing land
Tropical forests	Fast	Fast	Sink	Soil: 94–191; Vegetation: 170–250	Aboveground vegetation	Deforestation and forest degradation
Peatlands	Slow	Slow	Sink	1450	Soil	Drainage, conversion, fire
Oceans and coasts	In terms of plankton: Fast	Fast	Sink	(Total) Surface: 1020 Gt C; DOC: 700 Gt C; Deep ocean: 38100; Sediments: 150	Deep ocean	Not emission but decreasing uptake capacity

Figure 1.1. Summary of vegetation growth, decomposition, carbon storage and main threats linked to potential C emissions for main natural ecosystems. From Trumper et al. [7].

Differently from the forests, temperate grasslands are moisture and nutrient limited and allocate much of their biomass below ground. Climate change and CO_2 may affect grazing systems by altering species composition; for example, warming will favour tropical (C4) species over temperate (C3) species but CO_2 increase would favour C3 grasses [12]. However, despite grasslands have low levels of plant biomass, their soil organic carbon stocks tend to be higher than those of temperate forests [9]. In ecosystems like desert and dry shrublands, water represent the limiting factor and determines the way in which carbon is processed. While carbon stored is typically lower in the vegetation (2–30 tonnes of carbon per ha), Wohlfahrt et al. [13] suggested that carbon uptake by deserts is much higher than previously thought and that it contributes significantly to the terrestrial carbon sink. Savannas cover large areas of Africa and South America and can store significant amounts of carbon, especially in their soils. The trend and interannual variability of CO_2 uptake by terrestrial ecosystems are dominated by semiarid ecosystems whose carbon balance is strongly associated with circulation-driven variations in both precipitation and temperature [14]. Lastly, the largest terrestrial carbon store is held by tropical forest, where most of the carbon can be found in the vegetation and biomass estimates reaches 170–250 t C per ha [15]. Nepstad et al., [16] informed that predicted changes in temperature, rainfall regimes, and hydrology may promote the dieback of tropical forests. A matching example is the prolonged drought conditions in the Amazon region during 2005 that contributed to a decline in above-ground biomass and triggered a release of 4.40 to 5.87 GtCO2 [17].

Anthropogenic CO_2 emissions to the atmosphere were 555 ± 85 PgC (1 PgC = 1015 gC) between 1750 and 2011. Of this amount, fossil fuel combustion and cement production contributed 375 ± 30 PgC and land use change (including deforestation, afforestation and reforestation) contributed 180 ± 80 PgC [5]. Canadell et al. [18] informed that the land sinks of carbon absorb close to one-third of anthropogenic emissions; hence, monitoring terrestrial ecosystems using the latest technical methods is crucial for maintaining the significant potentiality of reducing future emissions of greenhouse gases [19]. Accurate estimates of plant productivity across space and time are thus necessary for quantifying carbon balances at regional to global scales.

Currently, the most renowned methods used for continuous monitoring ecosystem productivity are eddy covariance (EC) technique and remote sensing [20] while ecophysiological techniques have been widely used in the past as non-continuous monitoring of carbon dioxide (CO_2). Below, the methods used in this work for studying plant ecosystems chosen as experimental sites are briefly presented.

1.2 Eddy covariance

Terrestrial gross primary production (GPP) is the entry point of atmospheric CO_2 into the terrestrial ecosystem and it refers to the amount of carbohydrate produced through photosynthesis in a given period of time over a unit area [21]. About half of the carbohydrates are employed by plants for growth and maintenance (autotrophic respiration) [22]. When autotrophic respiration is subtracted from GPP, then the net carbon gain by vegetation (NPP) is obtained [22]. NPP is a key variable for environmental monitoring and is a sensitive indicator of climate change [23]. Besides autotrophic respiration, plants loose carbon through heterotrophic respiration, when heterotrophic organism eat live or dead organic matter and release CO_2 to the atmosphere. When also the heterotrophic respiration is subtracted by NPP, we refer to the net ecosystem productivity (NEP) which has an ecological relevance as it represents the net amount of carbon stored by an ecosystem [22]. NEP can be also expressed as net ecosystem exchange (NEE) which refers to the net CO_2 exchange with the atmosphere [24]. Song et al. [21] inform that ecosystem services base on NPP are multiple as for example food, shelter for wildlife, fiber for human society and the aforementioned potentiality for mitigating climate change. For this reason, during the last decades, the need of continuously and accurately track C dynamics became more and more important. In this context, during the last 30 years, the eddy covariance technique emerged as one of the most accurate approaches to measure gas fluxes over large areas. Eddy covariance allows the direct in-situ measurement of carbon exchange between plant canopy and the atmosphere [25]. The concept behind the method is that the atmosphere contains turbulent motions of upward and downward moving air that transport trace gases (e.g., CO_2). Therefore, the eddy covariance technique samples these turbulent motions to determine the net difference of material moving across the canopy atmosphere interface [24]. Specifically, this technique allows to acquire high frequency (10-20 Hz) measurements of wind speed and direction as well as CO_2 and H_2O concentrations at a point over the canopy using a three-axis sonic anemometer and a fast response infrared gas analyzer [26,27]. Flux measurements are typically integrated over periods of half an hour building the basis to calculate carbon and water balances from daily to annual time scales [28].

The widespread use of eddy covariance depended of mainly four reasons: 1) it is a scale appropriate method that assess net CO_2 exchange of a whole ecosystem; 2) it provides direct measurements of net carbon exchange across the canopy-atmosphere interface; 3) it provides measurements having a wide spatial (from hundreds of meters to several kilometers) and temporal scale (continuous measurements from hours to years) [24]. On the other hand, eddy covariance technique is affected by several sources of errors and uncertainties that can be summarized as 1) varying footprints if the ecosystem is inhomogeneous and patchy, 2) instrumentation errors (e.g., acquisition frequency, sensor separation), 3) underestimation of NEE during periods with low turbulence [28].

1.3 Optical sampling: Remote and Proximal Sensing

Optical sampling techniques take advantage of optical properties (reflected or emitted electromagnetic radiation) of a determined surface area using non-contact devices. Three main physical mechanisms may occur when incident radiation interacts with canopy elements: absorption reflection and transmission [29]. For any given material, the amount of solar radiation that is reflected varies with wavelength. When the response (reflectance) characteristics of a certain cover type is plotted against wavelength, this plot is termed the spectral signature of that cover [30]. As most of the diagnostic absorption features of green vegetation are located between 380 and 2500 nm of the spectrum, the solar reflected radiation in the optical domain is commonly used in vegetation studies (Figure 1.2) [31,32]. Reflectance of vegetation canopies depends on radiative properties of leaves, other non-photosynthetic canopy elements and their spatial organization. Homolová et al. [29] clearly summarize the main characteristic of leaf reflectance spectra as 1) strong and well described absorption of foliar photosynthetic pigments, dominated by chlorophylls, in the visible region (400-700 nm, VIS), 2) leaf structure in the near infrared region (700-1300 nm, NIR), and 3) prevailing water and protein absorptions in the shortwave infrared region (1300-2500 nm, SWIR or middle infrared).

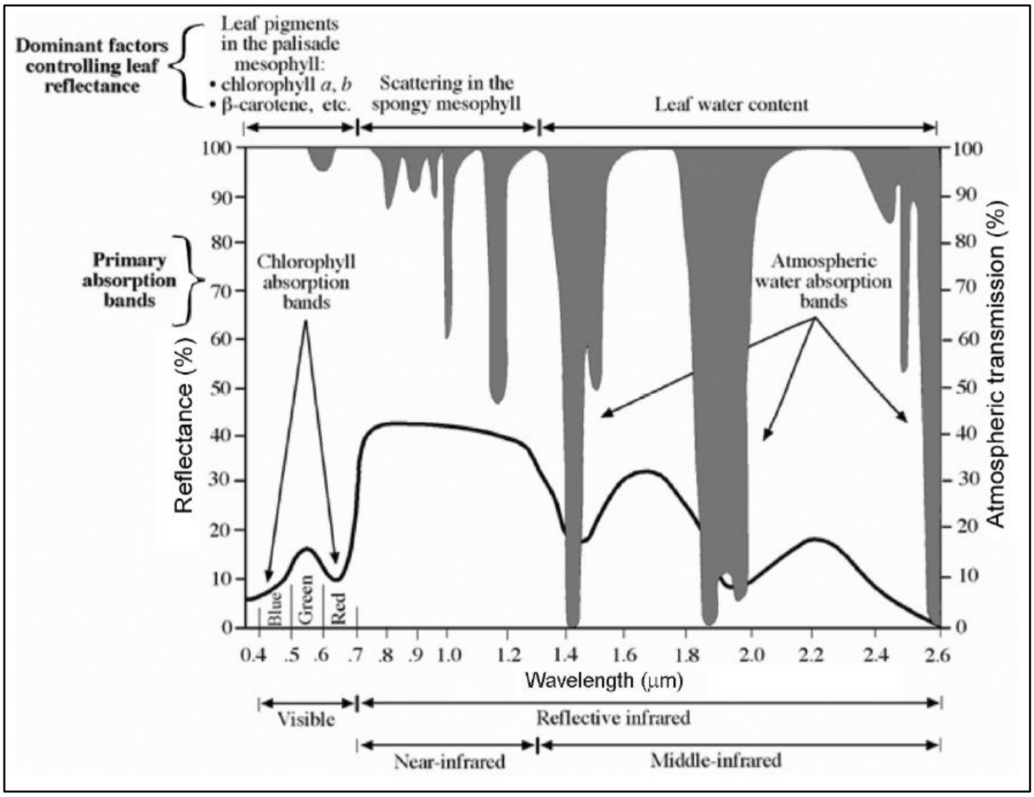

Figure 1.2. Typical spectral signature of leaf and dominant factor controlling leaf reflectance. From Jensen et al. [33].

In particular, in the VIS region, absorption by leaf pigments is the most important process leading to low reflectance values. The main light-absorbing pigments are chlorophyll a and b, carotenoids, xanthophylls and all pigments have overlapping absorption features. Chl a displays maximum absorption in the 410-430 nm (blue) and 600-690 nm regions (red), whereas Chl b shows maximum absorption in the 450-470 nm range (blue). These strong absorption bands induce a reflectance peak in the green domain at about 550 nm. Moreover, carotenoids (Car) absorb most efficiently between 440 and 480 nm (Figure 1.2) [34]. Car absorption waveband overlapping with Chl and lower content of Car than Chl content are the two main obstacles in Car estimation through optical sampling [35].

In the NIR region, the absorption is very low and reflectance reach their maximum values (about 50% in green health leaves), which is largely the result of photon scattering within the leaf tissue at the air-cell interfaces of the mesophyll [36]. The level of reflectance on the NIR domain increases with increasing number of cell layers, cell size and aerial interspaces in the leaf mesophyll. Scattering occurs mainly due to multiple refractions and reflections at the boundary between the hydrated cellular walls and air spaces [37]. In SWIR, leaf optical properties are mainly affected by the water absorption bands that occur at 1450, 1940 and 2700 nm [38]. Among them, the features at 1450 and 1950 nm are the most pronounced. However, strong water vapor absorption in the atmosphere reduces the effectiveness of these spectral information to essentially zero [39]. Protein, cellulose, lignin and starch also influence leaf reflectance in the SWIR [34].

Additionally, both green edge (490-530 nm) and red edge (680-750 nm) regions are widely recognized as two very informative features of the vegetation reflectance [40]. The green edge is a transition region where in situ absorption by Chl a and b and different Car drops sharply from a high value at 480 nm to an almost negligible amount above 531 nm [35]. On the other hand, the red edge region corresponds to the rise of reflectance at the boundary between the chlorophyll absorption feature in the red wavelengths and leaf scattering in the NIR wavelengths [40].

The spectral response of vegetated areas have been widely exploited to develop vegetation indices (VIs). An index is a number qualifying the intensity of a phenomenon which is too complex to be decomposed into known parameters. Accordingly, vegetation indices use a combination of spectral reflectance in different bands for qualitatively and quantitatively evaluating vegetative status using spectral measurements [41]. The advantage of vegetation indices is that they allow obtaining relevant information in a fast and easy way and that the underlying mechanisms are well-understood. [42]. One of the most widely known indices is the Normalized Difference Vegetation Index (NDVI) [43]. It expresses the normalized ratio between the reflected energy in the red chlorophyll absorption region and the reflected energy in the NIR providing an indicator of the ‘greenness’ of the vegetation [44,45]. Likewise, the VIs formulated as combination of red edge bands are frequently employed in plant status assessment. In fact, both the green and red edge regions are important for computation of vegetation indices since they remain sensitive to changes pigment content, reducing the saturation effect and enhancing the sensitivity to moderate-high vegetation densities [46,47].

Balzarolo et al. [48] informed that sensors for optical measurements could be classified into three categories, depending to their spectral bandwidth across the sampled spectrum: (1 broad-band multispectral sensors; (2 narrow-band multispectral sensors; and (3 hyperspectral sensors. Particularly, the broad-band multispectral sensors capture data in a few wavelength channels (bandwidth > 10 nm), the narrow-band multispectral sensors offer fine spectral resolution data (e.g., bandwidth ≤ 10 nm) in a few targeted bands instruments, and lastly the hyperspectral sensors measure in very narrow and contiguous (overlapping) channels and can be used to provide more detailed information in the wavelength domain. Consequently, while multispectral system commonly collect data in two to six spectral bands in a single observation, hyperspectral system collect several hundred spectral bands in a single acquisition, thus producing more detailed spectral data [49]. Furthermore, multispectral sensors are characterized by relatively low cost, easy maintenance, and low power consumption, and are hence useful tool for long-term unmanned field measurements. Conversely, hyperspectral devices are more expensive and thus are generally considered less suitable for long-term, automated deployment in the field without additional modifications for unattended use [50].

Both remote sensing (RS) and proximal sensing (PS) are based on the optical properties of vegetation. When we refer to remote and proximal sensing we indicate the practice of obtaining information about an object, area, or phenomenon through the analysis of data acquired by a device that is not in contact with the object, area, or phenomenon under investigation [51].

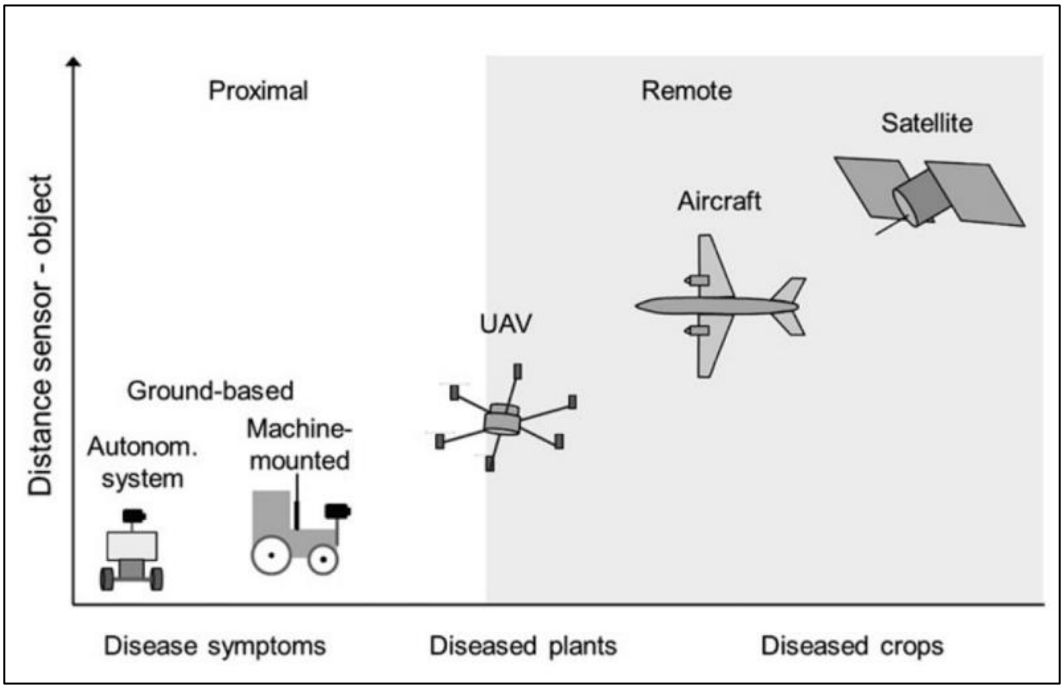

Figure 1.3. Example of proximal and remote sensors and relative distance between sensor and objects of study. From Gullino et al. [52].

The first main difference is that, for RS, the sensor is distant from the object of study by a scale equal to or greater than kilometers while in PS the distance from the sensor to the object of study is on the scale of meters (Figure 1.3) [53]. Moreover, conversely to RS that need geometric and atmosphere corrections, PS can be used without the need of substantial preprocessing of data. Examples of proximal sensors are hand-held, machine mounted or attached to unmanned aerial vehicles (UAVs) whereas satellites, aircraft or UAVs covering larger areas are typical RS platforms. Lastly, PS has a higher spatial resolution (from 10^{-3} to 10^{-2} m) than remote sensing (from 10^{-1} to 10^{2} m) [52].

1.4 Ecophysiological techniques

Revealing the underlying ecophysiological factors governing net ecosystem exchange (NEE) of CO_2 is necessary to strengthen future predictions regarding the role of terrestrial vegetation in the global C balance and potential climatic change [26].

Among the systems used for measuring the photosynthesis at leaf level, those mainly diffused are gas exchange system and fiber optic fluorimeter measuring chlorophyll fluorescence. Gas exchange system provides direct instantaneous, non-destructive measurements of CO_2 concentrations taken up by photosynthesis and H_2O released via transpiration. Particularly, CO_2 exchange systems use enclosure methods, where the leaf is closed in a transparent chamber and the rate of CO_2 fixed by the leaf enclosed is determined by measuring the change in the CO_2 concentration of the air flowing across the chamber [54].

This method involves the use of infrared gas analyzers (IRGAs) that measure the reduction in transmission of infrared wavebands caused by the presence of CO_2 between the radiation source and a detector. Beyond photosynthesis and transpiration, gas exchange systems are able to measure other parameters associated with photosynthesis such as leaf conductance, the intercellular CO_2 mole fraction over a range of conditions that can be manipulated by the researcher [55]. There are mainly two types of gas-exchange systems: closed and open systems. In closed systems, air is continually recycled throughout a system containing a cuvette in which a portion of or a whole plant is placed. Open gas exchange systems have largely replaced the closed systems since when advances in IRGA technology led to the development of commercially available open gas exchange systems. These open systems employ analysis of the gas concentrations in two different chambers: a reference chambers, which has an air stream that is not modified by the presence of a leaf, and a sample chamber, which contains a leaf [56]. Common problems encountered in gas exchange measurements are mainly associated with 1) the fundamentals of the technique, including calibration issue 2) the specific design of the leaf cuvettes used in most commercially available systems and 3) leaf physiology, which are independent of calibration and cuvette designs [55]. However, combining gas-exchange measurements with other techniques allows for an in-depth understanding of numerous processes related to photosynthesis beyond what gas exchange alone can provide.

To maintain energy balance and avoid damage, plants can re-emit excess energy through chlorophyll fluorescence or dissipate it as heat [57]. Chlorophyll fluorescence (Chl F) is one of the most popular techniques in plant physiology because of the easiness with which the user can gain detailed information on the state of photosystem II (PSII) at a relatively low cost. It has had a major role in understanding not just the fundamental mechanisms of photosynthesis but also the responses of plants to environmental change, genetic variation, and ecological diversity [58]. The theory beyond measurements of Chl fluorescence is that the light energy absorbed by chlorophylls associated with PSII can be used to drive photochemistry in which an electron is transferred from the reaction center chlorophyll, P680, to the primary quinone acceptor of PSII, QA. Alternatively, absorbed light energy can be lost from PSII as chlorophyll fluorescence or heat. The processes of photochemistry, chlorophyll fluorescence, and heat loss are in direct competition for excitation energy and these three processes do not exist in isolation but rather in competition with each other [59].

The development of the pulse amplitude-modulated (PAM) technique (an active technique that involves the use of a measuring light and a saturating light pulse) and the subsequent introduction of commercial PAM fluorometers enable the possibility to collect Chl F measurements not just in the laboratory but also in the field [60]. Despite PAM fluorometry has facilitated the study of the acclimation of photosynthesis and helped clarify the link between Chl F and photosynthetic CO_2 assimilation, the technique has been restricted to the leaf level for practical reasons, and thus its applicability at the canopy and landscape levels remains unknown. To fill the gap, a new wave of developments attempt to measure Chl F from remote sensing platforms [61]. The remote sensing technique is based on the passive measurement of solar-induced chlorophyll fluorescence (SIF), taking advantage of the fact that atmospheric absorption bands (e.g., the Fraunhofer lines) contain a small fluorescence signal that can be detected with the appropriate narrow-band instruments, allowing quantification of this small signal against a larger background of solar radiation [62,63]. There are intrinsic differences between the basis of active Chl fluorescence measurement methods based on PAM measurement and that of the SIF; thus, consequent challenges are currently encountered [64]. However, the remote measurement of SIF opens a new perspective to assess actual photosynthesis at larger, ecologically relevant scales and provides an alternative approach to study the terrestrial carbon cycle [65].

1.5 State of the art

Traditional sampling techniques for estimating vegetation conditions based on field collection data (e.g. biomass harvesting, pigment analysis), are time-consuming, costly, and not generally applicable to inaccessible regions [30]. From the 1990s to the present, the eddy covariance approach achieved a resounding success in studying ecosystem physiology. This led to the set-up of several network of flux tower such as Euroflux, Ameriflux, MEDEFLUX (the Mediterranean region), AsiaFlux, and OzNet (Australia) thanks to which scientific community improved the understanding of inter- and intra-annual variations in the carbon fluxes at the ecosystem level. However, it is recognized that flux measurements are subject to several sources of error and limitations. Measurements of flux methods require homogenous vegetation in flat terrain around the towers to produce results that are representative of a particular ecosystem, and these conditions are often not perfectly met in natural landscapes [66]. In addition, the footprint of eddy covariance measurements it is affected by variation depending on wind direction and speed, measurement height, and vegetation structure [67]. Furthermore, while number of experimental sites equipped with eddy covariance tower was constantly increasing during the last decades (more than 500 according to Schimel et al. [68], the distribution of the sites was still too limited for quantifying carbon flux at global scale. In this context, satellite-imaging sensors offered synoptic-scale observations of ecosystems conditions and represented invaluable tools to help fill the large spatial gaps of in situ measurements, improving the accuracies of models. Remote sensing complements the restrictive coverage afforded by experimental plots and eddy covariance measurements, facilitating observations of broad-scale patterns of ecosystem functioning [2]. For this reasons, other networks such as SpecNet or Eurospec endorsed the integration of optical sampling with ecosystem-atmosphere fluxes of carbon dioxide [69,70]. Thus, the combination of these methods to address ecosystem-atmosphere fluxes is a relatively new experience and the advent of new tools (principally improved field spectrometers and sampling platforms) have enabled more detailed optical studies of the flux tower footprint [71]. At the moment, the combination of eddy covariance technique and remote sensing provide a promising means to upscale point measurements taken such as carbon fluxes at the ecosystem level to the regional and global scale [72,73].

Recently, the FLuorescence EXplorer (FLEX) mission selected as the European Space Agency (ESA) 8th Earth Explorer (EE8) started to detect the faint red glow of the Sun-Induced Fluorescence signal (SIF) emitted by plants. The FLEX satellite carries the FLuORescence Imaging Spectrometer (FLORIS) to measure fluorescence at the oxygen absorption bands, the reflectance in the red-edge and the Photochemical Reflectance Index (PRI) [74]. Following the work of the afore mentioned networks (i.e., SpectNet, Eurospec), the current COST Action ES1304 “OPTIMISE” focus on enlarging the ground-truthing spectral networks, standardizing the optical sampling measurements within carbon flux monitoring networks and exploring the measurement and interpretation of multiscale chlorophyll fluorescence data to support satellite fluorescence data. New challenges and future work are mainly linked to present space missions that herald a new range of possibilities for retrieving SIF at the global scale. This could result in improved estimates of the global carbon budget and capacity to track the health of terrestrial ecosystems [61].

1.6 Objectives and thesis structure

The general aim of this research is to take advantage of the combination of different methodologies to better describe vegetation productivity and plant status using mainly 3 approaches: 1) eddy covariance technique, 2) remote and proximal sensing and 3) field sampling. These three approaches represent the common denominator of the study and are shared throughout the different parts of the work. Particularly, the study is organized in 3 parts that are presented after a concise introduction explaining the main characteristics of all the techniques adopted. In Chapter 2, a combination of remote sensing, proximal sensing, eddy covariance, and field sampling are used to monitor the productivity of a typical grassland ecosystem of Northern America. This chapter contribute to the understanding of how optical inputs (both satellite and ground measurements) to a simple empirical Light Use Efficiency model closely track seasonal carbon fluxes and provide a simple proxy to fill gaps in the eddy covariance. Successively, Chapter 3 explores the functionality of a deciduous broadleaf forest in Italy using simultaneously optical sampling, C flux data, leaf eco-physiological and biochemical traits. Spectral indices computed at canopy level were used to track changes in CO_2 fluxes and to detect changes in photosynthetic pigment levels and energy dissipation mechanisms in healthy and stressed vegetation. Besides water, carbon dioxide, and nutrients, plant requires solar radiation in the 400-700 nm range (photosynthetically active radiation or PAR) for photosynthesis. The fraction of PAR absorbed by the vegetation canopy (fAPAR) is therefore an important biophysical variable and is widely used in satellite-based productivity models to estimate gross primary productivity. Chapter 4 presents the validation of three different satellite fAPAR products (PROBA-V GEOV1, MODIS C5 and MODIS C6) against ground references at the same forest site in Italy. Three ground reference fAPAR, differing for temporal and spatial sampling, were collected using different devices (Apogee, PASTIS and DHP) for tracking the seasonal course of fAPAR over the aforementioned deciduous forest, a kind of ecosystem where lack of field data is recognized.

From this overview, it emerges that the three chapter of the thesis are strongly linked by the ecosystem productivity concept. In fact, if on one side, Chapter 2 and Chapter 3 are focused on estimating carbon productivity using optical measurements in different kind of ecosystems, Chapter 4 validates an essential input for photosynthesis modeling. Vegetation productivity is indeed directly related to the interaction of solar radiation with the plant canopy, based on the original logic of Montheith [75], who suggested that productivity was linearly related to vegetation absorbed PAR (light) for photosynthesis. Remotely sensed fAPAR data are widely used as input in carbon productivity models and the fAPAR accuracy is relevant as it has a considerable impact on the fluxes estimated by the model.

2. Monitoring grassland seasonal carbon dynamics, by integrating optical and eddy covariance measurements

2.1. Introduction

The need to better understand and predict future carbon–climate interactions makes the assessment of biosphere-atmosphere carbon exchange for the various biomes of the planet a critical topic for the scientific community and the policy-makers [76]. There is growing interest in assessing biospheric carbon storage with the hope that management regimes can optimize carbon sequestration. Also, soil processes play important role in global climate change as soils have the potential to act as a net sink for CO_2 due to the large amount of carbon currently stored in soil organic matter [77,78]. However, carbon fluxes are inherently dynamic, affected by short-term disturbance and weather events, making evaluation and prediction of carbon storage and climate feedbacks challenging. While much attention has been given to forests for their large feedbacks and carbon sequestration [79], the carbon storage potential of other biomes have been less thoroughly considered, even though many cover large areas, and contribute measurably to overall biospheric carbon uptake and storage.

Rangelands occupy close to 50% of the world’s land area[80],and are defined as lands where indigenous or introduced vegetation is grazed or has the potential to be grazed and are generally considered and managed as natural ecosystems [81]. Rangelands include natural grasslands, savannas, shrublands, deserts, tundra, alpine communities, marshes, and wet meadows [82]. The grassland or prairie biome is particularly important in Canada and in Alberta, as the Grassland Natural Region covers 14.4% of the province [83]. The Dry Mixedgrass Natural Subregion accounts for 47.5% of the Grassland Natural Region area, and thus represents 7% of the area of Alberta province [84]. Grassland provides a number of important services including carbon sequestration and livestock forage. The capacity of grassland ecosystems to sequester carbon is a leading factor in the consideration of policies and practices that maximize carbon storage without compromising managers’ profits [85]. The carbon sequestration of a grassland can vary considerably from year to year since it is influenced both by natural and anthropogenic factors such as temperature, rainfall, species composition, nutrient and water availability, light, grazing pressure and agricultural practices [86,87]. The combination of all these factors makes grasslands considered natural climate change signature ecosystems and so, particularly interesting to be monitored [88–90].

Historically, most attempts to assess ecosystem carbon storage have been based on field sampling of above- and below-ground biomass and carbon, which requires considerable investments in time and personnel [91], and may not capture the temporal dynamics in response to changing conditions.

Ecosystem carbon dynamics have been modeled using different input parameters such as climate [92,93] or soil and nutrient availability [94,95]. However, models often lack spatially or temporally sufficient data inputs, so may not take into account all ecosystem dynamics and interactions.

Significant progress in understanding ecosystem dynamics has been accomplished using the eddy covariance (EC) technique, which quantifies carbon and water vapour fluxes between the biosphere and the atmosphere[96]. This technique has been successfully applied to estimate carbon fluxes in grassland ecosystems [97,98]. Nevertheless, the EC technique is expensive, subject to data gaps, and limited to relatively flat, large landscape regions, so cannot offer universal sampling of fluxes for all locations.

Remote sensing and proximal optical sampling methods can provide cost-effective, uniform samplings under conditions where eddy covariance techniques would be impractical. Satellite remote sensing combined with weather data have been used to model global carbon exchange for many years now, but these current models often disagree with local field measurements due to the coarse scale of their optical and meteorological inputs [99]. For effective carbon policy, fine-grained measurements are needed to match the scale of local land management practices. Recent advances in automation and low-cost optical sensors are making a local-scale optical sensing approach increasingly attractive. Recent studies show that the combined application of remote and proximal optical sensors provide the opportunity to monitor productivity across a wide range of spatial and temporal scales and offer the possibility to relate spectral measurements with carbon fluxes as a foundation for modeling and upscaling [100]. Networks as SpecNet and EUROSPEC have been exploring the possibility of combining flux and spectral measurements[48,69,101]. In this context, models have recently became the bond between remote sensing measurements and carbon fluxes thanks to the increased availability of both information at tower sites. A crucial first step is to evaluate these optical methods in comparison to flux methods to enable proper model parameterization.

The most widely applied model for combining carbon fluxes and optical measurements is the Light Use Efficiency (LUE) model. Originating with the work of Monteith [75,102], more recent parameterizations have been used to estimate gross primary productivity (GPP) based on the equation:

$$GPP = \varepsilon * APAR_{green} \qquad (2.1)$$

Where $APAR_{green}$ (absorbed photosynthetically active radiation) represents the amount of radiation absorbed by green vegetation, and ε represents the efficiency with which that absorbed light is used by vegetation to fix carbon. To obtain annual GPP, the equation terms can be integrated (summed) [72,99].

APARgreen can be further defined or measured as the product of fAPARgreen (the fraction of photosynthetically active radiation absorbed by green vegetation) and PAR (photosynthetically active radiation, also called the photosynthetic photon flux density, or PPFD):

$$APAR_{green} = fAPAR_{green} \times PAR \qquad (2.2)$$

Damm et al. [65] reported that, especially in cropland and grassland, canopy structure and APAR covaries in time during a seasonal cycle. Partitioning between photosynthetic and non-photosynthetic components of vegetation in APAR calculations significantly improve estimation of ecosystem productivity with respect to models driven by total fAPAR [103]. Thus, $APAR_{green}$, a measure of green vegetation structure closely linked to green biomass or leaf area index, plays a dominant role in the model for most grassland ecosystems.

Light use efficiency (ε) relates to vegetation physiology, presumably less important in the case of grasslands and annual systems where canopy growth dominates the seasonal phenological signals detectable with remote sensing [71]. Consequently, most of the variability in grasslands productivity could be explained by changes in APAR [104] when the ecosystem is not stressed [103]. For this reason, the hypothesis of a constant ε over the season (May-October) was adopted in this study.

The strength of the LUE model is related to the possibility of deriving its input values from remote sensing observations [20,99,105]. Several vegetation indices (VIs) have been used to estimate $fAPAR_{green}$, most notably the normalized difference vegetation index (NDVI) [106]. When combined with PAR irradiance, either as a modeled or directly measured value (PAR sensor), fAPAR readily provides a reliable measure of APAR, the primary term in the LUE model (Equation 2.2).

The rising interest in linking carbon flux measurements, proximal (*in situ*) spectral measurements and remote sensing data has motivated the establishment of a global network of experimental sites in various ecosystems that simultaneously collect optical and flux datasets[69,101]. A key issue in combining optical and flux measurements is the evaluation of temporal scales, as optical and flux measurements vary on different time scales [69]. To our knowledge, few studies explicitly consider the effect on scale of aggregation when comparing optical and flux data, in part because satellite data are typically limited to a single overpass near midday. In this study, we took advantage of the continuous nature of flux and optical data to enable an explicit consideration of temporal aggregation, as recommended by the SpecNet community [101].

The objectives of this study were to:

- assess the seasonal patterns of CO_2 exchange, above-ground biomass accumulation, and optical properties of a prairie grassland ecosystem comparing different optical sampling techniques ($NDVI_{680,800}$ from field spectrometer measurements, proxy NDVI measurements from automated sensors on an "optical phenology station," and MODIS NDVI measurements);

- compare midday data aggregation periods for accurate prediction of fluxes from optical data;
- test different NDVI inputs and related biophysical parameters (fAPARgreen and APARgreen) from both satellite and ground measurements as proxies for flux measurements using the LUE model;
- test the hypothesis of constant ε over the entire season in grassland ecosystem;
- demonstrate how optical data can be used for gap-filling eddy covariance datasets.

2.2. Materials and Methods

2.2.1 Study site and experimental design

The Mattheis Ranch is a 4977 ha working cattle ranch located near Duchess in southern Alberta, Canada, and is mostly characterized by native prairie vegetation. Recently, this site has become a research area managed by the Rangeland Research Institute (University of Alberta), offering the possibility of long-term monitoring of ecosystem dynamics under management regimes typical of this region. The climate of southern Alberta presents long winters and short, windy summers with extreme temperatures in both seasons, and peak precipitation periods occurring in early summer (June). The rest of the summer usually has lower precipitation, but summer rainfall regimes can vary markedly from year to year, with a similarly variable effect on productivity[87].

Our study site centered around two eddy covariance tower locations designated "E5" (northern site, 50.9056N, 111.8823W) and "E3" (southern site, 50.8671N, 111.9045W), situated about 4.5 km apart. The two sites differed slightly in vegetation cover and microtopography; E5 appeared very flat and uniform, while the E3 landscape varied slightly more than E5 in microtopography and vegetation cover within the presumed flux tower footprint, but was still a relatively uniform grassland-dominated site. The E5 site represents typical dry mixed grass prairie as described by Adams et al. [84]. Based on a clay loam soil, the plant community is dominated by needle-and-thread grass (*Hesperostipa comata*), Junegrass (*Koeleria macrantha*), blue grama grass (*Bouteloua gracilis*), and western wheatgrass (*Pascopyrum smithii*). In contrast, the soil at the E3 site is a sandy loam. Dominant grasses include sand grass (*Calamovilfa longifolia*), needle-and-thread grass (*Hesperostipa comata*), and low sedge (*Carex stenophylla*). Slight variations in topography allow forbs such as wild licorice (*Glycyrrhiza lepidota*) and golden bean (*Thermopsis rhombifolia*), and shrubs such as wild rose (*Rosa woodsii*) to flourish [107]. Due to these differences in vegetation, soil type and associated hydrology (not shown), these two sites provided a natural experiment encompassing two contrasting landscapes typical of southern Albertan rangelands.

The measurements at the two grassland sites (E3 and E5), included:

-CO_2 flux measurements from eddy covariance,

-continuous, proxy NDVI [101,108] from a set of 2-band radiometers, PAR and PYR (pyranometers), comprising a "phenology station",

-aboveground biomass samples from a 1 ha area around each flux tower site periodically collected following the sampling scheme reported in Figure 2.1,

- $NDVI_{680, 800}$ measurements using a field spectrometer collected at regular intervals in the same area (1 ha) using a 10 m grid spacing (Figure 2.1),

- incident and reflected incoming PAR measurements at each calibration point (numbered circles, Figure 2.1)

- MODIS satellite NDVI data downloaded for the study areas.

Each phenology station was located approximately 10 meters to the southeast of its corresponding flux tower. These two sites were monitored for two consecutive growing seasons (May-September) during 2012 and 2013.

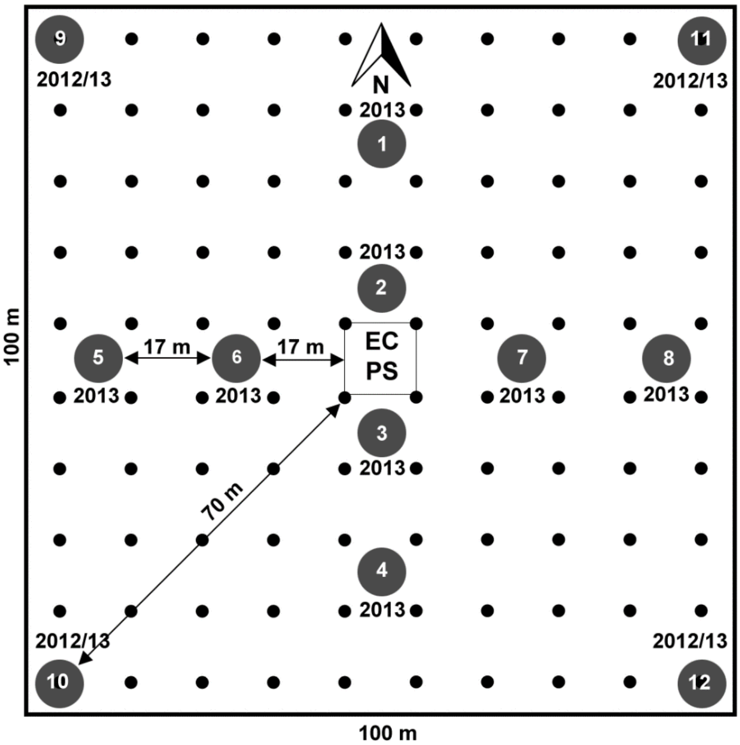

Figure 2.1. Optical and biomass sampling design around each eddy covariance (EC) and phenology station (PS) location. Leaf-level NDVI was sampled at regular intervals within a one hectare region surrounding each flux tower using 10m grid spacing (approx. 100 samples; sampling locations represented by black dots). Biomass sampling and fAPAR calibration occurred at the locations indicated by numbered circles (1-12), with the sampling years indicated by each circle.

2.2.2 NDVI measurements

2.2.2.1 NDVI$_{680,800}$ from spectrometer measurements

Narrow-band reflectance measurements were obtained with a dual channel spectrometer (UniSpec-DC, PP-Systems, Amesbury, Massachusetts, USA), which has a spectral range of 305-1130 nm and a ≈3 nm nominal bandwidth (10 nm full width at half maximum). The spectrometer was fitted with two optical fibers, one looking upward and one looking downward, enabling simultaneous sampling of downwelling irradiance and target radiance and correction for variable sky conditions. The upward-looking detector was fitted with a hemispherical cosine head (UNI435, PP Systems, Amesbury MA, USA) and sampled downwelling radiation (about 0.5 m^2 per sample); the downward-looking detector was fitted with a fiber optic (UNI684, PP Systems, Amesbury MA, USA) and field-of-view restrictor (hypotube, UNI688, PP Systems, Amesbury MA, USA) and sampled upwelling radiation with a nominal field-of-view of approx. 20 degrees from a distance of approx. 2 m.

The spectrometer sampling procedure involved sampling a 1-hectare grid centered on the flux tower (Figure 2.1). This grid sampling was completed approximately every 20 days during the growing season. Measurements were collected across a 100 X 100 m area (roughly 100 samples on a 10 m grid spacing) within one hour of solar noon. This allowed us to calculate the NDVI of a larger portion of the flux footprint and to compare the field spectral measurements with those derived from the MODIS satellite sensors. In addition to the grid sampling, the field spectrometer was also used to determine NDVI at exactly the same location of each aboveground biomass sampling site for the purpose of NDVI-biomass calibration (numbered circles, Figure 2.1).

Spectral processing software (Multispec, http://specnet.info) was used to calculate raw reflectance values, calculated as the ratio between upwelling surface radiance (R_{target}) and downwelling solar irradiance ($I_{downwelling}$):

$$\text{Raw reflectance} = R_{target} / I_{downwelling} \qquad (2.3)$$

This software also interpolated reflectance to 1-nm wavebands for index calculation.

The next step was to calculate a cross-calibration value comparing downwelling solar irradiance ($I_{downwelling}$) to a 99% reflective white standard panel (R_{panel}) (Spectralon, Labsphere Inc., North Sutton, NH):

$$\text{Cross-calibration} = I_{downwelling} / R_{panel} \qquad (2.4)$$

This cross-calibration was then used to calculate a corrected reflectance value as follows:

$$R_{corrected} = (R_{target}/I_{downwelling}) * (I_{downwelling}/R_{panel}) \qquad (2.5)$$

This application of the cross-calibration was corrected for optical differences among sensors and changing irradiance [109]. Both target and panel readings were taken under similar illumination and sun angle conditions. White panel measurements were taken at the beginning and ending of every grid sampling procedure.

Narrowband NDVI was calculated using spectrometer grid data using the 680 nm waveband for the red region of the spectra and the 800 nm waveband for the infrared region using the following formula:

$$NDVI_{680,800}=(\rho_{800}-\rho_{680})/(\rho_{800}+\rho_{680}) \qquad (2.6)$$

where ρ represents the reflectance at a given waveband, and subscripts indicate the wavelength values used. $NDVI_{680,800}$ was compared to green biomass and $fAPAR_{green}$ (see sections 2.2.4 and 2.2.5), but because of the low sampling frequency (about every 20 days) was not compared to daily flux values or used in the LUE model. For these purposes, reflectance spectra from the calibration sites were convolved against PAR, PYR, and MODIS NDVI band responses. These bands were then used to simulate proxy and MODIS NDVI values for calibration against $fAPAR_{green}$ (see section 2.2.5 below).

2.2.2.2 Proxy NDVI measurements

Each site was monitored with an optical phenology station consisting of a data logger (H21-001, Onset Computer Corporation, Bourne, Massachusetts, USA) and two-band radiometer mounted on a boom and tripod, 3 m above the ground, placed approximately 10 meters southwest of each tower. The sensors detected incoming light (irradiance) and reflected light from the canopy. One band consisted of two PAR (photosynthetic active radiation) sensors (S-LIA, Onset Computer Corporation, Bourne, Massachusetts, USA) that measure the photosynthetic photon flux density (PPFD) within the PAR band (400-700 nm), and the other band consisted of two PYR (pyranometer) sensors (S-LIB, Onset Computer Corporation, Bourne, Massachusetts, USA) measuring across a spectral range from 300 to 1100 nm. Both up- and down-looking sensors had cosine (nominally 180 degree) foreoptics, allowing us to sample a relatively large area ($\approx 100\ m^2$) immediately adjacent to the flux tower, but restricted to a small portion of the total flux footprint (typically > 1 ha, with variations depending on windspeed and wind direction). This phenology station provided a continuous, high temporal resolution proxy NDVI by means of continuous broad-band reflectance in both PAR and PYR bands sampled every 1-minute during the whole growing season and logged as 15-minute averages, thus monitoring seasonal changes in the vegetation photosynthetic phenology [108]. Additionally, temperature and relative humidity were monitored via appropriate sensors (RH; S-THB-M002, Onset Computer Corporation, Bourne MA, USA) allowing rainy-day optical data to be identified and filtered from the dataset (see Section 2.2.6, below). To derive proxy NDVI values, each sensor pair had been previously cross-calibrated against one another by comparing both upward- and downward-looking sensors in an upward-looking (irradiance) configuration, yielding a coefficient that corrected for any sensor differences (typically less than 5%). These coefficients were then applied to each sensor pair (PAR and PYR) prior to calculating proxy NDVI. Subsequent analyses used the 15-minute averages to calculate midday average APAR and proxy NDVI values for comparison with midday average net CO_2 flux from the eddy covariance tower (Figure 2.2).

The phenology station data were used to compute an NDVI proxy [101,108] following the formula:

$$\text{NDVI proxy} = (\rho_{PYR} - \rho_{PAR})/(\rho_{PYR} + \rho_{PAR}) \qquad (2.7)$$

where ρ_{PYR} is the reflectance of the solar radiation (PYR band), calculated as the ratio of the reflected solar radiation to the incoming solar radiation and ρ_{PAR} is the reflectance of the photosynthetically active radiation (PAR band) calculated as the ratio between the reflected PAR and the incoming PAR. This provided a continuous NDVI proxy, which was then averaged over a 5-hour midday period (Figures 2.2-2.3) for comparison with the daily flux measurements. Using the calibrations derived from the harvest sites (equations 2.9-2.11), the NDVI proxy time series was used to derive green fAPAR for the LUE model (Figure 2.2). PAR from the phenology station was then combined with this $fAPAR_{green}$ to calculate $APAR_{green}$ in the LUE model (Equation 2.2, Figure 2.2).

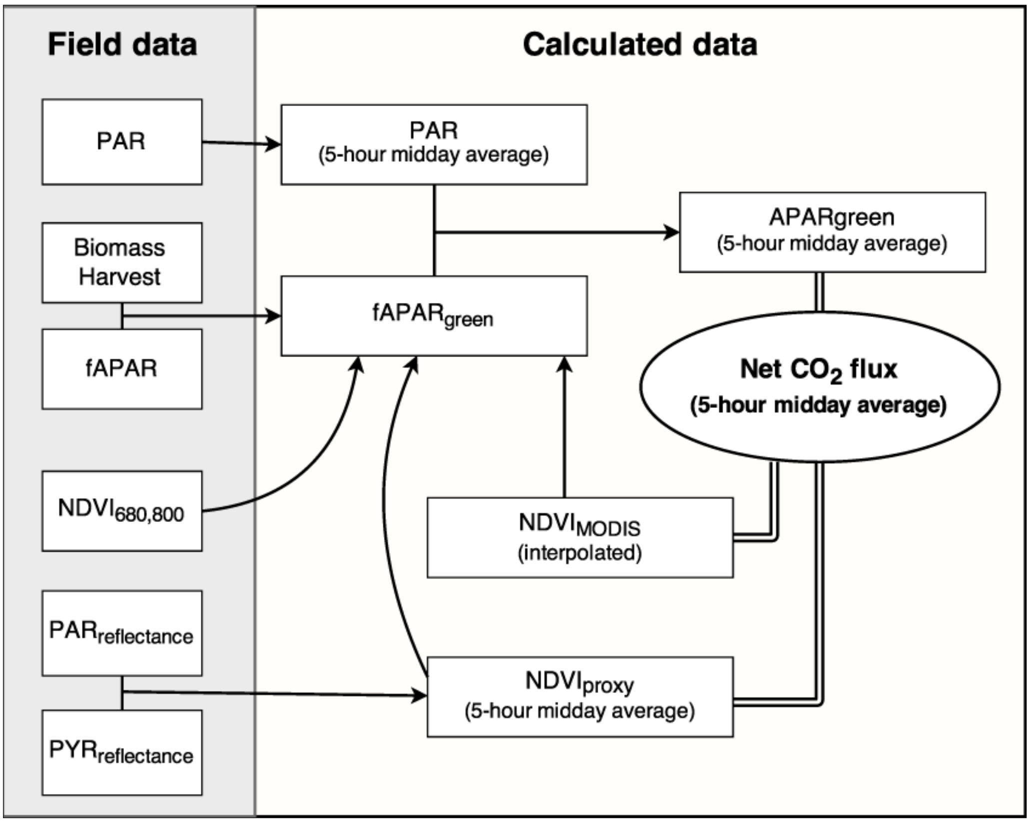

Figure 2.2. Experimental design, summarizing steps used in derivation of NDVI and APAR (arrows), and comparisons with net CO_2 fluxes (double lines).

2.2.2.3 MODIS NDVI measurements

The NASA Terra and Aqua satellites, which have orbited Earth since 1999 and 2002 respectively, each carry a MODIS (Moderate Resolution Imaging Spectroradiometer) sensor. These satellites pass daily over most of Earth’s surface and provide a nominal 250 m spatial resolution dataset in 36 spectral bands. NDVI values derived from MODIS NDVI products (MOD13Q1 from Terra and MYD13Q1 from Aqua) were downloaded from the Oak Ridge National Laboratory Distributed Active Archive Center website (http://daac.ornl.gov/cgi-bin/MODIS/GLBVIZ_1_Glb/modis_subset_order_global_col5.pl). MODIS bands 1 (red, 620 – 670 nm) and 2 (infrared, 841 – 876 nm) were used for MODIS NDVI calculation. The 16-day aggregation period was based on the best observations during the composite period, and the actual collection date for each optimal observation was used to provide more accurate time series. The date-corrected time series was then interpolated to produce a daily MODIS value for comparison with daily flux values (Figure 2.2).

2.2.3 CO_2 flux measurements

Net CO_2 fluxes were measured using the eddy covariance (EC) technique [96]. Identical EC flux towers were deployed at our E3 (50.8672º, -111.9045º) and E5 (50.9057º, -111.8823º) grassland sites. Sites exhibited uniform vegetation cover (described above), providing measureable fluxes from all wind directions (i.e., the flux footprint) except those passing through the tower structures. Each tower was equipped with an open-path infrared gas analyzer (IRGA; LI-7500, LI-COR, Lincoln NE, USA) and a three-dimensional sonic anemometer (CSAT3; Campbell Scientific, Logan UT, USA) to quantify vertical CO_2 fluxes. Each EC sensor was affixed at 2.9 m (E3 site) and 3.0 m (E5 site) above ground level and each IRGA was horizontally separated 15-17 cm from each sonic anemometer. Other sensors to quantify environmental conditions and weather were also fixed to each tower to measure half-hour averages of, for example, air temperature, relative humidity (RH) and soil conditions. All collected data were stored to a datalogger (CR5000, Campbell Scientific).

EC data were analyzed using the software package EddyPro (LI-COR, v. 5.1) to quality check raw data, remove outliers and apply standard corrections to calculate corrected vertical fluxes of CO_2. Raw 10Hz CO_2 fluxes were preconditioned by eliminating data spikes greater than 3.5 standard deviations (σ), temporary drop-outs (10% per bin), and heavily-skewed data ($+2>x<-2$). Calculated fluxes were corrected for density fluctuations using the Webb et al.[110] procedure. High-pass spectral corrections were implemented after Moncrieff et al. [111], while low-pass spectral corrections, integrating in-situ conditions to determine system cut-off frequencies, were used after Ibrom et al. [112]. Fluxes were further rejected when EC sensors malfunctioned or were affected by moisture, when wind passed through the tower before contacting EC sensors, or when friction velocities fell below 0.1 m s^{-1} (after Wille et al. [113]). Turbulence tests using the approach of Mauder and Foken [114] were used to remove the poorest-quality fluxes (level 2) when they did occur. Half-hour fluxes below -3σ or above $+3\sigma$ were considered outliers and removed. Corrections applied to daytime data resulted in the removal of 23.33% of all calculated fluxes across all EC measurements at both sites. For final comparison with optical data (NDVI and APARgreen), a midday average net CO_2 flux was calculated based on a 5-hour average, matching the period of averaging used for optical data (Figure 2.3).

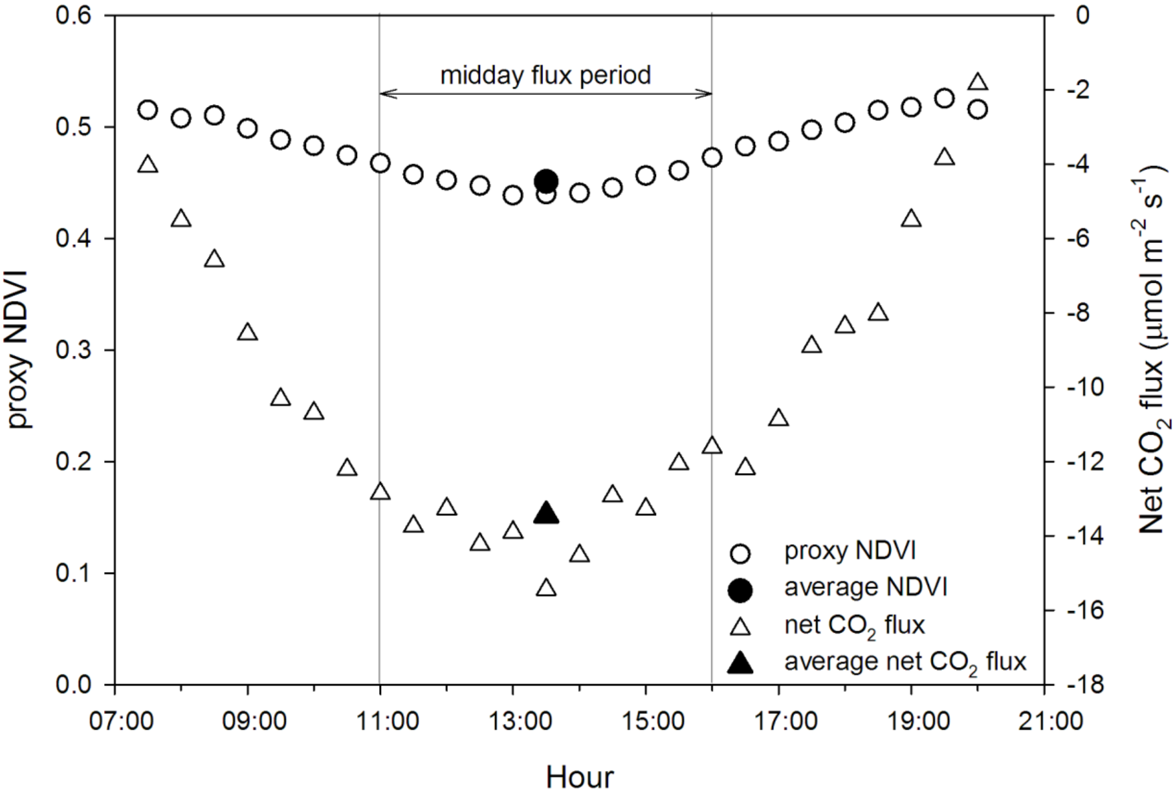

Figure 2.3. Sample diurnal course of proxy NDVI (from phenology station, circles) and net CO_2 flux (from eddy covariance, triangles), showing average values (open symbols) calculated for the 5-hour midday period (arrow between two vertical lines). Data from site E3, June 7, 2012**.**

2.2.4 Biomass estimation

From May to August 2012, vegetation samples were harvested from four biomass calibration points approximately every 20 days using a 30 cm diameter ring in both sites (E3 and E5) at a distance of 70 m from the tower in four directions (South-East, North-East, North–West, South-West) (Figure 2.1). The grass material within the ring was cut at ground level and placed into labeled paper bags. The following year, samples from 12 points (4 points above, plus 2 points 17 and 34 m from the tower, in each of four cardinal directions (North, East, South and West) were collected from May to July about every 20 days (Figure 2.1). Biomass samples were collected at each of the harvest sampling points just after the collection of both fAPAR measurements and reflectance measurements, used to calculated narrow-band NDVI ($NDVI_{680,800}$). Each sample was manually sorted into green biomass and brown biomass, put into an oven at 60 °C for 24 hours, and weighed. The selection was carried out considering the living tissue that was visibly green as green biomass and the visibly dead tissue as brown biomass. This selection of green and dead biomass allowed us to measure the current year’s production, since the green tissue represented the current year’s growth, and the dead tissue consisted of the previous year's growth. For each date, average green and total (green plus brown) above-ground biomass was calculated from the manually sorted and weighed biomass samples. For each sampling date, green biomass was calculated as the average of green biomass at all sampling locations (Figure 2), expressed as g m^{-2}. By providing a direct metric of productivity, this measure of biomass provided an independent check on the validity of the optical (NDVI) measurements and the resulting LUE model.

2.2.5 fAPAR and APAR calibration

At each calibration point (section 2.2.4 above; numbered circles, Figure 2.1), we also measured incident and reflected incoming PAR using a light bar (AccuPAR LP-80, Decagon, Pullman, Washington, USA). Particularly, along on NDVI from spectrometer measurements (Figure 2.1), we measured downwelling PAR above the canopy (S), upwelling PAR reflected from the canopy (R), downwelling PAR below the canopy (T), and upwelling PAR below the canopy (U). Ten measurements were made at each calibration point and averaged, then fAPAR was calculated, following the procedure described in Accupar user's manual (http://www.decagon.com/manuals/LPman12.pdf) and the equation:

$$f_{APAR} = 1 - t - r + tr_s \qquad (2.8)$$

Where t is the fraction of radiation transmitted through the canopy (t = T/S), r is the fraction of radiation reflected by the canopy (r = R/S), and r_s is the reflectance of the soil surface (r_s = U/T).

These fAPAR measurements were multiplied by the green:total biomass fraction (see section 2.2.4) to calculate a $fAPAR_{green}$ value (fraction of PAR absorbed by green canopy material) for comparison with the proxy NDVI values (phenology stations) and NDVI values collected at each harvest site (Figure 2.1). The NDVI- $fAPAR_{green}$ relationship was later used to derive the $APAR_{green}$ term of the LUE model (Equation 2.2), using the following equations derived from the fAPAR calibration sites:

$$fAPAR_{green} = (0.8799 * NDVI_{680,800}) - 0.1394 \ (R^2=0.79) \qquad (2.9)$$

$$fAPAR_{green} = (1.3916 * NDVI_{proxy}) - 0.3603 \ (R^2=0.82) \qquad (2.10)$$

$$fAPAR_{green} = (0.9879 * NDVI_{MODIS}) - 0.2131 \ (R^2=0.79) \qquad (2.11)$$

In accordance with equation 2.2, continuous $APAR_{green}$, was calculated as the product of PAR (i.e. PPFD) and $fAPAR_{green}$ values.

2.2.6 Filtering and averaging process

Preliminary analysis of the optical data indicated that periods of rainfall led to invalid proxy NDVI values. These periods were easily detectible by evaluating proxy NDVI data relative humidity (RH) values. Proxy NDVI values associated with RH values greater than 76% were filtered from the dataset were discarded to remove invalid data as this threshold best withdraw outliers (data not shown). Similarly, automatic gain control (AGC), an IRGA diagnostic value, identified obstructions blocking the sensor's optical path. Water droplets, rime, dew, dust or pollen on the optical path impede sensor function and reduce data quality. Proxy NDVI data with associated AGC values greater than 64% were filtered from the dataset. To achieve data comparable to the MODIS values, a midday averaging process was also applied to aggregate proxy NDVI and flux data. To determine how best to integrate flux and optical data, 3 different temporal aggregation periods were considered in our analysis by averaging measurements taken in the time window of 1-hour (13 pm-14 pm), 3-hour (12 am-15 pm) and 5-hour (11 am-16 pm) around midday (approx. 13:30 local daylight savings time). Based on this analysis, a 5 hour averaged value around midday for both CO_2 flux and proxy NDVI was used for our further analyses (Figure 2.2 and Figure 2.3).

2.2.7 Gap filling

A primary study aim was to test the utility of optical data as a proxy of EC flux measurements, thus allowing gap-filling of the flux dataset. Non-gap-filled flux data were augmented by both filtered proxy NDVI data (which provided the most continuous time-series of all three NDVIs used in this study, but not necessarily the most spatially representative NDVI) and MODIS data (less continuous, but more spatially representative). The relationships between NDVI and fluxes were then used to estimate missing flux data by applying several parameterizations of the LUE model (Equation 2.1), each assuming an invariant efficiency (ε) but variable optical inputs representing APAR. According to LUE model, we used and compared different model terms: parameterizations ranged from simple NDVI (proxy NDVI and MODIS NDVI) to APAR, calculated by combining proxy fAPAR (derived from NDVI) with PAR irradiance (PPFD).

When comparing proxy NDVI to CO_2 fluxes, both datasets were averaged for a 5-hour interval around solar noon (11 am - 4 pm; Figure 2.3) and these values were used as the daily value for flux and proxy NDVI, respectively. These midday average values were then used to model and fill data gaps in the flux data from optical measurements.

When using MODIS NDVI values, NDVI for each day over the entire season was calculated through a linear interpolation of actual date values from MODIS NDVI products (MOD13Q1 from

Terra and MYD13Q1 from Aqua). The relationships between MODIS NDVI and net CO_2 fluxes were then used to estimate flux data throughout 2012 for comparison with the proxy NDVI method.

The calibration between green fAPAR and NDVI (Equations 2.9-2.11) were used to estimate continuous green fAPAR from the continuous proxy NDVI data. This was then combined with PAR irradiance (PPFD) from the phenology stations to calculate a continuous APAR using equation 2.2, with PAR averaged over a 5-hour midday period. The resulting midday average APAR was then calibrated against midday average net CO_2 flux (Figure 2.2). The relationships between APAR and net CO_2 flux were used to estimate midday flux data for 2012, and to gap-fill missing flux data. Finally, measured fluxes were compared with the gap-filled, modeled fluxes based on proxy and MODIS NDVI (Figure 2.2).

2.3. Results

At both sites, NDVI values obtained from the three different methods all showed similar patterns over the summer growing season, reaching peaks within the first half of July, while green biomass showed maximum values later in the month (Figure 2.4). An exception was a single MODIS Terra NDVI value in each year (8 July 2012 and 11 July 2013) that yielded one anomalously high NDVI value for each site and date (Table 2.1, and Figure 2.4). In most cases (particularly in 2012), the E3 site showed slightly higher productivity than the E5 site, demonstrated by the generally higher NDVI values for E3 (Table 2.1). In most cases, higher values of NDVIs occurred in 2013 as compared with 2012 (Figure 2.4, Table 2.1). A particularly low peak proxy NDVI value in E5 during 2012 (asterisk, Table 2.1) was the result of a mid-season data gap (spanning from June 26 to August 27, 2012). In general, MODIS Terra values were higher than the corresponding Aqua values, and MODIS values were higher than the ground-based NDVI values, in agreement with previous studies (e.g. [115]).

Table 2.1. Peak NDVI values and standard deviation (σ) in 2012 and 2013 for both sites (E3 and E5), obtained with $NDVI_{680,600}$ (grid sampling method), proxy NDVI (phenology station), and MODIS satellite (AQUA and TERRA sensors). The asterisk (*) indicates an anomalously low peak value due to missing mid-season data (spanning June 26-August 27, 2012).

Peak NDVI values	2012				2013			
	E3	σ	E5	σ	E3	σ	E5	σ
NDVI680,800	0.54	0.09	0.51	0.06	0.60	0.09	0.59	0.06
Proxy NDVI	0.56	0.01	0.47*	0.03	0.58	0.02	0.59	0.02
MODIS NDVI-Terra	0.69	-	0.60	-	0.68	-	0.66	-
MODIS NDVI-Aqua	0.61	-	0.53	-	0.58	-	0.59	-

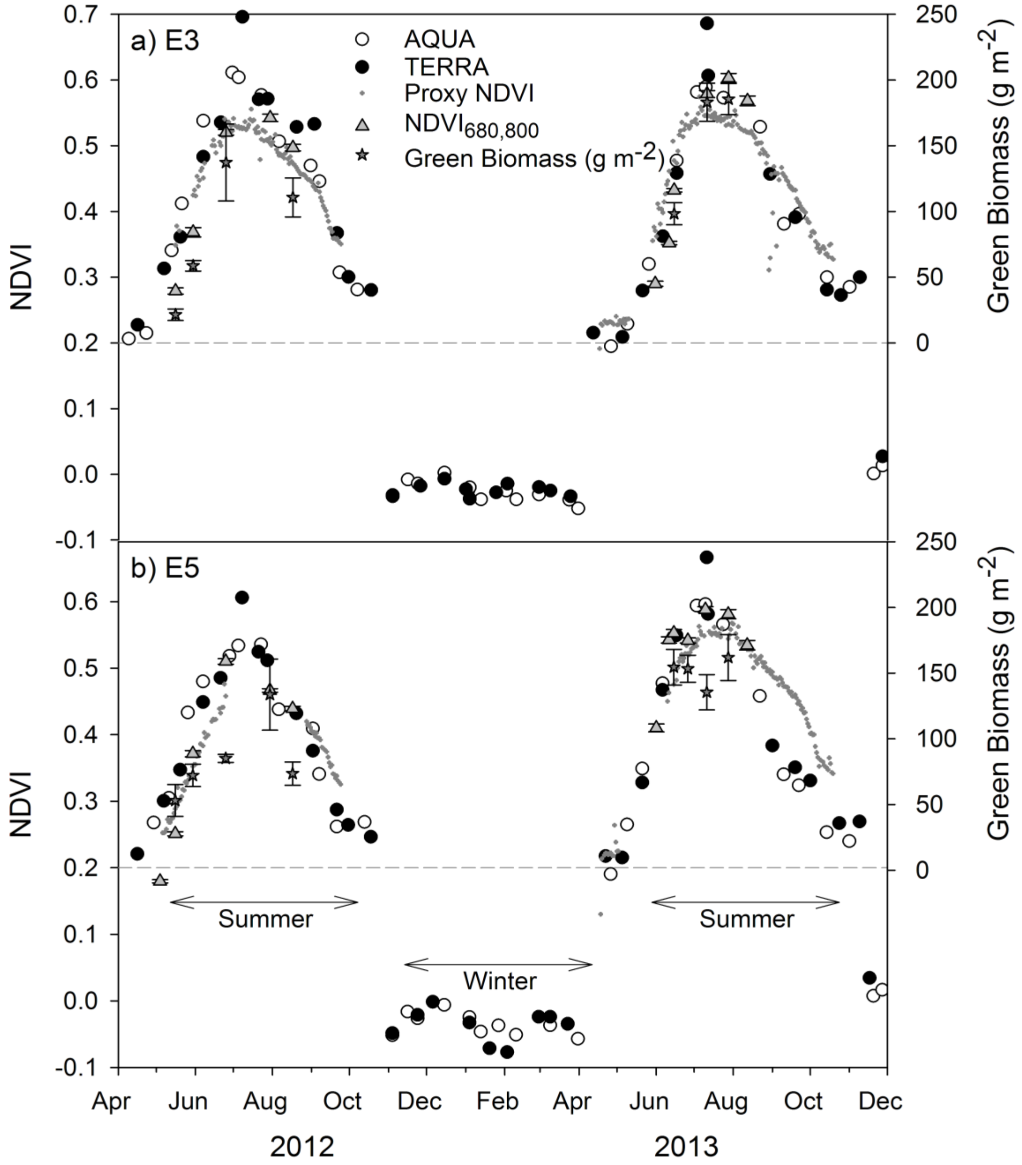

Figure 2.4. Biannual time series (2012-2013) of $NDVI_{680,800}$ collected from spectrometer with grid method, proxy NDVI from 2-channel sensors on phenology station (5 hour averaged), MODIS NDVI (Aqua and Terra satellites), green biomass, at a) E3 site, b)E5 site. Low (<0) NDVI values due to winter snow cover.

In preliminary analyses, temporal averaging of proxy NDVI (Figure 2.3) reduced short-term variability and clarified seasonal patterns. The impact of temporal aggregation was quantified by calculating the R^2 for the increasing time intervals considered (1, 3, 5 hour midday periods). R^2 values increased from 1-hour to 5-hour averaging periods considering the whole season; similar results were found when considering green up and senescence periods separately (Table 2.2). Consequently, since the relationship between proxy NDVI and net CO_2 flux showed the best fit using the 5-hour aggregation period (Table 2.2), this time period was used in all subsequent analyses of proxy NDVI as optimal aggregation period.

Table 2.2. R^2 and equations for fits between net CO_2 flux and different midday averaging period of proxy NDVI calculated both for the full season and for the first and second halves (green-up and senescence). The average intervals considered were 5-hour, 3-hour and 1-hour around midday (approximately 13:30 local daylight savings time). In all cases, proxy NDVI was filtered with the method explained in the text.

R^2 and equation	Full season	Separate seasons	
		Green up	Senescence
Proxy NDVI (1-hour)	0.45 y = -46.167x + 13.139	0.40 y = -38.306x + 6.7617	0.56 y = -48.023x + 14.737
Proxy NDVI (3-hour)	0.50 y = -44.159x + 12.52	0.49 y = -41.083x + 8.547	0.61 y = -44.975x + 13.597
Proxy NDVI (5-hour)	0.61 y = -45.18x + 13.298	0.71 y = -45.55x + 11.175	0.69 y = -46.039x + 14.266

Strong correlations emerged between each of the NDVI variants and green biomass (Figure 2.5). No significant differences occur between the slopes and the intercepts of the relationships for E3 and E5, thus allowing us to fit a single regression to the NDVI- green biomass data from both sites. Of the three NDVIs, the narrow-band NDVI yielded a slightly stronger correlation ($R^2 = 0.82$) than the proxy ($R^2 = 0.73$) or MODIS ($R^2 = 0.73$) NDVIs (Figure 2.5). All the relationships were statistically significant, showing P values < 0.01.

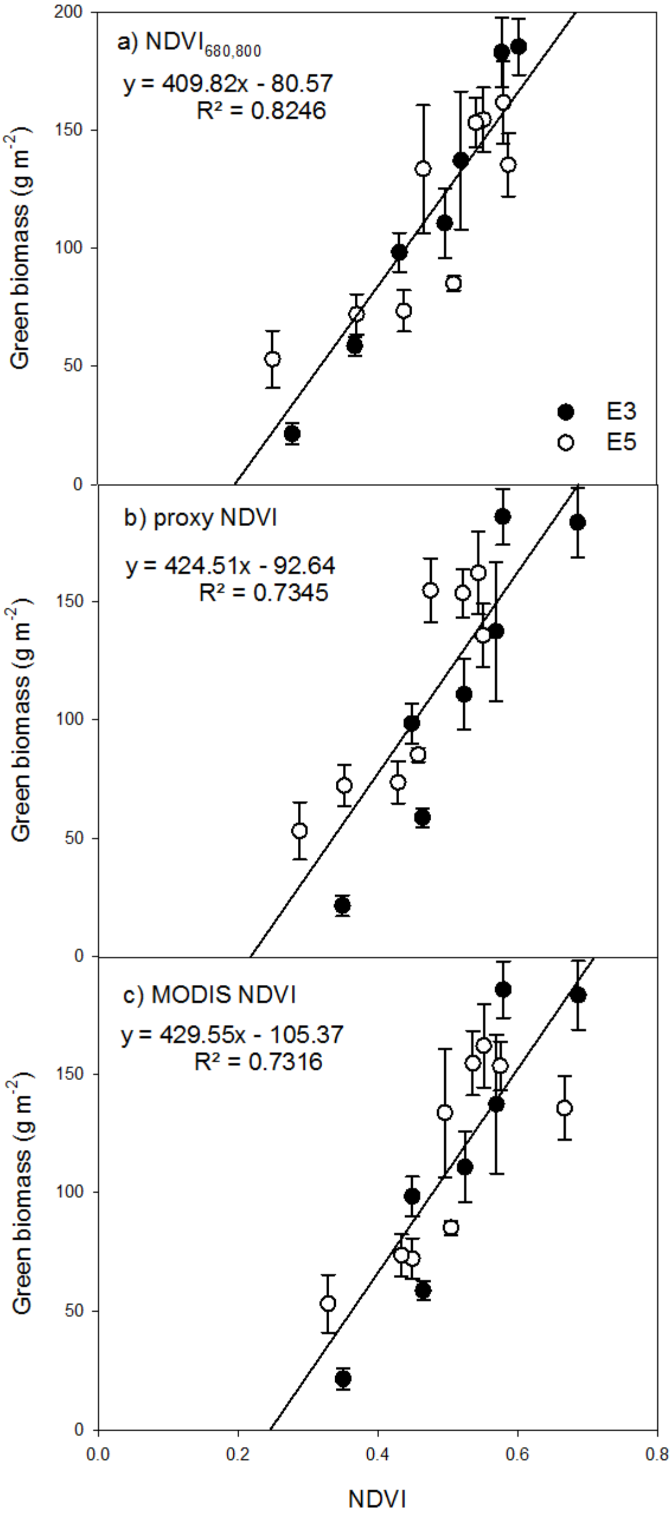

Figure 2.5. Correlations between green biomass and (a) $NDVI_{680,800}$, (b) proxy NDVI (5 hour averaged) and (c) MODIS NDVI for both E3 (black dots) and E5 sites (white dots). Error bars for green biomass are expressed as standard error of the mean. Resulting equations and correlations (R^2 values) are indicated for each fit above.

Figure 2.6 and Figure 2.7 present the different stages in flux-optical comparison, LUE model testing, and subsequent gap-filling of the flux dataset using optical datasets, including results based on proxy NDVI (panel a), MODIS NDVI (panel b), or APAR (panel c). For this purpose, only results from the E3 site during 2012 were selected because this year had the fewest gaps in the optical measurements. To explore the possible effect of hysteresis in our datasets, relationships between flux and NDVI (or APAR) are presented for the whole season (single fit) and for the green up phase and the maturity phase separately (separate fits). In this analysis, the peak flux value of the season was used to separate the season in the two parts. Better model estimates (higher R^2 values) were obtained when separate equations were used for the two parts of the season (Figure 2.6, Table 2.3). Flux model estimates derived from MODIS NDVI or APAR (based on proxy NDVI) yielded slightly better agreement with measured fluxes than the estimates based on proxy NDVI (Table 2.3).

Table 2.3. R^2 values for fits between net CO_2 flux and various expressions of optical data (proxy NDVI, MODIS NDVI, and green APAR values, calculated both for the full season and for the first and second halves (green-up and senescence). In all cases, NDVI, Green APAR, and CO_2 flux values were based on 5-hour averages around midday.

R^2	Full season	Separate seasons	
		Green up	Senescence
Proxy NDVI	0.61	0.71	0.69
MODIS NDVI	0.79	0.71	0.85
Green APAR (green fAPAR x PAR)	0.69	0.79	0.77

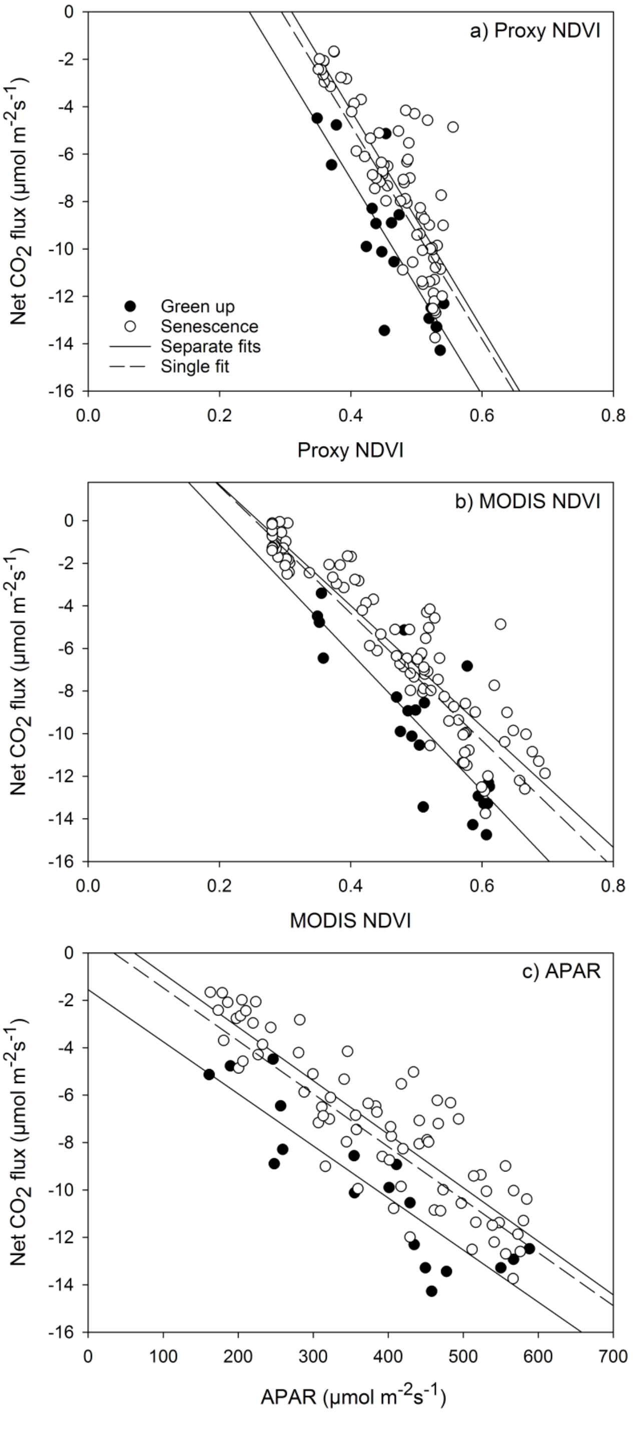

Figure 2.6. Relationship between proxy NDVI (5 hour average, panel a), MODIS NDVI (panel b), APAR (panel c) and filtered net CO_2 fluxes (5 hour average) for the E3 site in 2012. Fits are shown for the whole season (dashed line), for the green-up phase (black dots, solid line), and for the senescence phase (white dots, solid line). Panel a correlation coefficients (R^2 values) are 0.61 (whole season), 0.71 (green-up phase) and 0.69 (senescence phase). Panel b correlation coefficients are 0.79 (whole season), 0.71 (green-up phase) and 0.85 (senescence phase). P values are < 0.001 for all the relationships. Panel c correlation coefficients are 0.69 (whole season), 0.79 (green-up phase) and 0.77 (senescence phase). P values are < 0.001 for all the relationships.

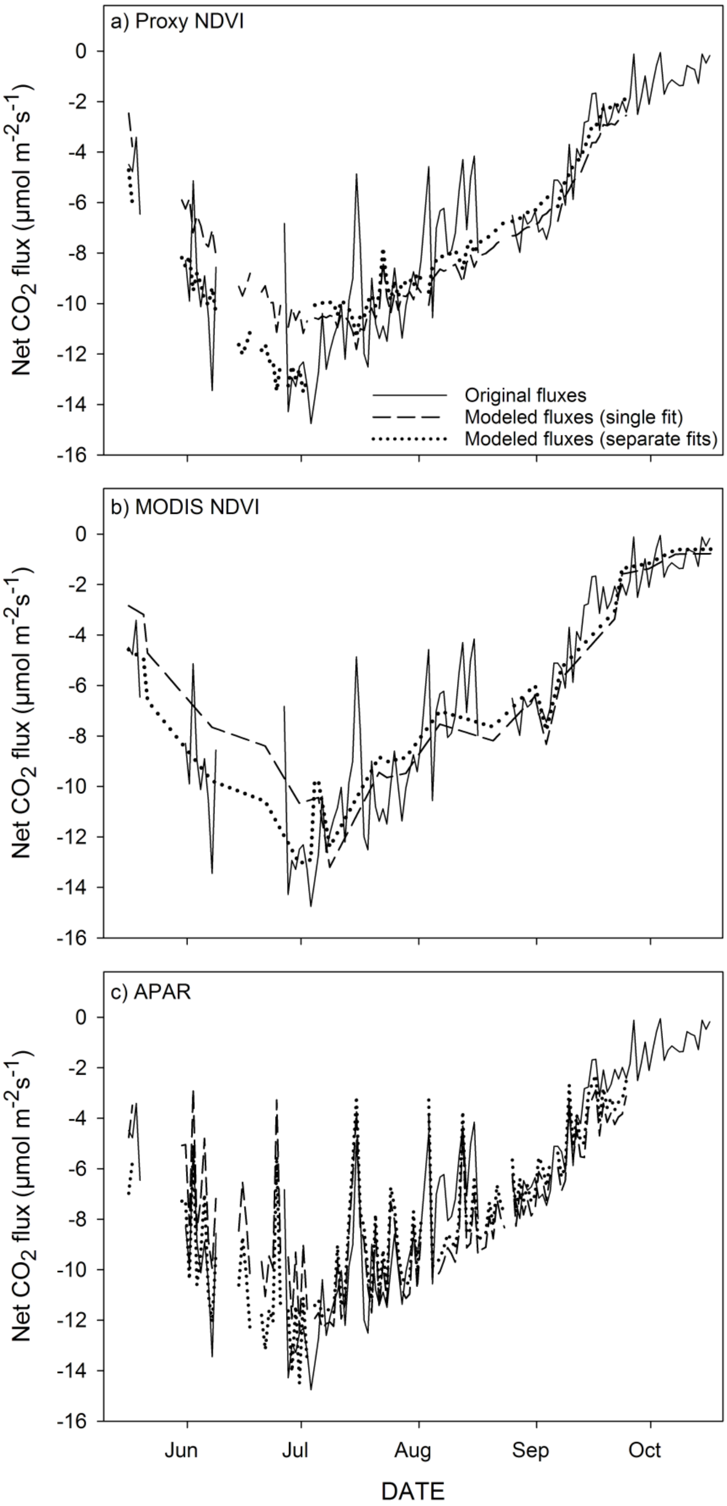

Figure 2.7. Time series of observed and modeled net CO_2 fluxes based on proxy NDVI (panel a), MODIS NDVI (panel b), and APAR (panel C). The original fluxes are shown as solid lines. Fluxes modeled using a single fit are shown as dashed lines, and fluxes modeled using two separate fits are shown as dotted lines. All results are for the E3 site in 2012.

The resulting time trends of modeled and measured fluxes using these two approaches (whole-season vs. two halves) are shown in Figure 2.7. Regardless of the model formulation, a single fit for the whole season tended to underestimate fluxes in the first half of the season and overestimate them in the second, and separate fits improved the agreement (Figure 2.7). In our final exercise, we used green APAR as independent variable and net CO_2 flux as a dependent variable to derive a modeled flux (Figure 2.6c and Figure 2.7c). Unlike NDVI, APAR also explicitly considers the dynamic variation in PAR irradiance (i.e., PPFD), and thus incorporated hourly and day-to-day variation in illumination. Relative to the proxy NDVI (from which it was derived), the APAR-based model yielded a better fit with measured fluxes. The APAR based model also yielded more dynamic patterns of flux measurements relative to NDVI-based models (cf. Figure 2.7c to Figure 2.7a&b)

2.4. Discussion

Eddy covariance measurements, while they provide the "gold standard" for net CO_2 flux measurements, are often affected by a number of problems, including instrumentation malfunctioning or low friction velocity, which can cause long data gaps. For this reason, several methods have been implemented to overcome periods of missing data [116–118]. The novelty of our approach lies in the particular combination of sensors used. In this study, we demonstrate the possibility of modeling and filling the gaps in a carbon flux dataset using empirical methods based on irradiance and spectral reflectance measurements. We address the data aggregation in the time domain and take advantage of flux station meteorological variables to filter optical measurements, thus integrating different dataset.

Over the years, NDVI has emerged as a widely used reflectance index for detecting seasonal changes related to photosynthetic activity [45,119–122]. The effectiveness of NDVI as a proxy of green biomass, and as a useful parameter in a simple expression of the LUE model for a grassland ecosystem is confirmed in our study. The strong correlations between NDVI, APAR, and midday CO_2 flux for this prairie grassland provide a strong foundation for using optical measurements to model fluxes and gap-fill eddy covariance data, as proposed by Wohlfahrt et al. [118]. Our findings are in agreement with past studies that have shown good correlations between NDVI and green biomass, green APAR, or total canopy chlorophyll content for many ecosystems [120,123–125]. Strong agreements between NDVI or NDVI-based modeled fluxes and eddy covariance measurements, particularly for ecosystems dominated by annual grasslands, are reported by similar studies [120,124,126]. These observations illustrate the utility of combining optical and flux measurements to characterize seasonal photosynthetic patterns.

The best relationship with NDVI and green biomass was established with $NDVI_{680,800}$, but similar, strong patterns were found for all NDVI formulations (Figure 2.5). More work would be needed to understand the slight differences, which are presumably related to the different band formulations, temporal sampling periods, or footprints of the three NDVI methods. Despite its broad-band formulation, proxy NDVI was able to depict most of the seasonal variability in net CO_2 flux, in part due to its continuous sampling (similar to eddy covariance sampling). This outcome highlights the utility of broadband proxy NDVI for monitoring seasonal photosynthetic activity ("photosynthetic phenology") using a set of simple, inexpensive optical measurements [108]. These findings demonstrate that, for the purpose of measuring the seasonal course of photosynthetic activity in grassland ecosystems, dual channel low-cost sensors can replace more complex and expensive hyperspectral sensors at eddy covariance sites when the budget is limited [101,108,127,128]. Of the three NDVI methods used, the proxy NDVI had the most limited sampling footprint, which might explain why it sometimes deviated from the other methods in the depiction of seasonal trends (Figure 2.4), and why it yielded slightly lower agreement with measured fluxes relative to MODIS NDVI (Figure 2.6).

Several versions of the LUE model driven by satellite remote sensing of NDVI have been in wide use for many years [72,99,129,130]. While these models can depict broad global patterns, their agreement with local field measurements varies considerably across ecosystems or with different model formulation [131,132]. In fact, the selection of input parameters (e.g., PAR, fAPAR, APAR, ε) can broadly affect the results [1]. Site-specific studies incorporating proximal optical measurements can offer insights into these causes of variation. Several recent studies have focused on estimation of carbon dioxide fluxes using proximal optical measurements as proxies for CO_2 fluxes [118,124,127]. However, a universal LUE model parameterization to estimate fluxes from proximal optical measurements for all ecosystems, while often discussed, does not yet exist [63,71]**.** Despite these limitations, it is clear that simple models that use linear relationships between fluxes and greenness spectral measurements such as those used in our study can successfully be used to estimate seasonal patterns of CO_2 flux for certain ecosystems[21].

In our study, we compared the estimates of carbon fluxes using different predictor variables (proxy NDVI, MODIS NDVI and green APAR), which reproduced the seasonal net CO_2 flux patterns with varying degrees of fidelity. This experiment allowed us to show that the APAR-based method improved the estimates over NDVI alone. The proxy and MODIS NDVI methods could not explain all the flux variability since they could not capture high-frequency flux changes due to irradiance dynamics. Unlike NDVI, APAR is not only influenced by canopy structure, but also incorporates PAR irradiance (PPFD) [63]. Consequently, the incorporation of PAR irradiance (PPFD) in the relationship better captures the light dynamics affecting fluxes. This is probably one of the main reasons why the APAR-based model depicted the day-to-day variation in net CO_2 fluxes much better than NDVI alone (Figure 2.7). While similar findings have been reported in some cases [133], other studies [128] have sometimes reported the opposite, finding that incorporation of PAR to yield APAR degrades agreement with CO_2 fluxes relative to NDVI or fAPAR alone. The reasons for these discrepancies deserve further consideration, and could partly result from the degree of stress (and variation in light-use efficiency), which can be assessed by the shape of the APAR-flux curve. Additionally, the period of data aggregation could also affect these relationships, as the effects of including PAR are often more readily visible at fine scales (Figure 2.7). In general, while validation of modeled productivity using in situ measurements provides essential information on model performance, sampling strategies and methodological differences in data collection complicate comparability [134].

This simple regression approach used in our study appears to work particularly well in ecosystems characterized by strong seasonal dynamics in above-ground green biomass such as grasslands and croplands [120,123,124,126,127]. In our grassland ecosystem, where seasonal CO_2 fluxes largely scaled with canopy development (e.g. as measured by green, above-ground biomass, Figure 2.4 and Figure 2.5), an APAR-based model assuming constant efficiency yielded good agreement with fluxes (Figure 2.6 and Figure 2.7), despite our ignoring the efficiency (ε) term in the LUE model. While the lack of standard definition of ε was recently addressed by Gitelson and Gamon [63], there is not a general assumption for ε term commonly accepted. In past studies, ε has been assumed constant for all vegetation [45], fixed for each vegetation type (varying among different plant communities) [1,135] or variable depending both on vegetation type and stress linked to environmental factors [99]. As it has been discussed elsewhere [136], we would not normally expect very large variations in efficiency (ε) over the season in grassland ecosystems. For this largely deciduous ecosystem, CO_2 fluxes can be reasonably approximated by green fAPAR (estimated by NDVI alone) or by green APAR, allowing us to assume a constant efficiency (ε) over much of the growing season. This supports the hypothesis that, in these annual ecosystems, controls on ecosystem fluxes are largely related to canopy structure, with relatively little physiological control evident [71]. These findings are in agreement with a broad range of studies that note strong relationships between CO_2 fluxes and green canopy structure, expressed as green APAR, LAI, or total canopy chlorophyll [120,123,126,137]. In such cases, modeling efforts should focus primarily on accurate estimation of the APAR term in the LUE model.

Not all ecosystems lend themselves to such simple analyses. In many cases, a simple APAR-based model based may be insufficient, particularly for evergreen ecosystems where dynamic light-use efficiency can be an important determinant of CO_2 fluxes and may have to be included in the model [71,136,138]. Additionally, the exact definition and parameterization of the LUE model may itself affect observations regarding light-use efficiency. Many studies define LUE as the flux rate divided by PAR irradiance (incident PPFD) [133,139], causing the efficiency term to be confounded with green canopy structure. In deciduous canopies, this definition of the model terms can lead to large seasonal variations in *apparent* efficiency that may actually be caused by variations in green canopy structure (the green APAR term of our model), not efficiency as defined in our analysis. As introduced, we defined APAR based on radiation *absorbed* by green canopies (green APAR), not incident radiation. This distinction and its consequences has been discussed in more detail elsewhere [63]. These differences in model definition and formulation make it difficult to directly compare results across sites and ecosystems, hindering meta-analyses, and confounding larger conclusions beyond the seemingly disparate results of different studies. Consequently, further attention to model formulation with the goal of standardized definition and parameterization of model terms is recommended.

Despite the generally good fit between a simple APAR-based model and measured CO_2 fluxes, some unexplained features remain. In our study, we found that the fit between CO_2 fluxes and both NDVI and APAR presented some hysteresis between the first and second halves of the growing season. Using different equations for these two growth phases considerably improved the flux estimates over the use of a single equation. This observation agrees with several similar findings of seasonal hysteresis between optical and flux measurements in other annual-dominated ecosystems [125,140]. Such hysteresis could have several causes. It is likely that ecosystem carbon balance between photosynthesis and respiration shifts over the course of the season, contributing to the hysteresis in APAR and measured fluxes, and this could also cause a seasonal shift in the APAR-flux patterns that could be interpreted as a change in light-use efficiency. In grasslands, the dead biomass that partially hides new green biomass in the early stage, which is the carry over effect of the previous season’s growth, along with the gradually declining chlorophyll and nitrogen content of the leaves during the senescence phase, can also affect the optical-flux relationship. It is possible that partitioning vegetation into “green” and “brown” failed to capture the subtle dynamics of leaf pigmentation over the season, leading to an apparent change in LUE. Variation in canopy structure (e.g. leaf rolling or leaf inclination angle over the season) could also contribute to this hysteresis. These possibilities warrant further investigation and should be considered in future efforts to model fluxes from optical sensors, particularly if we are to apply the LUE model to all phases of the season. In a similar study, Flanagan et al. [140], documented that ε could decline in the senescence phase due to low soil moisture and high vapour pressure difference (VPD). Such stress in the late season can explain why a unique equation might not be accurate for modeling seasonal CO_2 fluxes. This finding revealed that, when assuming an approach of a linear relationship with a greenness index such NDVI, environmental stress that are not related to chlorophyll content or changing in structure, cannot be detected [128]. We can conclude that, the hypothesis of a constant ε for our ecosystem seems violated over entire season (May- October), but holds for half season periods.

Obtaining an adequate optical sampling within the eddy covariance footprint can be a challenging issue [71,109,141]. Due to the high variability of the eddy covariance footprint, which varies with wind speed and direction [67], it is not always feasible to directly couple optical and flux footprints, so approximations are often necessary. Preliminary results of the flux footprint analysis for our site suggest a typical flux footprint area slightly larger than 1 ha [142]. In our study, the 1 ha grid $NDVI_{680,800}$ measurements were intended to approximate the footprint of the eddy covariance tower in size, but not necessarily in shape due to the temporal dynamics of the flux footprint. Because $NDVI_{680, 800}$ involved intensive manual sampling, it was limited to periodic measurement and could not provide a sufficiently dense time series to allow close comparison with the continuous flux measurements. Similarly, the spatial coverage of the MODIS NDVI (pixel size nominally 250 m x 250 m) provided a reasonable sample of the eddy covariance footprint but ignored its temporal dynamics. MODIS NDVI provided a sufficiently frequent time series that (once interpolated to daily data) allowed comparison with seasonal flux measurements. Of the three NDVI methods, the proxy NDVI from the automated phenology station provided the most detailed time series, matching the sampling frequency to that of the flux measurements. However, the proxy NDVI footprint was limited to a relatively small area (estimated at a few tens of meters squared), which may have reduced its effectiveness in modeling the CO_2 uptake form the much larger and more dynamic flux footprint. These differences in “optical footprint” among NDVI methods undoubtedly influenced our results, presumably contributing to the slight contrasts in seasonal patterns (Figure 2.4) and the different strengths of correlation between NDVIs and biomass (Figure 2.5) or net CO_2 flux (e.g. Figure 2.6 and Figure 2.7).

Temporal data aggregation is another important consideration, analogous to the challenge of footprint characterization and matching. Averaging flux and proxy NDVI measurements reduced fine-scale variability of both datasets suggesting that proper temporal aggregation can improve model accuracy when comparing optical and flux data (Table 2.2). Our findings show that it is crucial to optimize the temporal aggregation when fluxes are related to optical measurements since aggregation can deeply influence the accuracy of the resulting model (Table 2.2). For our study, a 5-hour averaging period (Table 2.2) worked best, but we would expect the optimal aggregation period to vary slightly with conditions, e.g. depending upon the stability of the fluxes and optical sampling, which would vary with latitude and daylength across sites. Thus, the topic of optimal aggregation period deserves further study and should be considered as an important issue when predicting fluxes from optical data.

Clearly, one of the challenges of integrating remote and proximal sensing with LUE model in the context of the flux footprint is the need for defining an appropriate temporal and spatial sampling scale. More efforts are needed in the future to further clarify this issue. A possible improvement might derive from integrating a high number of wireless sensors in order to expand the footprint of optical sampling while maintaining high frequency to better match the footprint and time scale of eddy covariance tower. At our site, we are examining this method of improving the spatial representation of proxy NDVI sampling while preserving the rich time series of automated measurements. In the future, UAVs offer to improve the footprint of field optical sampling, but obtaining sufficiently rich time series data will remain a challenge.

The integration of optical and flux measurements can add insights and capabilities beyond those of either measurement alone, in part by addressing the common problem of missing data. Ongoing integration of optical and flux measurements in the framework of the LUE model offers rich potential for improved evaluation of carbon uptake and sequestration for rangeland sites. Comparisons of optical and flux measurements can provide a basis for extrapolating fluxes beyond the scale of the flux tower footprint to larger areas (“upscaling”). Further attention is needed to standardizing these methods across sites and research groups in order to reach the full potential of integrating optical with flux measurements to deepen our understanding of ecosystem carbon fluxes.

2.5. Conclusions

The main take-home messages of this study exploring the potential of blending different datasets together for monitoring grassland ecosystem are:

- optical inputs to a simple empirical LUE model closely track seasonal carbon fluxes and provide a simple proxy to fill gaps in the eddy covariance datasets;
- the three NDVI methods could give slightly different results depending on different band formulations, footprints and temporal sampling periods; however low cost sensor (proxy NDVI) can be adopted for monitoring CO_2 fluxes;
- temporal aggregation improve model accuracy and further analysis are needed for evaluate the quantitative impact of each aggregation method;

- due to hysteresis and possible stress in late season, the hypothesis of a constant ε for our ecosystem seems violated over entire season (May- October), but holds for half season periods;

- greening and senescence phases of the growing season are best captured using separate model fits and give the most accurate carbon flux estimates (model based on APAR; $R^{2=}$ 0.69 for whole season, R^2=0.79 for green-up phase and R^2=0.77 for senescence phase).

3. Optical indices combined with carbon fluxes, fluorescence-based parameters and pigment analyses for the description and monitoring of a *Fagus sylvatica* L. forest

3.1.Introduction

The understanding of the fundamental “breathing” of the planet is one of the main focus of the scientific community due to its influence on climate change and future climate scenarios. Exploring biomes in natural conditions is a leading target to quantify their contribution as carbon (C) sinks. During the last decades, several methods have been used to monitor ecosystem C uptake like as, for instance, leaf and branch gas exchange [143,144], sap-flow technique [145], field harvesting [146], remote and [99,147,148] proximal sensing [128,149,150], eddy covariance (EC) technique [24,28] and carbon models [151–154]. Among these, the simultaneous use of EC fluxes with proximal and remote sensing brings to the possibility of having direct C flux measurements at high temporal resolution coupled with information at a broader spatial coverage, thus complementing each other weak points and generating a solid integrated dataset [71,101]. However, in this context of integrated approaches, the “ground truthing” at leaf level is needed as validation of optical measurements to monitor the seasonal variability in canopy physiology and to assess how well the optical indices work as proxies of plant physiological status. Fluorescence based parameters and pigment analyses can be used as ground data to verify the accuracy of data coming from different data set. Particularly, chlorophyll fluorescence (Chl F) and non-photochemical quenching (NPQ) are two of the three fates that a photon absorbed by a chlorophyll molecule can undertake. Chl F and NPQ, together with photosynthesis, are processes that occur in competition, thus these parameters can be considered as direct indicators of photosynthesis itself and can provide information about the efficiency of the photochemistry [155]. Likewise, the measurement of changes in pigment pools are essential for testing, validation or estimation of optical indices [156], fluorescence [157] or isoprene emissions [158].

In this framework of different possibilities for the science community to monitor vegetation condition and assess primary productivity, the application of visible and near infrared reflectance (NIR) for identifying plant status developed during the last 30 years allows to recognize the vegetation characteristic from spectral signature [159]. Vegetation indices (VIs) used in this study could be sorted in four categories: indices related to structural traits, to chlorophyll (Chl) content, to the carotenoid content and to water content. Normalized Difference Vegetation Index (NDVI) [43] and Enhanced Vegetation Index (EVI) [160], less affected by saturation issues, were extensively used for global vegetation monitoring. The traditional broadband greenness indices measure green biomass and are mostly able to track the changes of photosynthetic activity just during the growth and the senescence period [120]. They were commonly used as proxy for LAI [161], fAPAR [106], green biomass [121,162] and as input in satellite based diagnostic models [163]. Structural indices are mostly affected by the variations of canopy structure [164] but could fail in predicting diurnal changes in photosynthetic activity. In this context, several studies [165,166] led to the launch of optical indices able to predict short term physiological responses. As known, chlorophyll pigments (Chl *a* and Chl *b*) absorb photons in the blue and in red part of the spectrum. Sims and Gamon [167] explain that the reason of limits of greenness index (as NDVI) is mostly related to saturate absorption at 660-680 nm at relatively low chlorophyll contents. Consequently, other indices have been explored with the aim of tracking changes in chlorophyll. For instance, NDVI red edge [168] and Cl red edge [169], both including red edge (690-750 nm) wavelengths in their formulation, provide not just better predictions of leaf Chl content [167] but also effective proxies for remote estimation of GPP [133]. Chls were not the only pigment cluster considered to study pigment effects on leaf optical properties. Carotenoids, anthocyanins and other accessory pigments were also investigated and a variety of optical indices were developed to track their content [170]. Among these, the Photochemical Reflectance Index (PRI) [171], which measures xanthophyll cycle activity, is used as a proxy of light-use efficiency [136] and the Carotenoid Reflectance Index (CRI_{550}) which measures carotenoid content, is used to detect early stages of stress [35]. The reflectance indices´ responsiveness to changes in pigments and fluorescence may provide accurate estimates of seasonal changes in the photosynthetic flux of vegetation. In the last years several articles have been published on the evaluation of various spectral indices and other methods to retrieve leaf or canopy water content; the water band index (WBI, ratio of reflectance at 900 and 970 nm) is a useful tool to determine sample-specific water content without destructive measurements [165]. In view of all these considerations, VIs have the potentiality to be essential tools in stress detection such as drought monitoring, primary production estimation and other canopy attributes [66].

Considering its C sink potentiality and its socioeconomic impacts, beech forests represent one of the most important ecosystems in Europe [172]. Hence, the investigation of changes in plant ecophysiology and monitoring productivity is a relevant concern from both an ecological and economic point of view. In a mature forest, working in natural conditions could often be problematical due to difficulties in sampling activities, thus proximal sensing method can indicate an effective procedure to monitor canopy functionality in relation to sampling conditions and changes in the seasonal distribution of meteorological factors. For example, water–carbon-cycle interactions, where changes in the frequency of precipitation, could have profound effects on ecosystem productivity

[173], as these factors determine whether the water will be used by plants and transpired, or if it will just run off or evaporate [4].

With this study we want to understand which optical indices better predict the physiological processes occurring in a beech forest ecosystem during two growing season with different meteorological conditions; in particular, the work explores this issue using the integration of different approaches. Principally, the objectives of this study are to:

- Monitor seasonal patterns and variations of C fluxes, pigments pools and chlorophyll fluorescence and their relationship with a number of optical indices;
- Assess which optical indices act as best proxies for monitoring C fluxes and vegetation dynamics in a forest subjected to natural seasonal changes, mainly due to abiotic environmental stress conditions (water status, temperature, CO_2 concentration);
- Evaluate which optical indices are indicators of stress and senescence in healthy and stressed vegetation.

3.2 Materials and Methods

3.2.1 Study site and experimental design

The experiment was carried out at the Collelongo-Selvapiana pure beech forest (Abruzzo region, Central Italy, 41°50′58″N, 13°35′17″E, 1560 m elevation). The site is part of a wider forest area, included in the external belt of the Abruzzo-Lazio-Molise National Park and its structure and conditions are representative of Central Apennine beech forests [174]. According to EUNIS (European Nature Information System) habitat classification, the site is included into the Southern Italian beech forests type. Vegetation is homogeneous and dominated by the European beech (*Fagus sylvatica* L.). Understory is sparse, patchy, and mostly formed by herbs (coverage less than 2%, height less than 50 cm).

The site is equipped with a 28 m scaffold tower geared towards measuring ecosystem H_2O and CO_2 fluxes with the eddy covariance technique since 1993, as previously described by other studies [175,176]. The climate is the Mediterranean montane, with cool to moderately warm summer and cold winters. Mean annual temperature and precipitation measured at the site for the period 1996 – 2015 is 6.9 °C and 1116 mm; soil has a variable depth ranging from 40 to 100 cm and is classified as humic soil [177]. In the area of the experimental site, plant density is 740 trees ha^{-1} (starting from trees with 1 cm diameter at 1.30 m), the basal area is 42.2 m^2 ha^{-1} with a mean diameter at breast height of 25.5 cm and a mean height of 20.7 m (data from the 2012 periodic 5-year stand survey). At the peak of the growing season, Leaf Area Index (LAI) in 2014-2015 is 5.5-5.9 m^2 m^{-2} [178]. Previous works [176,179,180] provide a detailed description of the site and of the stand structure. The Collelongo-Selvapiana experimental site is currently part of the following projects: LIFE+ Smart4Action, eLTER H2020, PRIN 2012 Nitrogen in Mediterranean Forest, CNR IBAF Ecology and Dynamics of Forest Systems. It is also part of international networks as LTER-Europe, Fluxnet, ICP-Forests, ICP-Integrated Monitoring and CONECOFOR programs.

Measurements described in this study started in June 2014 and ended in October 2015 including almost entirely two growing seasons. Four datasets using different techniques were collected: 1) flux measurements (see Mazzenga, [181], PhD thesis presented at the same committee); 2) optical measurements; 3) fluorescence measurements and 4) pigment measurements. While CO_2 fluxes and vegetation reflectance were monitored continuously, fluorescence and pigments were sampled twice a month in 2014 growing season and every month during the 2015 growing season. Additional details on sampling lay-out are provided separately in the following sections.

3.2.2 Flux measurements and meteorological data

Details on the system set-up were described in several papers [176,179,180,182]. Detailed and integrated results on fluxes are presented in a different thesis Mazzenga [181]. Here we summarise the set-up. Ecosystem CO_2 and H_2O fluxes were measured at the site since 1993 using the eddy-covariance technique following the EUROFLUX [183] and then the FluxNet methodology. The experimental set-up consists of a fast-response infrared gas analyzer (LI-7000, LI-COR, Lincoln, NE, USA) and a three-dimensional sonic anemometer (CSAT3, Campbell Scientific, Logan, UT, USA). Air was drawn through the analyzer by a pump (VDO M48 × 25/l, Antriebstechinik GmbH, Germany) installed downstream of the analyzer. Raw data (20 Hz) and basic means (30 min) were stored in a data logger (CR1000, Campbell Scientific). Raw EC data were analyzed using the software package EddyPro (LI-COR, v. 5.2.1) to quality check the data, remove outliers and apply standard corrections to calculate corrected vertical fluxes of CO_2 and H_2O. All fluxes were calculated according to the standardised approaches of FluxNet.

For this study, daily estimates of Net Ecosystem Exchange (NEE, gC m^{-2} d^{-1}) were used. NEE is the flux variable directly measured by the Eddy Covariance technique and its daily total is the sum of the 48 half-hourly values measured during a day, each half-hour being calculated on the basis of the 20 Hz measurements of CO_2 concentration and wind parameters. When one or more half-hourly data were missing or their quality was not acceptable, gap-filling techniques were used to obtain a complete data set. To present a complete seasonal trend, all NEE data were used. However, for correlation analysis among fluxes, ecophysiological parameters and optical indices, NEE values with a quality flag lower than 0.65 were discarded, in order to use more reliable and effectively measured. Along with EC fluxes, the main meteorological variables were measured every 30 min including photosynthetically active radiation (PAR), air temperature (TAir), soil temperature and soil water content, precipitation and other radiation parameters. Details on meteorological measurements set-up have been presented elsewhere [176,179–182].

3.2.3 Optical measurements

The tower was equipped with a multispectral radiometer system MSR16R (CROPSCAN, Inc., Rochester, USA) which was mounted on a metal pole (6 m) on the last floor of the flux tower (28 m) in late June 2014. The radiometer accommodated 14 wavebands (Table 3.1) (14 up and 14 down sensor band pairs), which concurrently measured the reflecting and incoming radiation. Data collected were stored in the data logger controller (DLC). Downward looking sensors had a 28° field of view (FOV) and detected reflected radiance in the wavebands reported in Table 3.1, while the incident irradiance was measured through a flashed, opal glass, cosine diffuser.

Table 3.1. Multispectral Cropscan MSR16R system specifications.

Cropscan Multispectral Radiometer System (MSR16R) Bands			
Band number	Channel name	Center wavelength	Bandwidth (nm)
1	R510	509.3	10.6
2	R530	529.9	8.4
3	R550	549.0	8.3
4	R570	569.8	9.6
5	R650	647.1	37.1
6	R670	670.4	10.2
7	R710	709.9	10.3
8	R720	719.7	10.4
9	R740	740.9	9.9
10	R750	750.1	10.6
11	R850	851.6	42.1
12	R860	860.7	10.7
13	R900	901.0	10.4
14	R970	971.0	10.7

Since the diameter of the field of view is half of the height of the radiometer over the target, the down-facing sensors received direct reflected irradiance from surfaces within a circular conic region having 14 m of diameter. In complex canopy ecosystems like forests, reflected irradiance could arrive from leaves not too far below the radiometer or leaves much lower, when there are openings above them directly to the radiometer. Spectral data were collected during the growing seasons 2014 (26 June - 3 November) and 2015 (24 April 2015- 12 October). The radiometer was set in a standalone operation collecting optical measurements daily from 6 a.m. to 6 p.m. Downward irradiance and upward radiance were stored every 5 minutes during season 2014 and every 10 minutes during season 2015. In this study, only scans that met the criteria IRR ≥ 300 W/m^2 and Sun angles ≤ 50 degrees were considered. The Cropscan multispectral radiometer reflectance was calculated as the ratio between downward and upward sensor readings. Sensor temperature corrections, up-sensor cosine response correction and radiometric calibration constants were applied before the final calculation of the basic equation abovementioned. In order to reduce solar angle effects, reflectance data from 11 a.m. to 13 p.m. (local solar time) were used to compute VIs indices (Table 3.2) used in our analysis. R indicates reflectance, and the following number indicates the waveband in nm.

Table 3.2. Vegetation indices computed in this study. R stands for reflectance and the following number indicates the given wavelengths (e.g., R750 is the reflectance at 750 nm).

Vegetation index	**Formula**	**Reference**
Structural indices		
Simple Ratio (SR)	R750 / R670	[184]
Enhanced Vegetation Index 2 (EVI 2)	2.5 x (R750 - R670) / (R750 + 2.4 x R670 + 1.0)	[162]
Difference Vegetation Index (DVI)	R 750 - R 670	[185]
Normalized Difference Vegetation Index (NDVI)	(R750 - R670)/(R750 + R670)	[43]
Renormalized Difference Vegetation Index (RDVI)	(R750-R670)/(R750+R670) x 1/2	[164]
Modified Chlorophyll Absorption Ratio Index (MCARI 1)	1.2 x [2.5 x (R750-R670)-1.3 x (R750 - R550)]	[164]
Modified Simple Ratio (MSR)	(R 750 / R 670 - 1)/(R 750 / R 670 + 1) x 1/2	[164]
Optimized Soil-Adjusted Vegetation Index (OSAVI)	(1.16) x (R750 - R670)/(R750 - R670 + 0.16)	[186]
Wide Dynamic Range Vegetation Index (WDRVI)	(0.1x R750–R670)/(0.1xR750+R670)	[187]
Chlorophyll indices		
Simple Ratio red edge (SR red edge)	R750/ R710	[188]
Simple Ratio green (SR green)	R750 / R55	[189]
NDVI Red Edge	(R750-R720)/(R750+R720)	[168]
Red edge chlorophyll index (Cl red edge)	(R750/R720)−1	[46]
NDVI green	(R750-R550)/(R750+R550)	[190]
Green chlorophyll index (Cl green)	(R750/R550) – 1	[191]
MCARI 2	[(R750 - R720) - 0.2 x (R750 - R550)] (R750/R720)	[133]
Transformed Chlorophyll Absorption Ratio Index (TCARI)	3[(R720 - R670) - 0.2x (R720 - R550) x (R720/R670)]	[192]
MERIS terrestrial chlorophyll index (MTCI)	(R750 - R720)/(R720 - R670)	[193]
Difference Ratio (DR)	(R750 - R720)/(R750 - R681)	[194]
Carotenoid indices		
Carotenoid Reflectance Index (CRI)	(1/R510) - (1/R550)	[35]
Photochemical Reflectance Index (PRI)	(R530-R570) /(R530+R570)	[171]
Structure Insensitive Pigment Index (SIPI 2)	(R750-R550)/(R750-R670)	[195]
Plant Senescence Reflectance Index (PSRI)	(R670-R510)/R750	[196]
Water Content		
Water Band Index (WBI)	R900/R970	[197]

3.2.4 Leaf level measurements

During the two years of study (2014 and 2015), a number of field campaigns were carried out in order to collect different kind of leaf level measurements: 1) fluorescence measurements, 2) pigment measurements and 3) structural measurements (% N). Samples were collected within 2 hours from solar noon, ensuring the reduced diurnal variability during the sampling periods. We selected six labelled trees having branches accessible from the flux tower at 26 m (top of the canopy). On average, five branches were cut from the labelled trees at each campaign, labelled and immediately soaked in the water for sampling. Leaves were kept as close to their original orientation as possible to maintain the original illumination conditions during sampling. For each branch, three leaves were randomly selected and labelled. The leaf scale measurements were performed on the selected three leaves for every branch: first, on one half of the leaf, fluorescence measurements were collected; secondly, on the other half of the leaf, one disk (1.32 cm^2) was sampled for pigment analyses and a second disk (1.32 cm^2) was sampled for structural indices assessment (Leaf Mass Area, LMA and Relative Water Content, RWC, data not shown). Disks belonging to three different leaves of the same branch were immediately packed in aluminum paper, frozen in liquid nitrogen and preserved at -80 °C. Sampled leaves (the ones that were used for fluorescence measurements) and supplemental leaves from each branch were additionally packed and stored in liquid nitrogen and later transferred into a −80 °C freezer for long-term storage. More details are provided in the following sections.

3.2.4.1. Fluorescence measurements

Fluorescence parameters were monitored on fully expanded and exposed leaves using a miniaturized pulse amplitude-modulated fluorometer (Mini-PAM; Heinz Walz GmbH, Effeltrich, Germany) between 10:00 and 12:00 h. The fluorometer fibre optic was kept at a fixed angle to ensure measurements repeatability and an average of 20 leaves were sampled for each campaign.

The quantum yield of PSII in light adapted state (φ_{PSII}), an indicator of the photosynthetic efficiency of photosystem II, was obtained as:

$$(\varphi_{PSII}) = \frac{\Delta F}{F'_m} = \frac{F'_m - F}{F'_m} \tag{3.1}$$

where Fm’ is the maximum fluorescence yield with all the PSII reaction centres in the reduced state obtained by superimposing a saturating light flash during exposure to actinic light and F is the fluorescence yield at the actual reduction state of PSII reaction centres during actinic illumination.

The electron transport rate (ETR) (μmol m^{-2} s^{-1}), which provided a more direct estimation related to photosynthetic activity (Baker, 2008), was calculated based on chlorophyll fluorescence measurement of φ_{PSII} parameter employing the following equation:

$$ETR = \varphi_{PSII} \times PPFD \times 0.5 \times 0.84 \tag{3.2}$$

Where incident PPFD was obtained by a PAR quantum sensor positioned at measurements position, 0.5 is a factor that accounts for the partitioning of energy between PSII and PSI and × 0.84 is the leaf absorbance coefficient [155].

The potential efficiency of PSII photochemistry was determined on three leaves for each branch after at least 30 min of dark acclimation as Fv/Fm=(Fm-Fo)/Fm, where Fv represents the variable fluorescence in the dark, Fo is the minimum fluorescence yield in the dark and Fm is the maximum fluorescence yield in the dark after application of a saturation flash of light that completely closes all the PSII reaction centres. Non-photochemical quenching (NPQ) was calculated according to the Stern-Volmer equation as reported by Bilger and Bjorkman (1990):

$$NPQ = \frac{(F_m - F_m')}{F_m'} \tag{3.3}$$

3.2.4.2. Pigment determinations

The speciation of photosynthetic pigments was performed according to the method reported by Castagna et al. [198] and modified in Di Baccio et al.[199]. Leaf discs of known area (1.32 cm^2) were punched from leaves previously utilized for gas exchange measurements, frozen in liquid N_2 and stored at −80°C until use. Frozen samples were homogenized under dimmed room light in 100% HPLC-grade acetone with 1 mM Na-ascorbate, filtered through 0.2-µm filters (Sartorius Stedim Biotech, Goettingen, Germany) and immediately analyzed. The analysis was performed by HPLC (HPLC P4000, Thermo Fisher Scientific, Waltham, MA, USA)) using a non-endcapped column (5 µm particle size, 250 × 4.6 mm Ø; (Zorbax ODS column, Chrompack, Raritan, NJ, USA). Pigments were eluted using 100% solvent A (acetonitrile/methanol, 75/25, v/v) for the first 15 min, followed by a 2.5-min linear gradient to 100% solvent B (methanol/ethylacetate, 68/32, v/v), which continued isocratically until the end of the cycle. The separation cycle was 32 min with a flow rate of 1 mL min^{-1}. The column was allowed to re-equilibrate in 100% solvent A for 10 min before the next injection. Pigments (chlorophyll *a*, Chl *a*; chlorophyll *b*, Chl *b*; lutein; neoxanthin; violaxanthin; antheraxanthin; zeaxanthin and β-carotene) were detected by their absorbance at 445 nm, and quantified by injecting known amounts of pure standards (Sigma-Aldrich, Milan, Italy) into the HPLC system. The de-epoxidation index (DEPS index) was calculated according to the following equation: [(A/2) + Z]/(V + A + Z) × 100 (A, anteraxanthin; Z, zeaxanthin; V, violaxanthin). The carotenoid content shown in the "Results and Discussions" section was calculated as the sum of lutein, neoxanthin, VAZ and β-carotene.

For the construction and validation of calibration curves, evaluation of total chlorophyll (Chl *a* + Chl *b*) and caroteinoid contents were also measured spectrophotometrically according to the method described by Wellburn [200]. Briefly, leaf tissue samples (1.32 cm^2) were homogenized with 80% (w/v) cold acetone, centrifuged at 10,000 x g per 5 min at 4°C, and the absorbance of the supernatant was read at 663.2, 646.8 and 470.0 nm.

3.2.4.3 Leaf nitrogen content

Leaf samples of each branch (n>15) were oven dried until constant weight and subsequently ground to a fine powder. About 3–4 mg of powder was used for the determination of nitrogen content (N) using an elemental analyser (Model NA 1500, Carlo Erba, Milan, Italy).

3.2.5. Data analysis

One-way ANOVA was used to test differences among meteorological variables between July 2014, July 2015 and July 1996-2015. We additionally used multiple post hoc comparisons (Tukey test) to determine if years significantly differed from each other at a significance level of $p \leq 0.001$.

A direct linear regression between spectral indices and carbon fluxes was assumed. The difference among the slopes and the intercepts of the relationships between VIs and NEE for different years was evaluated through analysis of covariance (ANCOVA). Statistics for each relationship (coefficient of determination - R^2, root mean square error - RMSE, number of observations – *n*, probability value – *p* and Pearson correlation coefficient - *r*) were computed to evaluate the performance of the fit of the different indices.

Differences between spectral indices and biophysical parameters between 2014 and 2015 selected months of the two growing seasons were evaluated by one-way analysis of variance (ANOVA) or a *t*-Student test. Separation of means was performed by Fisher's least significance difference (LSD) test at a significance level of $p \leq 0.05$. These criteria were also used to evaluate differences in leaf pigment contents between the 2014 and 2015 growing seasons.

3.3Results and Discussions

3.3.1 Characterization of meteorological variables, temporal patterns of fluxes, pigment and fluorescence measurements

The thermopluviometric diagram (Figure 3.1) reported the seasonal course of the air temperature (T, °C) and precipitations (mm day $^{-1}$) for 2014 (top panel) and 2015 (bottom panel) at Collelongo site.

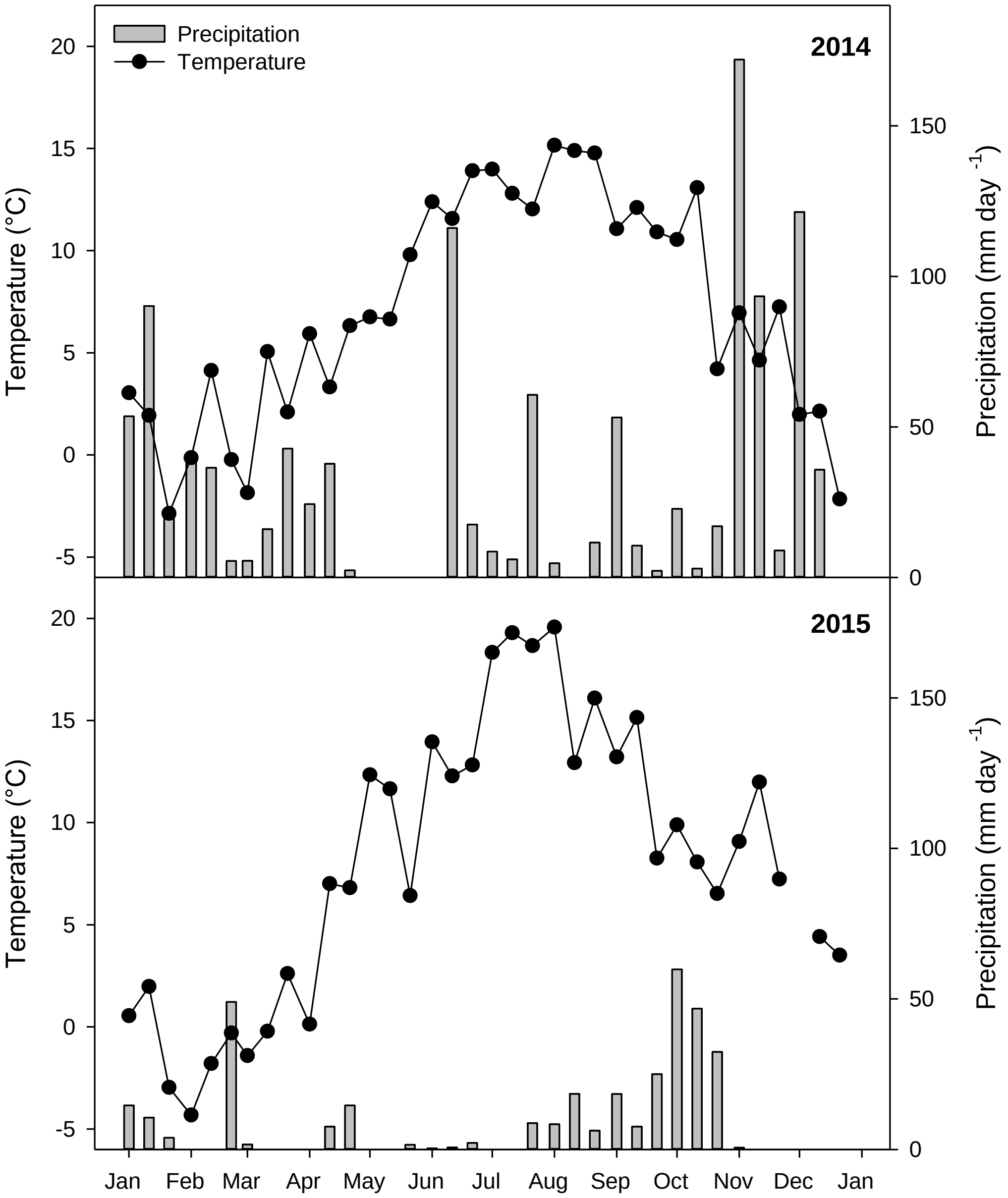

Figure 3.1. Seasonal variations of air temperature and rainfall for 2014 (top panel) and 2015 (bottom panel). Data of air temperature and rainfall are presented, respectively, as decades averages and the decades sum. Gaps occurred for temperature during the first decade of December 2015 and for precipitations in November and December 2015.

Higher air temperature and lower precipitations were generally measured during 2015 as compared to 2014. These differences were especially evident in July, when monthly mean air temperature was 12.9±2.9 °C for 2014 and 18.8±1.4 °C for 2015, while the monthly mean precipitation was 75.3 mm day $^{-1}$ for 2014 and 9.0 mm day $^{-1}$ for 2015 (Figure 3.1; Table 3.3).

Table 3.3. July monthly means and standard deviation for 19 years period (1996-2015) and the two years of study, 2014 and 2015. Air temperature (T average,°C), Vapor Pressure Deficit (VPD; hPA), Soil Water Content (SWC; %) and maximum for air temperature (T max; °C) are presented as the average of July measurements while Precipitation (mm) are presented as sum of July measurements.

Year	**Air temperature (°C)**		**Precipitation (mm)**		**VDP (hPA)**		**SWC (%)**		**T max (°C)**	
	mean	σ	Sum	σ	mean	σ	mean	σ	mean	σ
Mean 1996-2015	15.9	0.62	36	1.01	11.0	2.0	-	-	20.8	0.62
2014	12.9	2.93	75	-	4.2	1.8	38.1	1.3	17.3	3.84
2015	18.7	1.40	9	-	7.3	2.5	31.8	1.2	24.3	2.23

Meteorological differences between the two years of study were also reflected in seasonal SWC determined at 20 cm of depth (Figure 3.2) and VPD (Figure 3.3). The period between January and middle April showed different SWC trends in 2014 and 2015, until the second decade of April, when the two values overlap. After that, similar trends were measured, with a clear shift towards the end of the seasons for 2014. Apart from the overlaps of the SWC values in the second decade of April in 2014 and 2015, the SWC in 2015 was generally lower than in 2014, with the exception of a period between October and November (Figure 3.2). In particular, we observed a sharp decrease in soil water availability starting in June (Figure 3.2). On the other hand, during 2015, the sudden decrease started earlier in the season (middle of April). Moreover, in 2015, the SWC remained low until late summer, while in 2014 SWC increased again at the beginning of August. A steep increase in SWC occurred on the last decade of October for 2014 and at the middle of October for 2015. In agreement with the lower values of SWC during 2015, figure 3.3 showed higher values of vapour pressure deficit (VPD) during the same year. Particularly, in 2015, July averages of VPD were clearly larger than those registered in the same period of 2014.

Hence, all the meteorological variables investigated in our study highlighted a clear difference between the two years of study. This difference is especially evident in the month of July and could be summarized as higher temperature, reduced precipitations, lower SWC and higher VPD values during July 2015 compared to July 2014. ANOVA analysis confirms that, for T average, T max, SWC and VPD, statistical significant differences were found between July 2014 and 2015 and between each year of study and the 19 years period (1996-2015) when the month of July is compared (Table

3.3). When values of the 19 years period were not available (SWC), we performed a *t*-test that also indicates a statistical difference between the means of the two years of study (2014 and 2015) (Table 3.3).

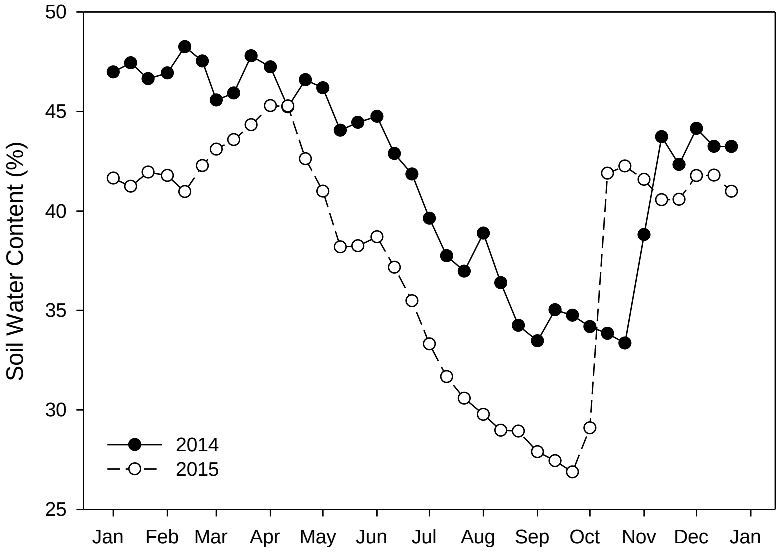

Figure 3.2. Seasonal variations of Soil Water Content (SWC) determined at 20 cm of depth and expressed as percentage (%) at Collelongo site. Values are presented as decades averages in black dots and solid line for 2014 and white dots and dashed line for 2015.

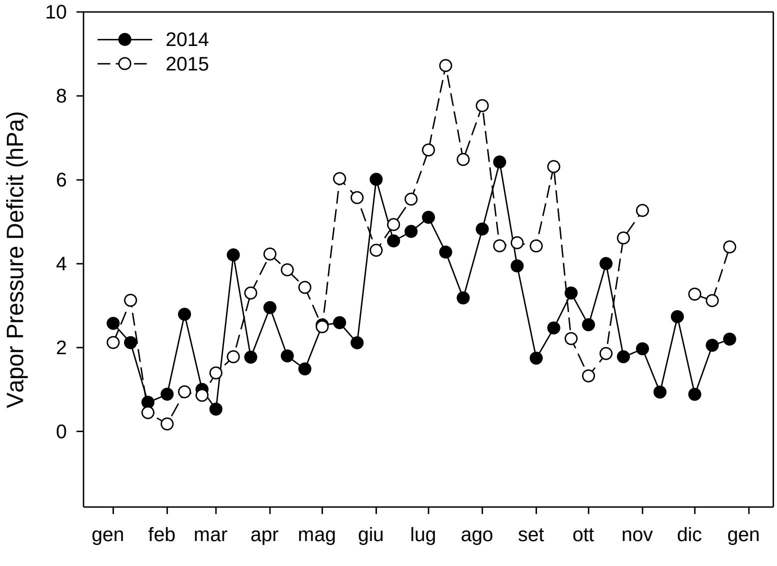

Figure 3.3. Seasonal trends of Vapor Pressure Deficit (hPa) gapfilled with MDF at Collelongo site. Values are presented as decades averages in black dots and solid line for 2014 and white dots and dashed line for 2015. November values for 2015 were identified as outliers and removed.

The metereological differences observed between 2014 and 2015 were supported also by the seasonal variations of NEE measured with the eddy covariance technique. Collelongo beech forest acted as a net CO_2 sink between the half of May and the last decade of October 2014. A slight anticipation of both the opening and the closing of the season was observed in 2015 as compared to 2014; in fact, the forest started to be a sink from the beginning of May until middle October 2015 (Figure 3.4). In 2015, for the month of July until the beginning of August a lower sink capacity of the forest is evident (Figure 3.4), indicating a lower quantity of absorbed C in that month compared to the same period of 2014. The maximum net CO_2 flux rates were recorded during the last decade of June for both the studied years. Over the year, Collelongo forest carbon sink capacity was higher in 2014 (-757 gC m^{-2} y^{-1}) than in 2015 (-608 gC m^{-2} y^{-1}).

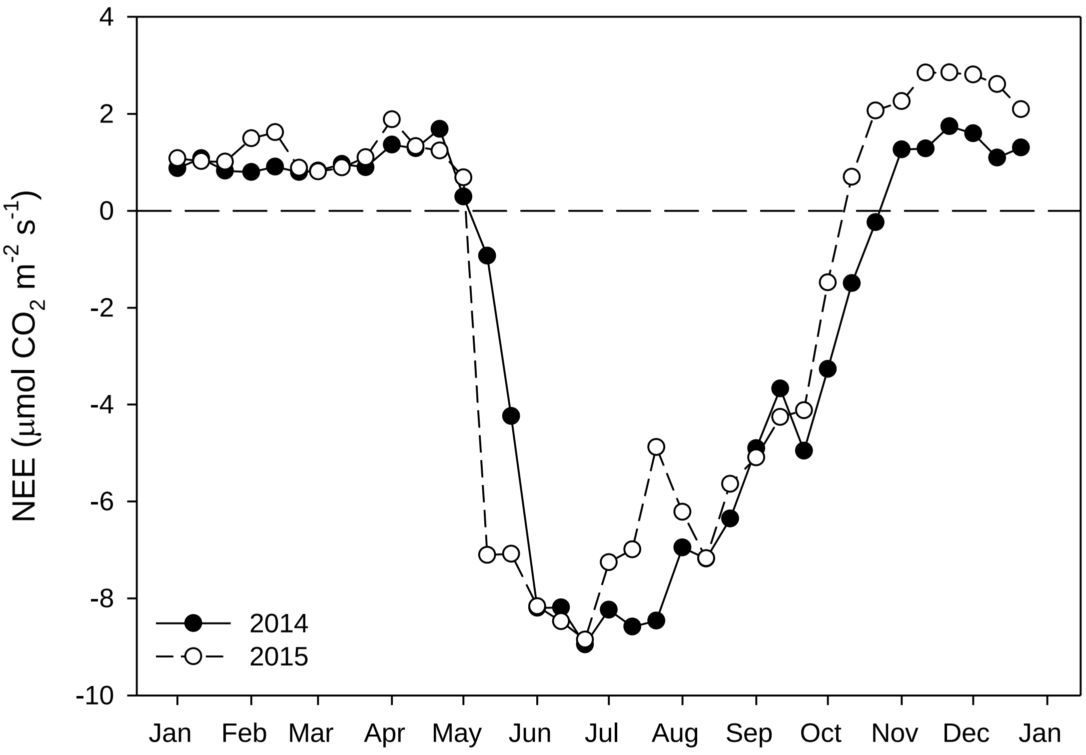

Figure 3.4. Seasonal variations in NEE at Collelongo site. Values of NEE are presented as decade averages in black dots and solid line for 2014 and white dots and dashed line for 2015.

The content of total Chl (Chl *a* + Chl *b*) of *Fagus sylvatica* L. leaves was significantly different between 2014 and 2015 seasons only in July (Figure 3.5a). In particular, Chl *a* + Chl *b* was 1.3 fold lower in July 2015 than in July 2014. However, these modifications were not sufficient to alter the Chl *a*/ Chl *b* ratio in the same period (Figure 3.5b). This ratio increased (+ 26%) in October 2015 compared to October 2014 and the variation of Chl *a*/ Chl *b* at the end of the growing season could be related to the earlier occurrence of senescence process in the beech plants grown in 2015 season compared to 2014. Indeed, Zhang et al. [201] showed that in higher plants the chlorophyll degradation, occurring in senescence conditions, is preceded by the conversion of Chl *b* to Chl *a* with a consequent increase in Chl *a* to Chl *b* ratio. Besides, variations in Chl *a*/ Chl *b* ratio are related to different amount of light harvesting complex (LHCs) in the photosystem II antennas, since these complexes are the most enriched in Chl *b* [202]. Such modifications are consistent with adaptation to different light exposure and stress conditions [178,203,204].

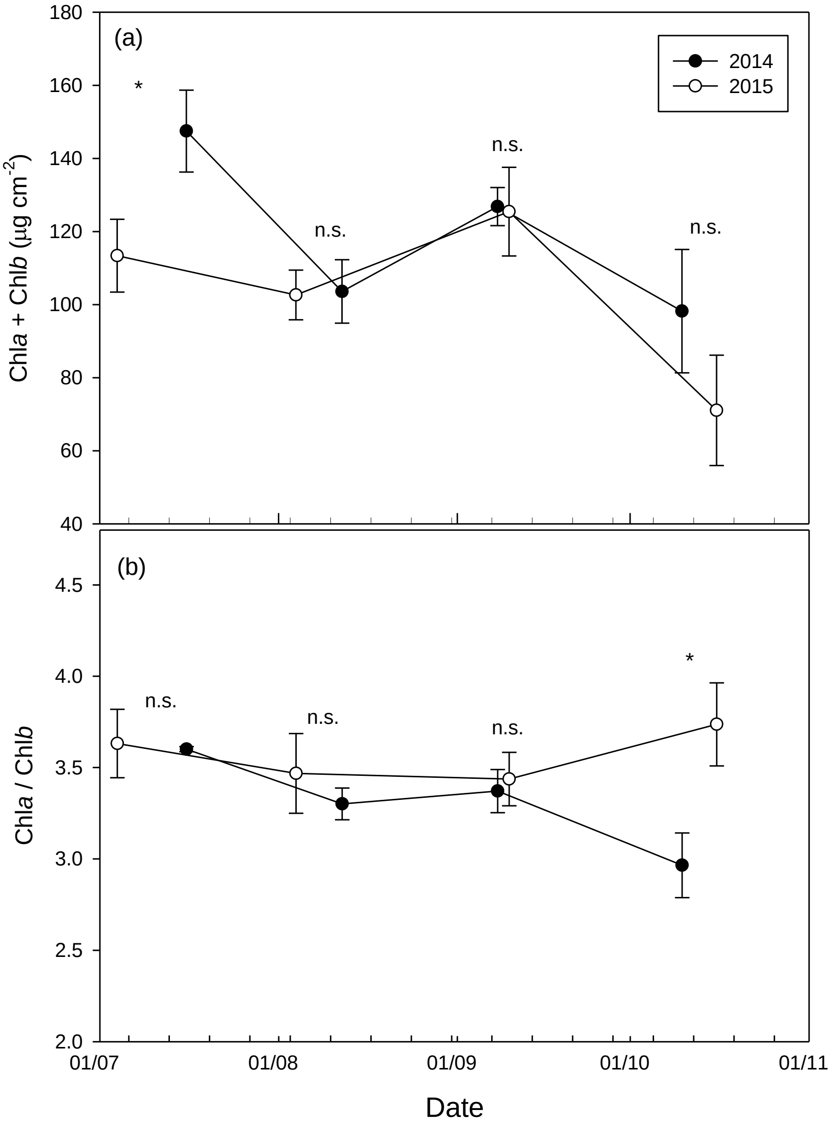

Figure 3.5. Total chlorophyll (Chl *a* + Chl *b*) (a) and Chl *a* to Chl *b* ratio (b) in leaves of *Fagus sylvatica* L. during the two growing season 2014 (black circles) and 2015 (white circles). Leaves were collected at the top of the canopy (26 m). Each value represents the mean of at least four ($n = 4$) biological replicates ± SE. For each month, asterisks represent significantly different data (*t*-test, $p \leq 0.05$); n.s. = not significant, *≥0.05. Different letters mean significantly different results at the *p*-value indicated.

The leaf carotenoid content (Fig. 3.6) showed significant differences in July and October, at the beginning and at the end of the growing seasons investigated, although in September the *p* value which defined the variation between 2014 and 2015 was close to the significant value (0.058). The higher (1.6-fold) carotenoid levels reached in July 2015 compared to the same month of 2014 seemed to confirm the enhanced defense capabilities gained by plants through the increased synthesis of these photoprotective pigments. The most rapid decrease in carotenoid contents in the 2015 reflected the anticipated closure of the season with the senescence of 2015 compared to 2014 (Fig. 3.6).

In particular, as regard the different type of carotenoids analyzed, the lutein content varied only at the end of the growing season, with a 31% reduction in October 2015 in comparison with October 2014 (Figure 3.7a).

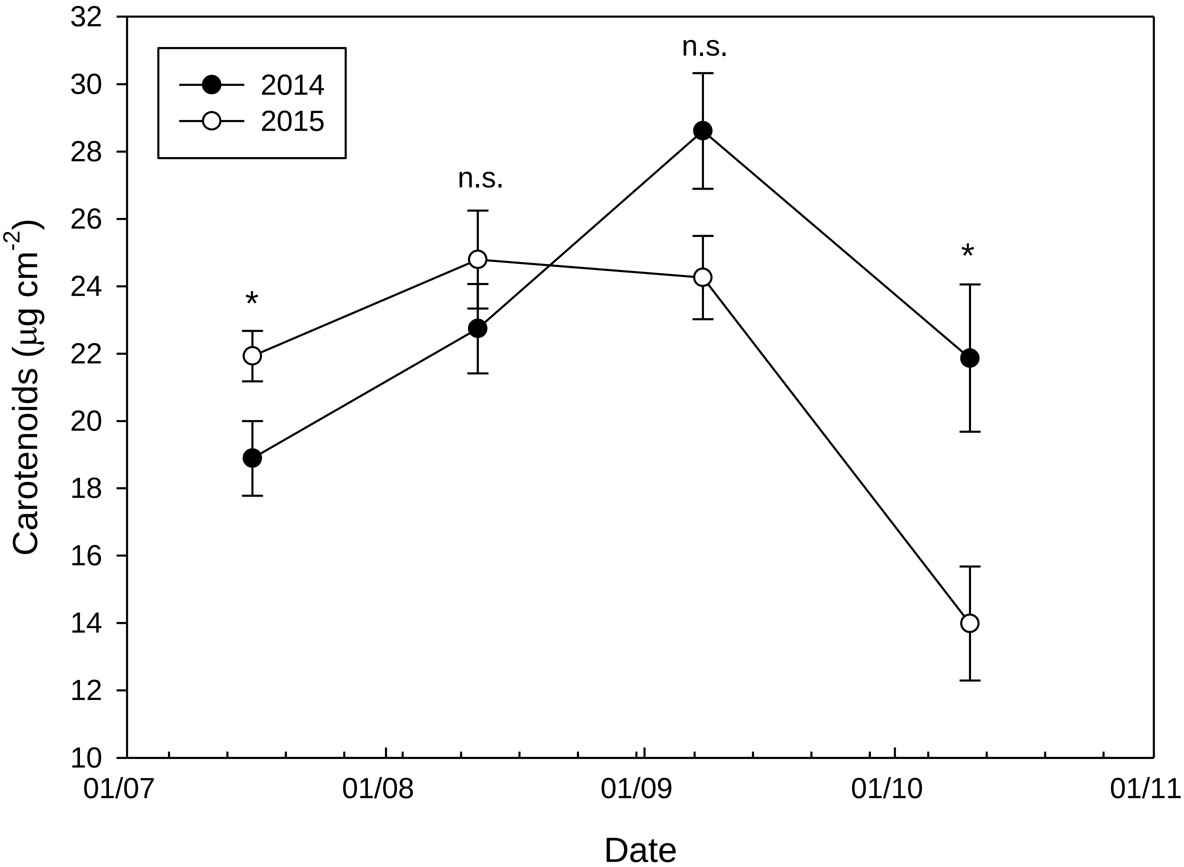

Figure 3.6. Leaf contents of carotenoids in the beech forest of Collelongo during the two growing season 2014 (black circles) and 2015 (white circles). Each value represents the mean of at least four (*n* = 4) biological replicates ± SE. Statistical analysis is as in Fig. 3.5.

Lutein is the most abundant xantophyll in the photosynthetic apparatus of higher plants and it has a fundamental role in the protein folding and quenching of chlorophyll triplet in the major LHCII antenna complex [205]. Its stability during the growing season of both 2014 and 2015 revealed a good tolerance to temperature and drought stress, and its higher level in October 2014 can be related to an enhanced photoprotection action as compared to the same period of 2015 [206].

The ß-carotene changed in July and September, being 2.4-fold higher and 2.5-fold lower in 2015 than 2014, respectively (Fig. 3.7b). Together with Chl *a*, ß-carotene is bound to the photosynthetic reaction center complexes, where it has the double role of accessory pigment and antioxidant / photoprotection molecule. Its increase in the relatively hot and dry July 2015 might be related to the activation of antioxidant defense systems [207,208], while its decrease in autumn is probably related to senescence processes [206].

The VAZ pool showed variations only in October, with a 36.4% decrease in 2015 (Fig. 3.7c). The amounts of xanthophylls involved in the xanthophylls cycle seemed not to be affected by impairments during the growing season of the two years investigated. However, their degradation in the senescence phase occurred more rapidly in 2015 than in 2014.

In summer (July-August) the neoxanthin was about 1.3-fold higher in 2015 than 2014 (Fig. 3.7d). The neoxanthin is bound to the light harvesting proteins together with lutein and violaxanthin [205] and it is the precursor of violaxanthin and abscissic acid (ABA, [209]). Thus, the neoxanthin variations observed during summer in the two years investigated might be attributed to structural and functional changes of the photosynthetic apparatus; its decline in October of both 2014 and 2015 was probably due to the increased synthesis of ABA with the beginning of the senescence phase.

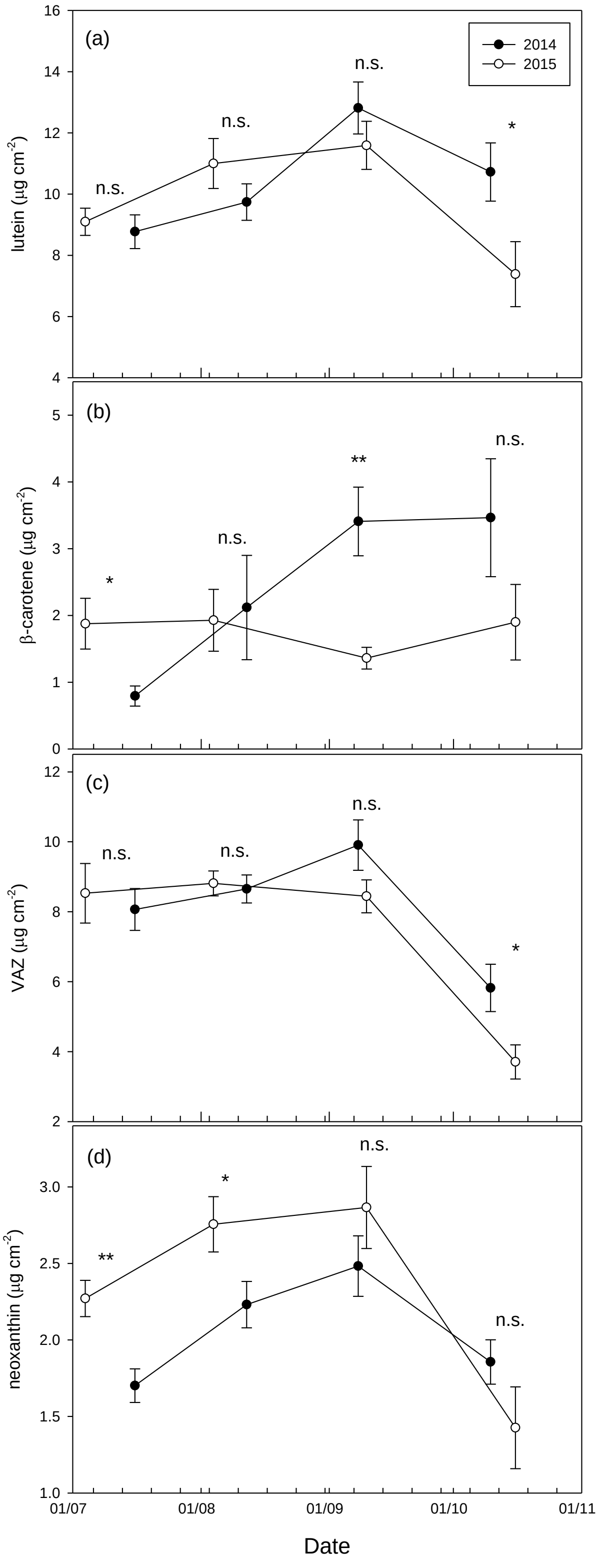

Figure 3.7. Leaf contents of lutein, ß-carotene, VAZ (Violaxanthin+Antheraxanthin+Zeaxanthin) pools and neoxanthin in the beech forest of Collelongo during the two growing season 2014 (black circles) and 2015 (white circles). Each value represents the mean of at least four (*n* = 4) biological replicates ± SE. Statistical analysis is as in Fig. 3.5.

The DEPS index was higher in August 2014 (57.5%) than in August 2015 (48.5%), whereas it increased in October 2015 (53.5%) compared to October 2014 (36.8%, Figure 3.8a). When near or over the 50% the DEPS index indicates high activation of the xanthophyll cycle for the alleviation of excessive excitation energy under stress or senescence and degeneration processes [198,199,206,208,210].

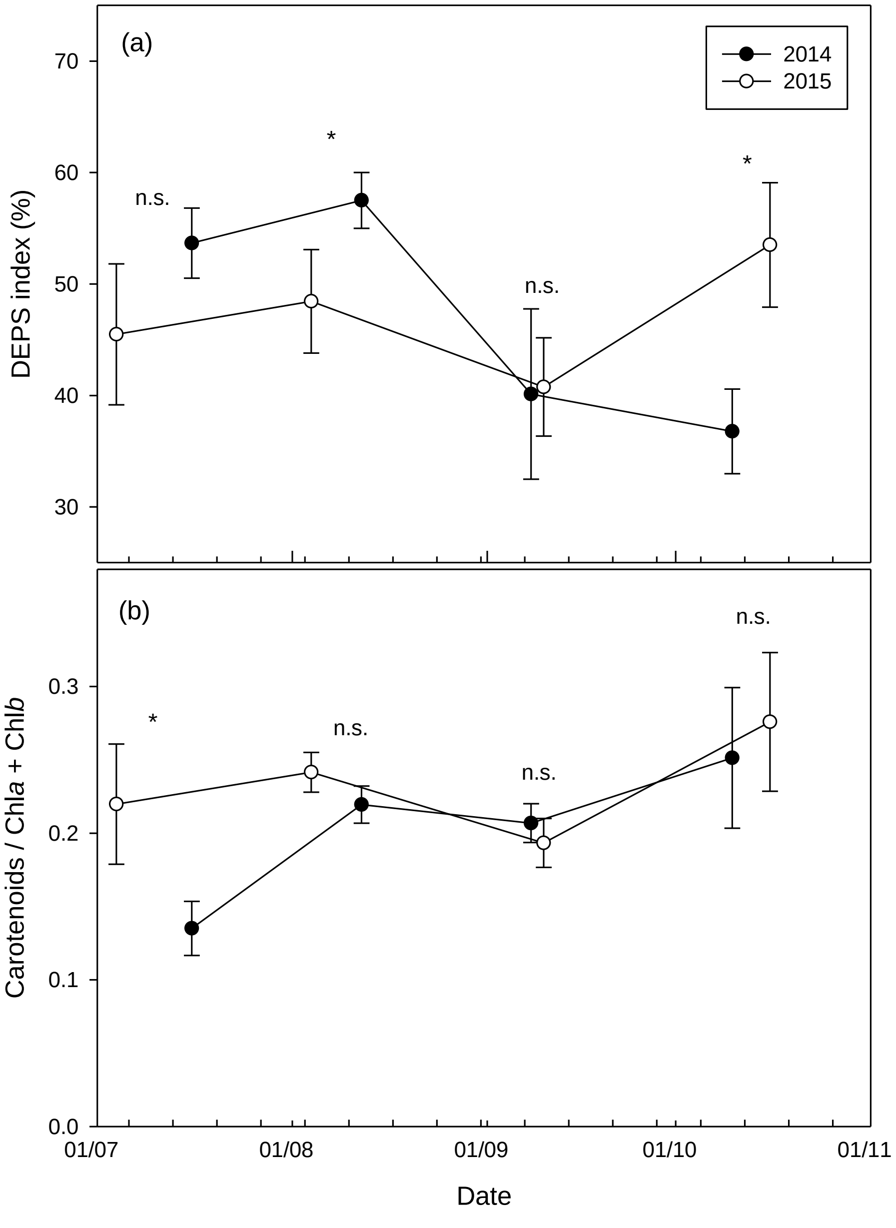

Figure 3.8. The de-epoxidation index (DEPS) and carotenoids to total Chl ratio in the leaves of the beech forest of Collelongo during the two growing season 2014 (black circles) and 2015 (white circles). Each value represents the mean of at least four (*n* = 4) biological replicates ± SE. Statistical analysis is as in Fig. 3.5. The DEPS index was calculated according to the following equation: [(A/2) + Z]/(V + A + Z) × 100 (A, anteraxanthin; Z, zeaxanthin; V, violaxanthin).

The carotenoids to total Chl ratio was 1.6-fod higher in July 2015 than in July 2014 (Figure 3.8b). The Car/Chl tot represents a marker of stress charged to the photosystems [211] and its increase due to a relative enhancement of the carotenoid amount is usually related to stress conditions because of the antioxidant action of these pigments [212] and their role in the energy dissipation mechanism [208]. The increase of Car/Chl tot in July 2015 is consistent with the fluorescence measurements (Figure 3.8 and 3.9). The actual photon yield of PSII photochemistry in the light (Φ_{PSII}) was significantly higher in July 2014 than July 2015, while during the other seasonal period we did not observe significant differences between the two years (Figure 3.9a). Inter-annual and seasonal changes of Φ_{PSII} were reflected in changing photosynthetic electron transport and non-radiative energy dissipation (NRD) capacity, as suggested by the electron transport rate (ETR) and the non-photochemical quenching (NPQ) (Figure 3.9b and c). Particularly, ETR was higher and NPQ lower in July 2014 than July 2015. These results indicate that during the relatively hot and dry July 2015 plants reduced the photosynthetic electron transport and increased the proportion of adsorbed energy to be dissipated as heat in order to avoid photoinhibition and photodamage at PSII. These results are in agreement with the lower NEE observed in July 2015 than July 2014 (Figure 3.4) and with the increased Car/Chl tot ratio (Figure 3.8b). Then, ETR and NPQ decreased during the late season (September-October), due to the onset of the senescence phase. Interestingly, ETR showed a higher value in October 2014 than October 2015, supporting the evidence of an anticipated senescence in October 2015 (Figure 3.4).

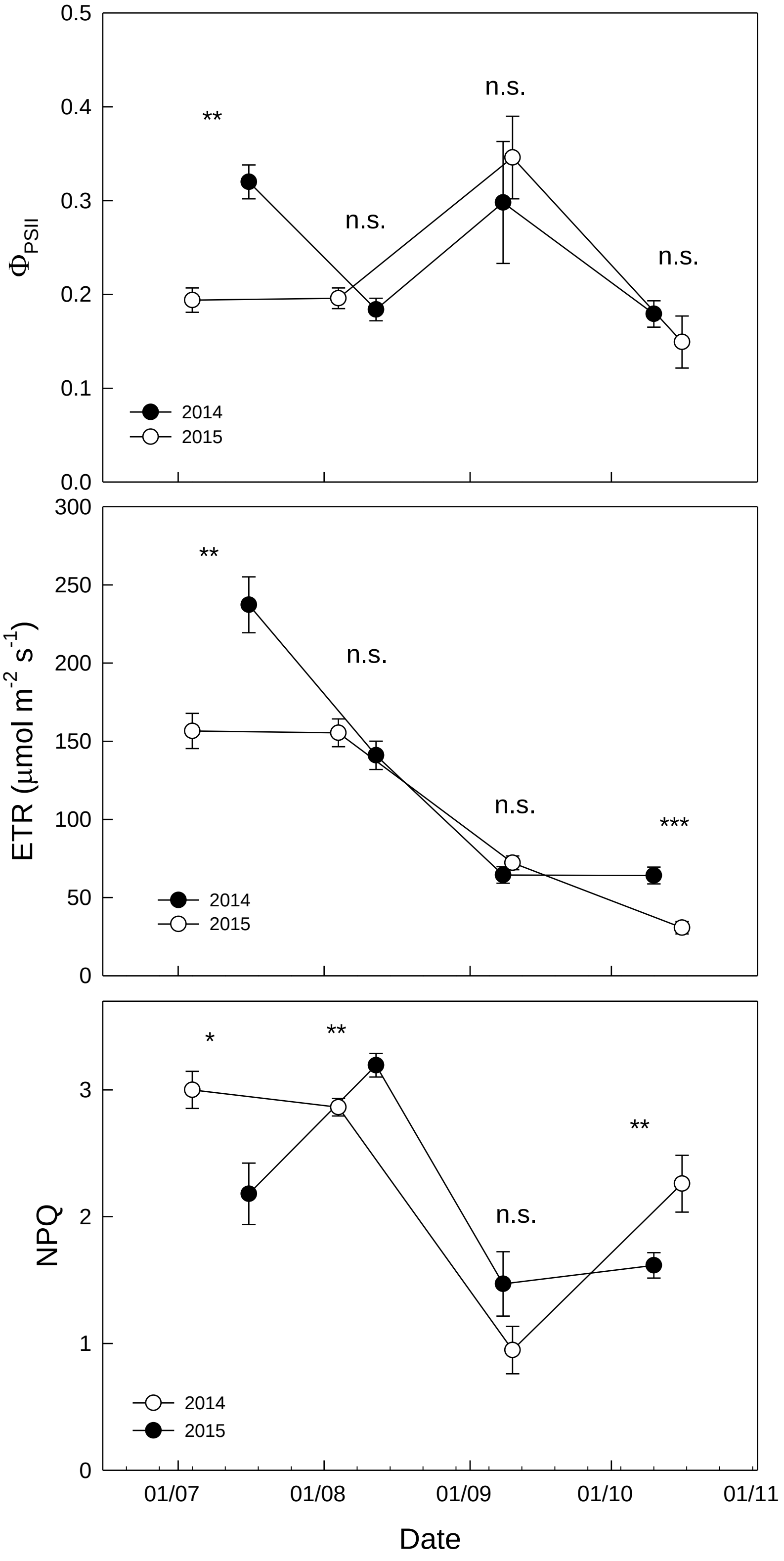

Figure 3.9. The actual photochemical efficiency of PSII (Φ_{PSII}), the electron transport rate (ETR) and the non-photochemical quenching (NPQ) in leaves of the beech forest of Collelongo during the two growing season 2014 (black circles) and 2015 (white circles). Each value represents the mean of at least 15 fluorescence measuements ± SE. Statistical analysis is as in Fig. 3.5.

3.3.2. Relations between spectral indices and NEE, pigment concentration, fluorescence parameters and nitrogen

According to Wu et al. [161], C fluxes could be appropriately estimated by correlating *in situ* flux measurements with a single vegetation index (VI), as demonstrated in several cases. In our study, with a rather limited number of spectral bands from a multispectral radiometer, it was possible to calculate several VIs to monitor the carbon dioxide (CO_2) fluxes between the forest ecosystem and the atmosphere. Recently, several studies explored the relationship between CO_2 fluxes and VIs in rice [213], wheat [161] and maize fields [123], mountain grasslands [118,124,127,128] and chaparral ecosystem [214]. Although not so extensive as in crops and grasslands, similar researches were carried out also in mixed deciduous forests [93,215], larch forest [216] and holm oak forest [147]. For our deciduous beech forest, the statistics of the linear regressions between daily carbon fluxes (NEE) versus spectral indices are reported in Table 3.4. The ANCOVA test showed significant differences between the slopes and the intercepts of each relationship and consequently statistics were considered separately for both the years. Almost all the regressions were highly significant ($p < 0.0001$), except for WBI and CRI 550 for 2015. On the other hand, correlations involving TCARI, SIPI 2 and PSRI were statistically significant at p value < 0.001.

R^2 values were consistently higher for 2014 as compared to 2015, except for PRI. One explanation, could be that the Cropscan sensor was not operating during the last two decades of October 2015, thus missing the end of the growing season mainly characterized by senescence of the canopy. A higher correlation was expected expanding our experiment (and spectral dataset) towards whole early spring and senescence season, thus providing a wider seasonal variability.

For 2014, the indices that better tracked C fluxes were MCARI 2, EVI 2, DVI, RDVI, MCARI 1, SR, SR red edge and CL red edge with a R^2 ranging from 0.804 to 0.754 and a RMSE spanning from 1.262 to 1.415 gC m^{-2} d^{-1}, respectively (Table 3.4, bold character). During 2015, SR red edge, RDVI, EVI 2, DVI, MCARI 1, NDVI green, SRgreen and CL green explained between 43% and 63% of the variability of NEE with RMSE varying between 1.526 and 1.826 gC m^{-2} d^{-1}(Table 3.4, bold character). To better analyze the ability of the spectral indices in tracking C dynamics and the afore mentioned differences between the two year of study, the experiment focused on those indices that, concurrently for both 2014 and 2015, were the best predictor of NEE. The selected five indices were EVI 2, RDVI, DVI, SR red edge and MCARI1. Figure 3.10 presents the relationships between the daily NEE and the selected indices, focusing on July, August, September and October.

Table 3.4. Summary of the statistics of the linear regressions between NEE and vegetation indices computed for this study. Pearson correlation coefficient (*r*), coefficient of determination (R^2), root mean square error (RMSE), number of observations (*n*) and probability value (*p* value) are presented for 2014 and 2015. NEE is the daily NEE estimates (gC m^{-2} d^{-1}) while vegetation indices are midday averages from 11 a.m. to 13 a.m. The indices which performed the higher accuracy are indicated in bold.

	2014					**2015**				
Vegetation indices	*r*	R^2	RMSE	*n*	*p* value	*r*	R^2	RMSE	*n*	*p* value
Structural indices										
SR	**-0.873**	**0.763**	**1.389**	**113**	**< 0.0001**	-0.617	0.381	1.899	68	< 0.0001
EVI 2	**-0.889**	**0.791**	**1.304**	**113**	**< 0.0001**	**-0.703**	**0.494**	**1.717**	**68**	**< 0.0001**
DVI	**-0.887**	**0.786**	**1.319**	**113**	**< 0.0001**	**-0.687**	**0.472**	**1.753**	**68**	**< 0.0001**
NDVI	-0.806	0.650	1.688	113	< 0.0001	-0.625	0.391	1.883	68	< 0.0001
NDVI MODIS	-0.680	0.463	2.091	113	< 0.0001	-0.704	0.496	1.713	68	< 0.0001
RDVI	**-0.884**	**0.781**	**1.335**	**113**	**< 0.0001**	**-0.706**	**0.498**	**1.709**	**68**	**< 0.0001**
MCARI 1	**-0.882**	**0.778**	**1.344**	**113**	**< 0.0001**	**-0.685**	**0.469**	**1.759**	**68**	**< 0.0001**
MSR	-0.861	0.742	1.449	113	< 0.0001	-0.622	0.387	1.889	68	< 0.0001
OSAVI	-0.808	0.652	1.682	113	< 0.0001	-0.628	0.394	1.878	68	< 0.0001
WDRVI (0.1;750)	-0.845	0.714	1.526	113	< 0.0001	-0.625	0.391	1.883	68	< 0.0001
Chlorophyll indices										
SR red edge	**-0.872**	**0.760**	**1.399**	**113**	**< 0.0001**	**-0.774**	**0.600**	**1.526**	**68**	**< 0.0001**
SR green	-0.857	0.735	1.469	113	< 0.0001	**-0.654**	**0.427**	**1.826**	**68**	**< 0.0001**
NDVI red edge	-0.854	0.730	1.482	113	< 0.0001	-0.604	0.365	1.922	68	< 0.0001
CL red egde	**-0.868**	**0.754**	**1.415**	**113**	**< 0.0001**	-0.570	0.325	1.982	68	< 0.0001
NDVI green	-0.835	0.697	1.571	113	< 0.0001	**-0.675**	**0.455**	**1.780**	**68**	**< 0.0001**
CL green	-0.857	0.735	1.469	113	< 0.0001	**-0.654**	**0.427**	**1.826**	**68**	**< 0.0001**
MCARI 2	**-0.897**	**0.804**	**1.262**	**113**	**< 0.0001**	-0.574	0.330	1.975	68	< 0.0001
TCARI	0.694	0.482	2.053	113	< 0.0001	0.311	0.097	2.293	68	0.0099
MTCI	-0.849	0.721	1.507	113	< 0.0001	-0.532	0.283	2.042	68	< 0.0001
DR	-0.833	0.693	1.580	113	< 0.0001	-0.576	0.331	1.973	68	< 0.0001
Carotenoid indices										
CRI 550	-0.599	0.359	2.284	113	< 0.0001	-0.224	0.050	2.351	68	0.0660
PRI	-0.401	0.161	1.990	94	< 0.0001	-0.570	0.325	1.935	68	< 0.0001
SIPI 2	0.546	0.298	2.390	113	< 0.0001	-0.396	0.157	2.215	68	0.0004
PSRI	0.715	0.512	1.993	113	< 0.0001	0.400	0.160	2.211	68	0.0007
Water Content										
WBI	0.523	0.274	2.431	113	< 0.0001	-0.189	0.036	2.369	68	0.1220

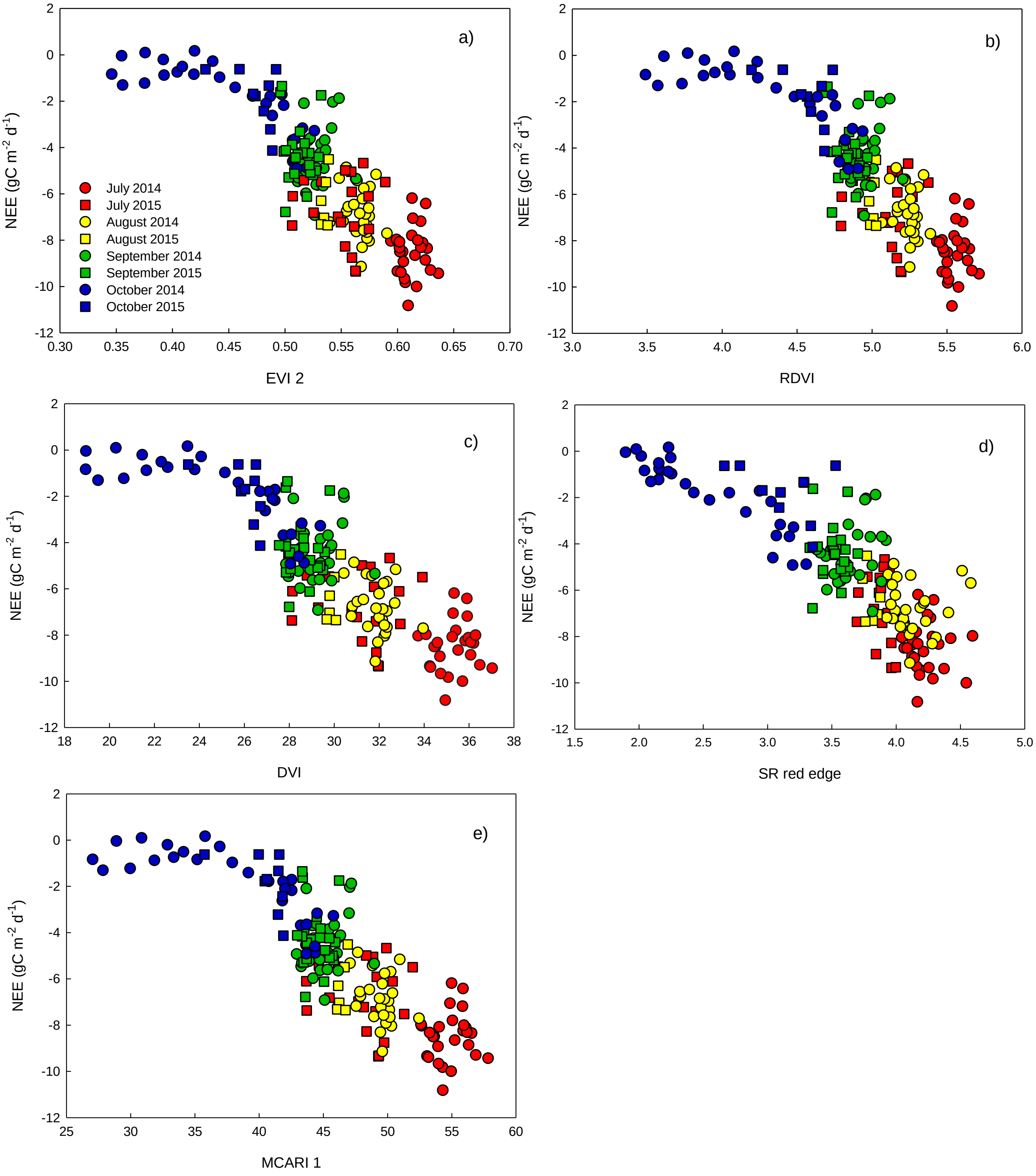

Figure 3.10. Relationships between daily NEE estimates and midday averages (11-13 a.m.) of the five vegetation indices selected as best predictor of NEE for Collelongo forest (EVI 2- plot a, RDVI- plot b, DVI- plot c, SR red edge- plot d, MCARI 1- plot e). July (red), August (yellow), September (green), October (blue) were considered in the plots. Circles and squares refer to 2014 and 2015, respectively.

From the analyses presented, almost all the indices that better predict CO_2 fluxes are associated with the canopy structure (EVI 2, RDVI, DVI, MCARI 1; Figure 3.10). These indices are generally used for the global monitoring of vegetation canopies and represent a number of alternatives to the conventional NDVI in order to overtake its limitation such as the saturation issue for dense canopies [160,217,218]. A common feature of the best structural indices is the use of only two spectral bands, the red and the NIR, in their formulation. These bands exploit the reflected energy in the red chlorophyll absorption region and the reflected energy in the NIR due to light scattering in the leaves mesophyll. Anyway, it is recognized that VIs calculated as difference or normalized difference between red and NIR suffer the saturation of red reflectance and much higher NIR reflectance compared to red reflectance at intermediate-high Chl content [123], thus showing low performance for high canopies. For these reason, Wu et al. [219], according to the sensitivity analysis of Gitelson and Merzlyak [220], suggested to replace the traditional red and NIR spectral bands (680 nm and 860 nm, respectively) by spectral bands in the red-edge region (690-750 nm) to compute indices having better linearity with Chl content and thus more suitable to follow vegetation dynamics throughout the season. The red edge region is defined as the part of the spectra where the leaf reflectance changes from very low Chl red absorption band near 680 nm to very in the high in the near-infrared near 750 nm [221]. In this context, it is worth to note that all the VIs presented in Table 3.2 were computed in two versions: a) choosing R750 or b) R860 as the NIR band in the formula. It resulted that indices calculated using R750 as NIR band showed higher R^2 consistently for both years compared to the same results using R860 (data not shown). Our results confirm that, computing the structural indices with a red edge band improve the performances of conventional structural indices based on red and NIR bands that usually do not provide high performance in tracking ecosystem dynamics.

Figure 3.10 showed very clearly how different phases of the season were distinguished by the selected VIs in both years of study. In the relationship between CO_2 fluxes and VIs, all the selected months are well separated (different colors, Figure 3.10) and keep the same position during the two years, with the exception of July 2015. In fact, a common feature of all the plots presented in Figure 3.10 is that data points of July 2015 (red squares) overlay data points of August 2014 and 2015 (yellow circles and squares). This characteristic supported the difference between July 2014 and July 2015, which was formerly evidenced by the meteorological dataset (Figure 3.1, 3.2 and 3.3) and eddy covariance dataset (Figure 3.4), thus proving the ability of vegetation indices in detecting seasonal variations in CO_2 fluxes. A *t* test ($p < 0.01$) confirmed that the means of NEE in July 2014 (-8.5 ± 0.20 n=27) and July 2015 (-6.3 ± 0.37 n=22) were statistically different; the same result was observed for the selected five indices (EVI 2, RDVI, DVI, SR red edge and MCARI1) for the same period. Although less evident, it is possible to distinguish that data points related to October 2014 (blue circles) and September 2015 (green squares) showed comparable values (Figure 3.10). The partial overlapping of these data were explained in the earlier senescence in 2015, and also confirmed the fact that the forest showed a lover sink capacity by the end of the growing season 2015 (end of September-October) as compared to the same period in 2014 (Figure 3.4). On the other hand, we were not able to test the earlier start of the vegetative season of 2015 as compared to 2014 through VIs as Cropscan sensor was not operating on early spring 2014. Among the selected indices, the SR red edge was the only one included in the "chlorophyll indices" category. SR red edge is known to provide good results in estimation of Chl content in closed forest canopy [188]. The main reason of the high performance are due to the employment of two red edge region (R710 and R750), which capitalize on sensitivity to changes in canopy Chl content and senescence. As clearly explained by Gitelson et al. [221], while reflectance at 680 nm is sensitive to low Chl content and saturation level is reached for 100 mg m^{-2}, the range 700–710 nm does not reach saturation level even for very high Chl content (above 670 mg m^{-2}), and the sensitivity to Chl remained high across a wide range of leaves. At 750 nm, the reflectance virtually did not depend on Chl concentration and is fairly inert, thus being a perfect candidate for reference parameter in spectral index computation.

While the afore mentioned studies focused mostly on models fed by vegetation indices to estimate C fluxes, the distinctive trait of our work was the simultaneous collection of C flux determinations with structural, ecophysiological and pigment measurements which allowed to establish a more consistent and wider description of forest dynamics.

After focusing on a canopy level, we investigated how the spectral indices that performed best for NEE tracking, are related to total chlorophyll (Chl tot) foliar concentrations, ecophysiological variables and leaf nitrogen content (N) (Table 3.5).

Table 3.5. Selected optical indices related to leaf biochemical (chlorophyll, Chl), physiological (ETR, Electron Transport Rate) variables and leaf nitrogen content. Coefficient of determination (R^2) and number of observations (*n*) are presented considering 2014 and 2015 together. The asterisk indicates significance of correlation: ****$p < 0.0001$; ***$p < 0.001$; **$p < 0.01$; *$p < 0.05$.

Index		Chl tot (µg cm^{-2})	ETR (µmol m^{-2} s^{-1})	N (%)
		n=10	*n*=10	*n*=11
Name	**Reference**	**R^2**	**R^2**	**R^2**
EVI 2	Jiang et al. [162]	0.420 *	0.714**	0.553**
RDVI	Haboudane et al.[164]	0.436 *	0.700**	0.577**
DVI	Tucker et al.[185]	0.389 (0.0542)	0.724**	0.541**
SR red edge	Zarco-Tejada et al.[188]	0.493 *	0.609**	0.848****
MCARI 1	Haboudane et al. [164]	0.407 *	0.731**	0.519**

The regression analysis showed a fair agreement between selected indices and total Chl, with R^2 ranging from 0.407 for MCARI1 and 0.493 for SR red edge. Apart from DVI, which relationship with R^2 resulted non-significant, none of the 5 indices provided a higher significance than the others; in fact, all the correlations reported the same level of significance ($p < 0.05$). The low R^2 values were linked to the fact that EVI 2, RDVI, DVI and MCARI 1 are *structural* indices and they were not particularly conceived for pigment estimation. These traditional indices mainly tracked canopy structural changes but are not able to identify subtle changes due to pigment content variation between study sites [188]. This could partially explain the relatively lower R^2 values found for the relationships between these 5 selected indices and the Chl tot. However, neither the red edge spectral indices usually employed to estimate changes in Chl content showed better performances (see VIs vs Chl tot in Table 3.6a) conversely to what reported in literature [188,222–224]. It might be two possible reasons for this discrepancy: 1) limited number of data which lead to weak relationships (n=10; Table 3.6a) and 2) difference between Chl sampling (leaf level) and optical sampling (canopy level). In fact, low correlation between *chlorophyll* spectral indices and Chl content suggests that sampled leaf disks were not fully representative of the whole canopy condition during the sampling days.

On the other hand, we found high correlations between ETR and the 5 selected indices. Particularly, when related to ETR, EVI 2, RDVI, DVI and MCARI 1 showed the highest R^2 of all the VIs computed in this study (Table 3.5). This result is in accordance with the strong relationships found between the daily NEE and the same spectral indices (Table 3.4, Figure 3.10). Hence, eddy covariance and ecophysiological measurements confirmed that the selected indices were the ones that better captured the sink capacity of our forest both at canopy (NEE) and leaf level (ETR). In addition, ETR determined by chlorophyll fluorescence showed also significant positive relationships with NEE (R^2=0.79; $p < 0.001$).

While SR red edge had the lower R^2 value when related to ETR, we observed the highest R^2 when it was related to nitrogen (Table 3.5). It is worth to note that when we related the vegetation indices to N component, the ones which gave best results were the *chlorophyll* indices. In fact, beyond SR red edge, NDVI red edge (R^2=0.781***), DR (R^2=0.765***), CL red edge (R^2=0.724***), NDVI green (R^2=0.695**), MTCI (R^2=0.675**) and MCARI 2 (R^2=0.664**) performed the best linear correlations with nitrogen. Our findings are in agreement with other studies focused on the link between red edge indices and nitrogen [95,225–227]. Consistently, Schlemmer et al. [227] informed that non-destructive N content estimation employed either green or red-edge spectral regions while avoid spectral bands located near the main red absorption band of Chl (where absorption saturates at low- to-moderate Chl values). As explained by Perez-Priego et al. [228], plant enable photosynthetic processes by absorbing light through chlorophyll pigments. Since N atoms are basic components of the chlorophylls molecular structure, there is a correlation between leaf chlorophyll pigments and leaf N content. This correlation explains why canopy nitrogen content can be estimated through chlorophyll-related vegetation indices. In our study, we found relatively low coefficients of determination for the relationships between the *chlorophyll* indices and Chl tot while we found higher coefficients of determination for the relationships between the *chlorophyll* index and N status, as expected from the literature. This disagreement confirms our hypothesis that sampled leaf disks were not fully representative of the canopy condition. In fact, while we used few (n = 4-8) leaf disks for Chl estimation, N was estimated by averaging all the leaves from several branches (n>15) around the flux tower, thus ensuring higher representativeness of the canopy condition around the tower.

For each growing season (from July to October) maximum five field measurement campaigns were carried out for the sampling of leaf disks used in pigment extraction (see 3.3.2.4 section). For technical and economic reasons, these biochemical determinations cannot be as frequent as those made for the detection of the optical indices. So, due to this relatively lower number of biochemical determinations, the pigment measurements from the 2014 and 2015 years of study were considered together, leading to a total observation number of 10. Tables 3.6 illustrates only the highest R^2 and significant ($p \leq$

0.05) linear regressions between the leaf pigment concentrations and the vegetation indices related to Chl and Car analyzed during the 2014 and 2015 growing seasons.

As already mentioned, apart from SR green and CL green, we found not very high but significant relationship between *chlorophyll* indices and Chl tot while no significant relationship were found between *cholophyll* indices and Car; consequently the significant relationships with Car/Chl tot ratio were driven by Chl tot (Table 3.6a). Conversely, apart for SIPI 2, we found high R^2 for *carotenoid* indices related to both Chl tot, Car tot and therefore, the ratio Car/Chl tot (table 3.6b). In particular, remarkably high correlations were found for VAZ related to both PRI ($R^2 = 0.80$) and PSRI ($R^2 = 0.76$). As VAZ pool is associated with the photoprotection mechanisms and VAZ pool size increase with increasing irradiance and environmental stress [229], we further investigate PRI and PSRI in the following section.

Table 3.6a. Linear regressions between main leaf pigment measurements and chlorophyll vegetation indices computed for this study. The coefficient of determination (R^2), number of observations (*n*) and probability value (*p* value) are presented for 2014 and 2015 growing season together.

Index	Chl tot ($\mu g\ cm^{-2}$) $n = 10$		Car/Chl tot $n = 10$		VAZ ($\mu g\ cm^{-2}$) $n = 10$		Carotenoids ($\mu g\ cm^{-2}$) $n = 10$	
Chlorophyll indices	R^2	p	R^2	p	R^2	p	R^2	p
SR red edge	0.493	0.0236*	0.561	0.0127*	0.661	0.0043**	_	_
SR green	–	–	0.432	0.039*	0.538	0.0158*	_	_
NDVI red edge	0.487	0.0249*	0.553	0.0137*	0.606	0.0080**	_	_
CL red egde	0.485	0.0252*	0.570	0.0116*	0.614	0.0074**	_	_
NDVI green	0.418	0.0434*	0.457	0.0319*	0.579	0.0105*	_	_
CL green	–	–	0.432	0.0390*	0.538	0.0158*	_	_
MCARI 2	0.437	0.0375*	0.569	0.0117*	0.534	0.0164*	_	_
MTCI	0.483	0.0256*	0.568	0.0118*	0.607	0.0079**	_	_
DR	0.459	0.0313*	0.524	0.0179*	0.556	0.0132*	_	_

Table 3.6b. Linear regressions between main leaf pigment measurements and carotenoid and water content vegetation indices computed for this study. The coefficient of determination (R^2), number of observations (*n*) and probability value *p* value) are presented for 2014 and 2015 growing season together. R^2 and *P* values for significant relations are not shown (–); *, $p \leq 0.05$; **, $p \leq 0.01$; ***, $p \leq 0.001$.

Index	Chl tot ($\mu g\ cm^{-2}$) *n* = 10		Car/Chl tot *n* = 10		VAZ ($\mu g\ cm^{-2}$) *n* = 10		Carotenoids ($\mu g\ cm^{-2}$) *n* = 10	
Carotenoid indices	R^2	*P*	R^2	*p*	R^2	*p*	R^2	*p*
PRI	0.726	0.0036**	0.481	0.0383*	0.800	0.0011**	0.504	0.0322*
SIPI 2	0.467	0.0293*	_	_	0.411	0.0459*	_	_
PSRI	0.588	0.0097**	0.485	0.0252*	0.763	0.001***	0.445	0.0352*

3.3.3. Carotenoid spectral indices as indicators of stress and senescence

As suggested by Gamon [71], exploration of pigments with a particular focus on the rich world of carotenoid biochemistry and function should be expanded given that understanding of the role of carotenoids as optical indicators of stress responses is in its infancy, but is ripe for further exploration. Among the spectral indices performed with pigment estimation, we focus our analysis on PRI and PSRI, which are grouped as *carotenoid* indices (Tables 3.2), to explore to which extent these indices could be proxies of stress or senescence events in a forest ecosystem. Recent studies [230,231] clarified the dual nature of PRI that, along with NDVI, is one of the most famous indices in vegetation remote sensing. Briefly, PRI responses can be divided into “facultative” response (xanthophyll cycle-driven effects operating over the diurnal time scale) and “constitutive” response (changing pigment pool sizes over seasonal time scales, e.g. due to ontogeny and senescence). In our two years-study, we focused on the seasonal time scale when PRI is driven mainly by pigment transformations associated with ontogeny and not by the xanthophyll cycle per se [232]. PRI monthly averages in 2014 resulted lower than 2015 for July ($p < 0.01$), September ($p < 0.001$) and October ($p < 0.05$) while there was not significant difference between August averages (Figure 3.11). This result indicated that PRI was an indicator of seasonally shifting pigment (chlorophyll, carotenoid and anthocyanin) contents, and hence photosynthetic activity thus supporting the lower sink capacity of the forest in 2015 (Figure 3.4). We analyzed Chl-PRI and Car-PRI relationship to understand the effects of these pigments on PRI and we found that PRI-Chl relationship were closer than PRI-Car ($R^2 = 0.726$; $p < 0.01$ for Chl and $R^2 = 0.504$; $p < 0.05$ for Car, Table 3.6b). PRI uses reflectance at 531 nm in the so-called green edge and at 570 nm in the green range of the spectrum. Similar to the red edge, the green edge (between 490 and 530 nm) is a transition region which is governed by Chl a, Chl b, Car and Anthocyanins (AnC) absorption [35]. On the other hand, the reflectance at 570 nm was invariant with respect to Car content due to very small Car absorption [35]. Therefore, the theory beyond the PRI formulation justified the significant correlation found for both Chl and Car.

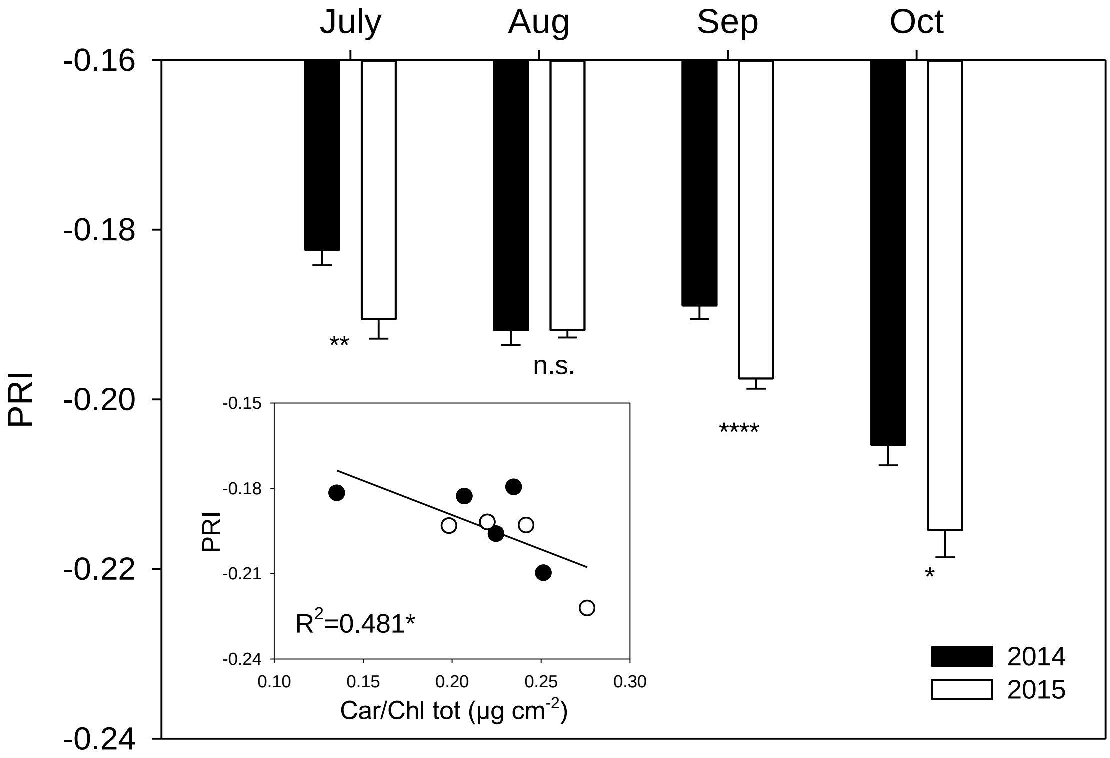

Figure 3.11. Seasonal trend of PRI for 2014 (black bars) and 2015 (white bars). Insert: correlation between PRI and Car/Chl tot ratio (µg cm^{-2}). In the principal image measurements image are monthly averages of PRI while in the insert, measurements of PRI coincide to the exact day of pigment sampling. For each month, asterisks represent significantly different data (*t*-test; ****$p < 0.0001$; ***$p < 0.001$; **$p < 0.01$; *$p < 0.05$, n.s. = not significant)

The differences in fluorescence parameters and in Car/Chl tot ratio between July 2014 and July 2015 was also reflected in a significant different PRI index between the two years (compare Figure 3.8.b, 3.9 and 3.11), indicating as this index is able to detect changes in leaf pigment composition and energy dissipation mechanism associated with dry and hot periods. In August, ETR and PRI were not statistically different between the two years, while in September we observed a decrease of ETR and NPQ (Figure 3.9) associated with a reduced NEE (Figure 3.4) and a decreased irradiance level during the late summer-early autumn at the onset of the senescence period. Indeed, between September and October we recorded a general decrease in chlorophyll and carotenoid pigments associated with a decrease of the PRI index, especially during 2015 when the senescence period resulted slightly anticipated with respect to 2014.

As described by Solovchenko [233], stresses that limit photosynthesis often increase Car/Chl tot ratio. According to this, we analyzed also the relationship Car/Chl tot-PRI ($R^2 = 0.481$; $p<0.05$, Table 3.6b) to evaluate if this index was able to detect changing pigment levels (Figure 3.11, insert). Consequently, seasonal an inter-annual variation of PRI was dependent on changes in Chl, Car and Car/Chl ratio, as suggested by the significant relationship found between these parameters (Figure 3.11, insert).

Plant Senescence Reflectance Index (PSRI) was first proposed by Merzlyak et al.[196] as being sensitive to the senescence phase of plant development. It is a combination between red, NIR and green band, the last (510 nm) sensible to carotenoids. In our study, seasonal trends of PSRI increased from July to September 2014, according with the ontogenic stages of the canopy. On the contrary, PSRI values resulted constant in July, August and September 2015 while sharply increased during October of the same year (Figure 3.12).

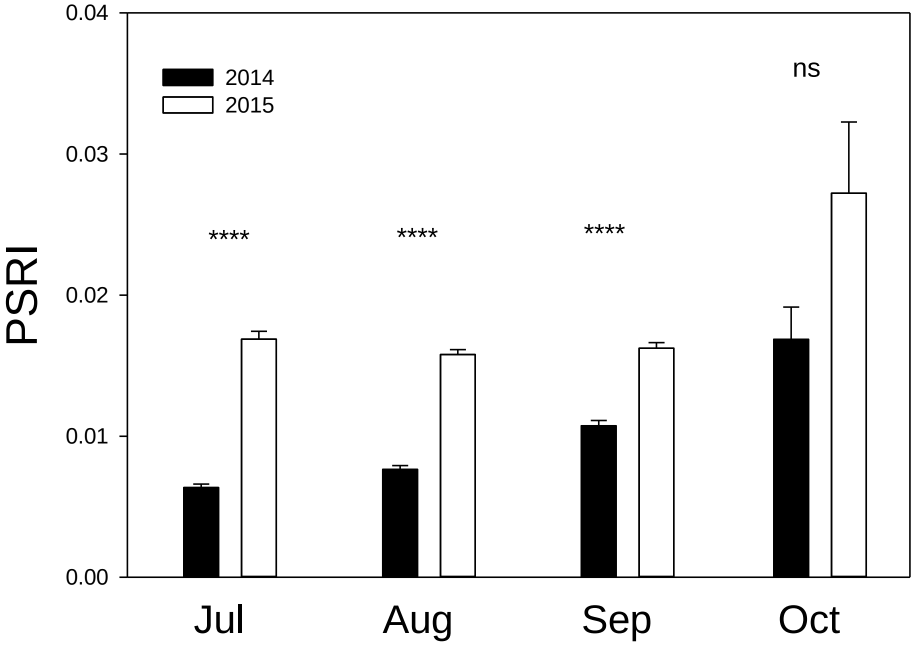

Figure 3.12. Seasonal trend of PSRI for 2014 (black bars) and 2015 (white bars). Measurements image are monthly averages of PRSI. For each month, asterisks represent significantly different data (*t*-test; ****$p < 0.0001$; ***$p < 0.001$; **$p < 0.01$; *$p < 0.05$, n.s. = not significant).

We found that, except for October, the PSRI values (monthly averages) were significantly different between the two years reflecting the different distribution of carotenoids (especially neoxanthin and β-carotene) during the full vegetation stage (July-September) of summer period (Figure 3.7). PSRI was significantly related to Car/Chl tot with a very similar coefficient of correlation found for PRI-Car/Chl tot (R^2=0.485; p<0.05, Table 3.6b). Indeed, the Car/Chl tot ratio takes into account the relative variations of the two main groups of photosynthetic pigments, both of them with different structural and biochemical functions driving the efficiency of photosynthesis during the plant vegetation cycle. As suggested by other studies [234], we hypnotize that confounding effects as structural parameters (i.e., canopy structure) highly affected both PRI and PSRI thus worsening their performances at canopy level (e.g., R^2< 0.50).

Conclusions

Our study focused on exploring the conditions of a Mediterranean beech forest over two years with different meteorological conditions from canopy to leaf level taking advantaging of different methods. We investigated seasonal patterns of carbon fluxes, photosynthetic pigments and chlorophyll fluorescence which consistently evidenced a drought period and an anticipated senescence in July and October 2015 than in the same months of 2014, respectively. The main outcomes of our study were the following:

- Four optical indices related to structure (EVI 2, RDVI, DVI and MCARI 1) and one *chlorophyll* index (SR red edge) were found to better track NEE variation for both 2014 and 2015, thus suggesting that structural parameters (leaf area, leaf status) are one of the main drivers of the C uptake capacity in the considered deciduous forest; this result was also confirmed at leaf level since the same indices were the ones that better related to ETR measurements;
- *Chlorophyll* indices using green or red-edge in their formulation gave best performances for estimating N content but not for Chl probably due to the different sampling size (average of several leaves for N vs average of few leaf disks for pigment estimation);
- PRI and PSRI were the only indices that correlated with both Chl tot and Car; these indices were indicators of the shifting pigment composition related to stress (July) and senescence (October) during 2015.

In conclusion, our study support the hypothesis that a combination of different methodological approach (optical indices, eddy covariance, chlorophyll fluorescence and leaf pigment analysis) can give detailed information on the main processes affecting carbon sink capacity and on its seasonal and inter-annual changes in both health and stressed vegetation.

4. Validation of three fAPAR products in a deciduous beech forest site in Italy

4.1. Introduction

Ecosystems are continuously changing due to both natural and anthropic factors. Monitoring biophysical variables is fundamental to describe vegetation dynamics, disturbances, and responses to changing environmental conditions [121]. The Fraction of Absorbed Photosynthetically Active Radiation (fAPAR) is recognized as an Essential Climate Variable (ECV) by the Global Climate Observing System (GCOS) as it has a primary role in estimation of carbon balance [235]. fAPAR is generally defined as the fraction of Photosynthetically Active Radiation (PAR) absorbed by vegetation, where PAR is the solar radiation reaching the vegetation in the wavelength region 400-700 nm [236]. Consequently, fAPAR is the available light energy for plant productivity and thus is strictly related to photosynthesis. It is influenced by illumination condition and varies with sun position, atmospheric conditions, and the relative contributions of the direct and diffuse illumination [237]. The actual or ‘blue-sky’ fAPAR is the sum of two terms, weighted by the diffuse fraction in the PAR domain: the ’black-sky’ fAPAR related to the direct component of the incident radiation and the ‘white-sky’ fAPAR related to the diffuse component of the incident radiation [238].

The importance of this variable in the vegetation monitoring is related to 1) the fact of being linked both to ecosystem function and structure [239] and in 2) the possibility to be monitored from space. The growing availability of fAPAR satellite products at global level make this variable suitable for monitoring vegetation status [240], phenology [241], drought events [242] and land degradation [243]. The productivity of a vegetated surface is related to fAPAR and remotely sensed fAPAR data are widely used as input in carbon productivity models [129,244,245]. One of the most widely used models in the estimation of carbon productivity is the Light Use Efficiency (LUE) model that describes carbon sequestration as a product of a structural term determining light absorption (fAPAR x PAR) and a physiological efficiency term (ε) defining the conversion of solar radiation into biomass or carbon. In this approach, the accuracy fAPAR data used is relevant, as it has a considerable impact on the fluxes estimated by the model [1], even more in those cases when ε is assumed to be constant.

The methods used to monitor fAPAR could be divided into ground and satellite methods. Weiss et al. [237] report that there are mainly 4 different ground methods, depending on the approximation: a) assessing fAPAR directly using quantum sensors that measure all the terms of the radiation balance [146]; b) assessing transmitted PAR using ceptometers that compute the instantaneous fIPAR (fraction of Intercepted PAR) [104]; c) assessing directional transmittance measurements using digital hemispherical photography (DHP) [238] or LAI-2000 [246] and d) simulating fAPAR through a 3D model that accurately takes into account the canopy structure [247]. On the other hand, the major approaches used to estimate fAPAR from remote sensing over a large spatial scale are basically two: a) empirical models based on relationships between field measurements and satellite-derived vegetation indices as Normalized Difference Vegetation Index (NDVI) [99,106] or EVI [93,248] and b) physically-based methods by inversion of radiative transfer models (RTM) [249,250]. In the last decades, several satellite-based fAPAR products have been developed from different sensors on a global scale by spatial agencies and earth observation services, which make available to the scientific community various fAPAR products at different temporal and spatial resolutions over the Earth [251–257]. In particular, the Copernicus Global Land Service (http://land.copernicus.eu/global/) delivers global LAI, fAPAR, and fCOVER products from SPOT VEGETATION (1999-2014) and PROBA-V observations (2014-present) with a spatial sampling close to 1 km and temporal frequency of 10-days. These products, namely GEOV1 products, were developed to capitalize on existing products and its validation results [22], and were globally validated and intercompared with existing satellite data and ground reference maps, showing better performances than others satellite products [258]. Since 2000, NASA has delivered MODIS/TERRA fAPAR Collection 5 (C5) products that are produced at 1 km spatial resolution [249,259]. Accuracy improvements from 0.2 to 0.1 of Collection 5 over previous Collection 4 were observed in several studies [260–262]. Lastly, the newest version of fAPAR MODIS product is Collection 6 (C6) which is 500 m spatial resolution and contains the entire time series from February 2000 to the present [263]. Recent studies [263,264] aimed to assess product accuracy, uncertainty, and consistency with the previous version. Yan et al. [264] informed about the absence of valid ground truth for fAPAR measurements over deciduous broadleaf forest and recommended more efforts in field measurements to further refine remote sensing data performance in the future. Also Camacho et al. [258] pointed out how validation of satellite products are limited by the ground data set available and that, presently, a very small number of data exist over broadleaf evergreen and deciduous forests. Recently, studies aimed to evaluate consistency between fAPAR datasets in forest biomes proved that important differences exist among them and thus further efforts to improve accuracy in carbon models are needed [260,265–267]. Subsequently, the availability of new satellite products require simultaneous efforts in their validation to provide users with a better comprehension of product performances and uncertainties [268]. To reach this goal, ground reference fAPAR datasets are essential, however few sites are equipped to generate measurements of fAPAR useful for the validation of space-borne products [236]. Nevertheless, validation is not simply equivalent to field measurements. An up-scaling strategy to extend the in situ measurements and match satellite data resolution is needed for taking into account the spatial variability of the site at the size of satellite footprints [269]. One of the constraints that limit ground fAPAR measurements in forest ecosystems is the retrieval of downwelling PAR at the top canopy, that results unfeasible when flux towers are not accessible in the study site [266]. Also, collecting ground datasets is resource intensive and mostly limited in spatial and temporal sampling extensions [265]. In this frame, if efforts in validation of satellite data with accurate field data are generally necessary, those carried out in forest ecosystems are even more valuable and indispensable.

This chapter presents a validation exercise that was carried out at the Collelongo site, a deciduous broadleaf forest in Italy, which has been already described in Chapter 3. The aim of this study is to validate three currently available fAPAR satellite products: GEOV1, MODIS C5 and the recent MODISC6 version against ground references collected using three different devices (i.e., Apogee sensors, PASTIS sensors and digital camera with fish-eye lens) and to determine to what extent the GCOS requirements on accuracy (maximum 10% or 0.05) [270] are met. Both ground sampling and satellite product validation were conducted following best practices developed within the Land Product Validation sub-group (LPV) of the Committee on Earth Observing Satellite (CEOS) on Calibration and Validation Working Group (WGCV) [269].

4.2. Remote sensing product

In this section, the principal characteristics of the three different satellite products examined in this work are presented. Table 4.1 summarizes the main features of each fAPAR product.

Table 4.1. Characteristics of the fAPAR remote sensing products under study. GSD, ANN, RTM and CYC stands for “Ground Sampling distance”, “Artificial Neural Network", “Radiative Transfer Model”, and "CYCLOPES 3.1" respectively.

Product	**Sensor**	**GSD**	**Frequency**	**Compositing**	**Algorithm**	**Definition**	**Parametrization**	**Reference**
GEOV1	PROBA-V	1 km	10-days	30-days	ANN trained with CYC and MODIS C5	Green vegetation, instantaneous black-sky ~10:15 a.m.	Global	Baret et al., [257]
MODIS C5 (MOD15A2)	MODIS/ TERRA	1 km	8-days	8-days	Inversion RTM 3D	Green vegetation, instantaneous black-sky 10:30 a.m.	8 biomes	Knyazikhin et al., [251]
MODIS C6 (MOD15A2H)	MODIS/ TERRA	500 m	8-days	8-days	Inversion RTM 3D	Green vegetation, instantaneous black-sky 10:30 a.m.	8 biomes	Yan et al., [263]

4.2.1. GEOV1

The GEOV1 LAI, fAPAR and fCOVER products are delivered with a 10-day temporal sampling in a *Plate Carrée* projection from December, 1998 to present. GEOV1 products were produced based on SPOT VEGETATION (SPOT VGT) observations until the end of the mission in May 2014, and covered more than 15 years of data. To provide continuity to the service at 1 km, the GEOV1 processing chain was adapted to the Project for On-Board Autonomy-Vegetation (PROBA-V) mission [271], launched in May 2013 by ESA. One of the main objectives of PROBA-V was to ensure the succession of the VEGETATION instruments acting as "gap filler" between SPOT and Sentinel-3. Thus, since May 2014, the GEOV1 products are based on PROBA-V observations, with spectral characteristics nearly identical to VEGETATION. The GEOV1 retrieval methodology relies on neural networks trained to generate the "best estimates" of LAI, fAPAR, and fCOVER obtained by fusing and scaling of MODIS C5 [251] and CYCLOPES 3.1 [255,272] satellite products to take advantage of their specific performances while limiting the situations where they show deficiencies [257]. The algorithm provides instantaneous black-sky fAPAR value at around 10:15 a.m. solar time under clear sky conditions, which is a close approximation of the daily integrated black-sky fAPAR value. Note that conversely to MODIS and similarly to CYCLOPES, no biome classification is required to run the GEOV1 algorithm, although GEOV1 products are impacted by the 8-types biome dependence of MODIS C5 algorithm. GEOV1 products from both SPOT VGT and PROBA-V sensors are freely distributed through the Global Land Service of the European Commission's Copernicus program (http://land.copernicus.eu/global).

4.2.2. MODIS C5

Terra MODIS LAI and fAPAR (MOD15A2) collection 5, available since 2000 from https://lpdaac.usgs.gov/products/, is produced based on TERRA observations at 1 km spatial resolution and 8 days step over a sinusoidal grid. The main algorithm is based on Look Up Tables (LUTs) simulated from a three-dimensional RTM [251]. The MODIS red and NIR atmospherically corrected reflectances [273] and the corresponding illumination-view geometry are used as input for the LUTs. The output is the mean LAI and fAPAR computed over the set of acceptable LUT elements for which simulated and measured MODIS surface reflectances are within specified uncertainties. When the main algorithm fails, a backup solution based on LAI and fAPAR-NDVI relationships is used. In collection 5, parameters of both main and backup algorithms are defined for 8 vegetation types, and a new stochastic RTM was used to better represent canopy structure and the spatial heterogeneity intrinsic to woody biomes.

The main drawbacks observed in MODIS fAPAR C5 are its low temporal stability and the systematic overestimation of fAPAR retrievals over sparsely vegetated areas [258]. Camacho et al. [258] reported an overall accuracy (RMSE) of 0.11 using the same ground reference data set than for evaluating SPOT VGT GEOV1 products [258].

4.2.3. MODIS C6

The MODIS LAI and fAPAR (MOD15A2H) collection 6 (doi: 10.5067/MODIS/MOD15A2H.006), is provided at frequency of 8 days and 500 m spatial resolution in which the algorithm chooses the best pixel available from all the acquisitions of the Terra sensor within the 8-day period. MODIS LAI and fAPAR C6 uses the same retrieval algorithm and LUTs as C5 [263], but C6 benefited from improved surface reflectances and biome type inputs at their 500 m version. The consistency between C5 and C6 was evaluated [263] without finding spatial scale effects due to resolution changes, with the RMSE between both versions of 0.091 fAPAR units with the same biome input. The accuracy assessment performed over 45 fAPAR ground measurements showed an overestimation of both C5 and C6 fAPAR products over sparsely-vegetated areas [264].

4.3. Materials and Methods

4.3.1. Study site

The experiment was carried out at the Collelongo-Selva Piana pure beech forest (Abruzzo region, Central Italy, 41°50′58″N, 13°35′17″E, 1560 m elevation), which was already described in Chapter 3 (Section 3.2.1).

4.3.2. Temporal and spatial sampling

The study area used for satellite validation covered 5 km x 5 km and is centered at the flux tower (41°50′58″N, 13°35′17″E). Different temporal and spatial samplings were performed depending on the three different devices used in the experiment, two PAR sensors (Apogee and PASTIS, details in the following Section) and Digital cameras for collecting hemispherical photographs (DHP). The ground sampling was concentrated over a homogeneous area of approximately 1 km^2 around the flux tower, where 15 spatial units called Elementary Sampling Units (ESUs) were taken as reference (Figure 4.1). Each ESU is approximately 20 m x 20 m and was selected to cover the variability of the site around the flux tower area. The center of each ESU was geo-located using a Global Positioning System (GPS). ESU 1 (centered at the flux tower) was selected for an intensive PAR measurements sampling for its proximity to the reference above canopy sensors and thus equipped with Apogee-PAR sensors from July to December 2014 and from May to December 2015 (Table 4.2). ESUs 1-9 were equipped with PASTIS-PAR sensors from May to December 2015. All the 15 ESUs were involved in two field campaigns on July 8th and September 25th, 2015 for the spatial characterization of vegetation variables with DHPs (Figure 4.1).

Table 4.2. Specifications of ground data sampling in the study.

Name of the sensor	**Spatial sampling**	**Temporal sampling**	**Description**
Apogee-PAR	ESU 1 (tower)	July-December 2014 May-December 2015 (daily)	22 PAR sensors - Continuous measurements
PASTIS-PAR	ESUs 1-9	May-December 2015 (daily)	10 data logger with 6 PAR sensors each - Continuous measurements
Digital camera collecting Digital Hemispheric Photographs (DHPs)	ESUs 1-15	8 July 2015 25 September 2015	13 DHPs for each ESU

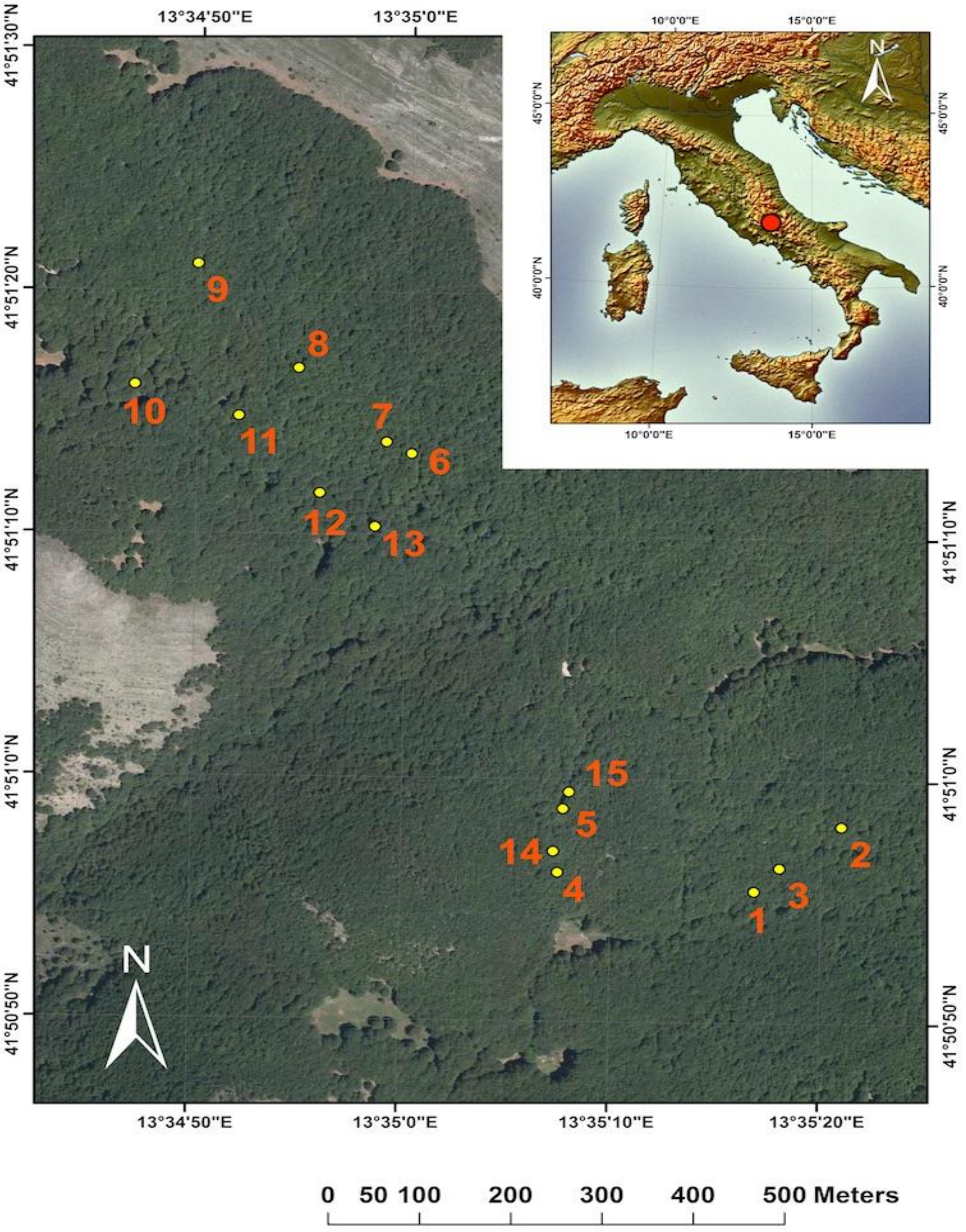

Figure 4.1. Spatial sampling design of the ground measurements over 1 km x 1 km area at Collelongo. ESU 1 was centered at the flux tower and equipped with Apogee sensors. ESUs 1-9 were equipped with PASTIS sensors. All the 15 ESUs were involved in the Digital Hemispheric Photographs campaigns. Further details can be found in the text. Image credits: Geocatalogo Regione Abruzzo (WMS service, orthophoto from 2013); inset image: NaturalEarthData (http://www.naturalearthdata.com).

4.3.3.Ground measurements and Instruments

4.3.3.1. PAR measurements from Apogee

Continuous PAR measurements of incident, transmitted and reflected PAR were collected according to the protocol for PAR measurements developed within the FP7 ÉCLAIRE Project (http://www.eclaire-fp7.eu/). In total, 22 PAR sensors (SQ-110, Apogee Instruments, Logan,USA) were installed around the flux tower (800 m^2) [274]. Specifically, 15 sensors pointing upward were mounted below the canopy to monitor transmitted PAR through the canopy ($PAR_b^{\downarrow}$) and 5 sensors pointing downward were mounted below the canopy to monitor reflected PAR by the soil ($PAR_b^{\uparrow}$). At the top of the tower, two sensors were installed on a horizontal 2 m arm to measure incident PAR above the canopy ($PAR_a^{\downarrow}$) and reflected PAR from the canopy ($PAR_a^{\uparrow}$), respectively. To maximize the radiometric footprint, below-canopy PAR sensors pointing downward were installed on a 2 m high pole while below-canopy PAR sensors pointing upward were installed on a 1 m high pole. PAR measurements were acquired every 10 seconds and stored as 30 minutes averages as μmol m^{-2} s^{-1}.

4.3.3.2. PAR Measurements from PASTIS

At ESUs 1-9, PASTIS device (PASTIS-PAR, INRA-Hyphen, Avignon, France) were installed to continuously measure transmitted PAR through the canopy ($PAR_b^{\downarrow}$). In addition, one PASTIS device was also installed above the flux tower at ESU 1 to measure incident PAR radiation above the canopy ($PAR_a^{\downarrow}$).

Each PASTIS system consists in a data logger associated to 6 wired hemispherical quantum sensors measuring instantaneous PAR signal in millivolts (http://www.hiphen-plant.com/products/pastis_18.html) [275]. Below the canopy, the data logger was fixed at a labeled tree while the sensors were installed at soil level. Each of the 6 sensors were mounted on a 30 cm-long support bar to avoid falling leaves and other litter material covering the quantum sensors while acquiring data.

PAR measurements were acquired every minute. PASTIS sensors measured downward radiation both above and below the canopy and an intercalibration against Apogee sensors was performed in order to combine Apogee and PASTIS measurements for fAPAR computation at the ESUs. Both PASTIS and Apogee PAR continuous ground measurements were used to qualitatively assess the temporal courses of the satellite products.

4.3.3.3. Gap fraction estimation from DHP

Two hemispherical digital photography (DHP) cameras were used for estimating fAPAR at the study area: CANON EOS 6D with a SIGMA 8mm F3.5 – EX DG and NIKON Coolpix 995-FCE8.

To perform an accurate images processing, the optical center and the projection function of the optical system were calculated for each camera [276]. At each ESU, 13 DHPs were taken pointing the camera upward-looking. A measurement was acquired every 10 m along the path (black circles, Figure 4.2) to cover the ESU area (20 m x 20 m), in agreement with the VALERI spatial sampling protocol (http://w3.avignon.inra.fr/valeri).

DHP acquisition was processed using CAN-EYE software version 6.4 developed at INRA-CSE Avignon (http://www6.paca.inra.fr/can-eye) for deriving biophysical variables (LAI, fAPAR, fCOVER) from hemispherical photos. Since CAN-EYE is based on a RGB colour classification of the image to discriminate vegetation elements from the background (i.e., gaps), photos were acquired with similar illumination conditions to limit the variation of colour dynamics between images. DHPs processing consisted of three steps: 1) image pre-processing aimed to remove undesired objects (e.g. operator, sun glint) and ensure better visual discrimination between vegetation and background adjusting image contrast, 2) assignment of the colours to each class (vegetation elements versus background) after reducing the number of distinctive colours in order to easily manipulate the image, 3) realization of a binary image (background versus vegetation elements), using the classification results [277].

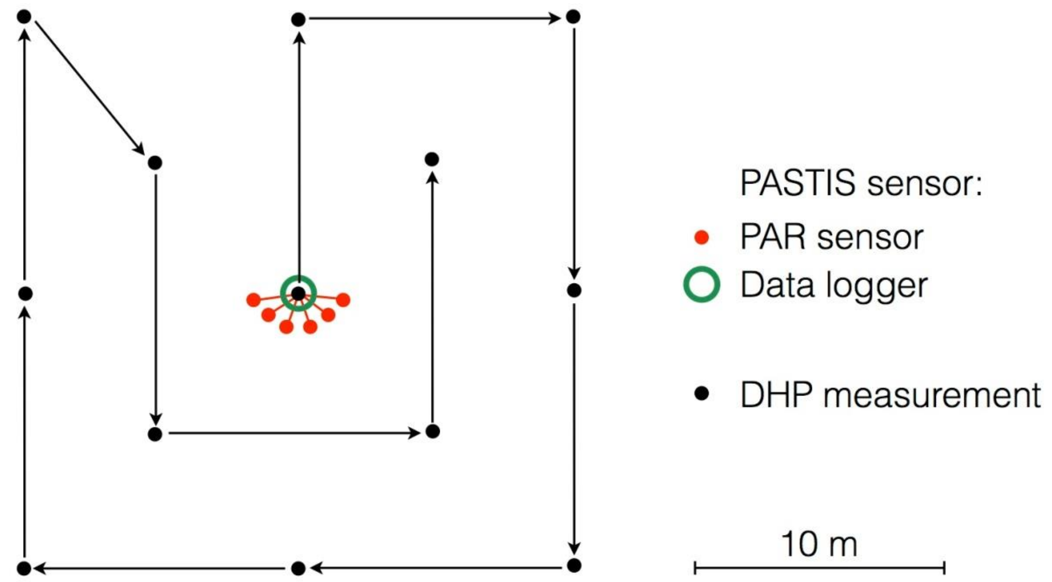

Figure 4.2. Spatial sampling for DHPs collection at each ESU. Every black circle stands for a DHP acquisition, while arrows indicate the path followed during the sampling at every ESU. PASTIS device consist in a data logger (green empty circle) and 6 PAR sensors (red circles). The first DHP acquisition is made at the PASTIS installation.

4.3.4. Calculation of ground fAPAR

4.3.4.1. Estimation of fAPAR from Apogee (fAPAR$_{\mathrm{APOGEE}}$)

In this work, the Apogee sensors, given the set-up, the spatial coverage, and the measurements of all fAPAR components (see Section 3.3.1), provided the reference fAPAR value at the tower site (ESU 1) against which PASTIS and DHP measurements were compared. Having the four PAR contributions, fAPAR from Apogee measurements (fAPAR$_{\mathrm{APOGEE}}$) was calculated as reported by Liang et al.[278]:

$$fAPAR = \frac{PAR_a^{\downarrow} - PAR_b^{\downarrow} - PAR_a^{\uparrow} + PAR_b^{\uparrow}}{PAR_a^{\downarrow}} \tag{4.1}$$

Where $PAR_a^{\downarrow}$ is the incident PAR above the canopy, $PAR_a^{\uparrow}$ is the reflected PAR above the canopy, $PAR_b^{\downarrow}$is the transmitted PAR through the canopy and $PAR_b^{\uparrow}$is the reflected PAR by the soil [278], all components are hemispherical quantities. As temporal mismatching between *in situ* data and satellite observation could be critical [279], we calculated fAPAR as averages from 10:00 a.m. to 11 a.m. to guarantee temporal matching between ground data and the satellites overpass. For the purpose of validating fAPAR products, only photosynthesizing materials (leaves, needles, or other green elements) should be accounted for in the calculation (green fAPAR)[267]. Nevertheless, in homogeneous deciduous forests where LAI reaches maximum values that remain stable during the vegetative season, the influence of non-photosynthetically active vegetation (NPV) elements (such as trunks, branches,) in the fraction of absorbed PAR by the canopy is expected to be quite small as compared to the green elements. For instance, Zhang et al. [280] showed that in the Harvard deciduous forest the contribution of NPV to the fAPAR is lower than 0.1 in spring and summer time, whereas the fAPAR from green elements reaches 0.85 in summer time. In line with this work, we assume that the largest impact of NPV elements in our ground dataset occured during the senescent period.

4.3.4.2. Estimation of fAPAR from PASTIS (fAPAR$_{\mathrm{PASTIS}}$)

fAPAR$_{\mathrm{PASTIS}}$ was computed using two sets of measurements in Equation (4.1): 1) incident and reflected PAR obtained from Apogee and transmitted PAR obtained from PASTIS (previously intercalibrated as reported in Section 3.3.2). The adapted equation was computed as follows:

$$fAPAR_{PASTIS} = \frac{PAR_{a\ APOGEE}^{\downarrow} - PAR_{b\ PASTIS}^{\downarrow} - PAR_{a\ APOGEE}^{\uparrow} + PAR_{b\ APOGEE}^{\uparrow}}{PAR_{a\ APOGEE}^{\downarrow}} \tag{4.2}$$

We used the same method to calculate $fAPAR_{PASTIS}$ at each of the 9 ESUs equipped with PASTIS sensors. It is worth to note that incident $PAR_{aPASTIS}^{\downarrow}$ was not used in the Equation (4.2) since a long data gap occurred due to battery loss. $fAPAR_{PASTIS-ESU\ n}$ stands for fAPAR computed at ESU$_n$

while$fAPAR_{PASTIS-AVG}$ stands for fAPAR computed averaging transmitted PAR ($PAR_b^{\downarrow}$) of ESUs 1-9.

4.3.4.3. Estimation of fAPAR from DHPs

Among other measurements related to canopy architecture (e.g., LAI), hemispherical photos allow the computation of fAPAR by measuring the directional gap fraction [277,281]. In fact, as the photosynthetically active radiation domain (PAR, 400-700 nm) is characterized by strong absorbing features of the photosynthetic pigments [282], fAPAR is often assumed to be equal to fIPAR (Fraction of Intercepted Photosynthetically Active Radiation)[252], and therefore is directly related to the gap fraction. According to this assumption, CAN-EYE software proposes three outputs for fAPAR: the instantaneous black-sky (or direct) fAPAR; the daily integrated black-sky fAPAR and the white-sky (or diffuse) fAPAR. In our study, we selected the instantaneous black-sky fAPAR at 10:00 a.m. ($fAPAR_{10h}^{BS}$) for consistency with satellite products and we refer to it as fAPAR$_{\mathrm{DHP}}$. According to CAN-EYE output variable description [283], fAPAR$_{\mathrm{DHP}}$ was computed using the following equation:

$$fAPAR_{DHP} = fAPAR_{10h}^{BS} = 1 - P_0(\theta_S)|_{S=10h} \qquad (4.3)$$

where P_0represents the measured gap fraction on each viewing zenith angle θ and $\theta_S$is the sun zenith angle at 10:00 local solar time [283].

4.3.5. Validation approach

To perform a direct validation of medium resolution satellite products we need to account for the differences in scale between the footprints of the ground measurements and the satellite sensor. For this reason we followed the bottom up approach proposed by the CEOS LPV sub-group summarized in Figure 4.3. This approach consists of using high-resolution imagery and robust regression methods to up-scale the ground measurements from ESU values to the site level. The resulting ground-based map can then be aggregated to the spatial resolution of the satellite product to be validated. The first step was deriving an empirical transfer function (TF) that establishes a relationship between the fAPAR$_{\mathrm{DHP}}$ values, the only available at all the 15 ESUs plus additional control values obtained in prairie and over bare areas, and the multispectral radiometric values from the high-resolution Landsat-8 imagery [284] (Section 3.5.1). The ground-based high-resolution maps, derived from the selected transfer function, were then remapped to the spatial support of GEOV1 and MODIS products (i.e., 1 km and 500 m), taking into account the equivalent Point Spread Function (PSF) of the satellite sensors [269] (Section 3.5.2). Finally, the aggregated maps were compared to the moderate resolution fAPAR products under study and validation statistics were computed for the accuracy assessment (Section 3.5.3).

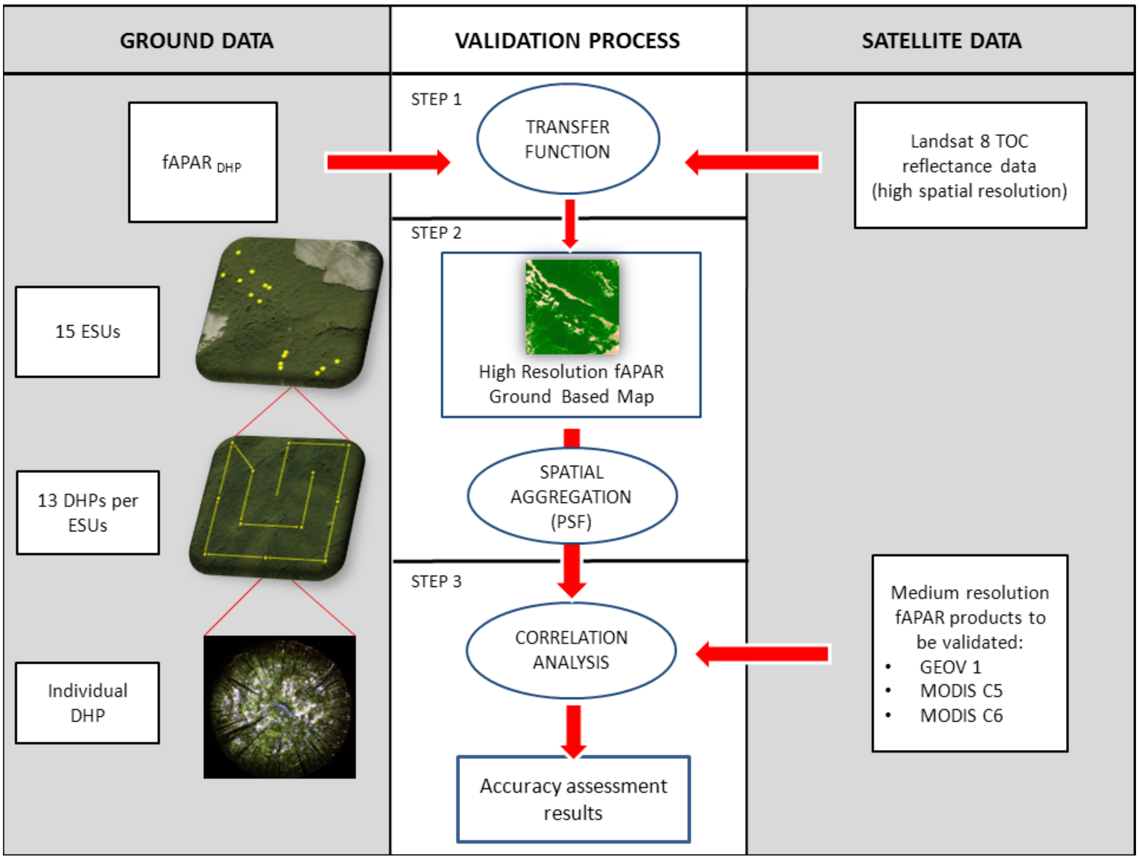

Figure 4.3. Bottom-up approach for the upscaling process used in the present study. 13 DHPs measurements were collected at every ESU and 15 ESUs were sampled over the site. Radiometric values over a decametric image (Landsat-8) were extracted over the ESUs and used to develop empirical transfer functions for upscaling the ESU ground measurements. The resulting high-resolution map was aggregated to the spatial resolution of the satellite product to be validated, taking into account the equivalent Point Spread Function (PSF) of the satellite sensors. A correlation analysis was performed to accomplish the accuracy assessment.

4.3.5.1. Empirical transfer function

For the up-scaling of the ground measurements at the site level, we need to establish an empirical relationship (transfer function) between the fAPAR ground values and concomitant radiometric values of a high-resolution imagery. For this purpose, Landsat-8 top-of the canopy reflectance images of 30m spatial resolution were selected. Landsat-8 images are freely available at the USGS earth explorer portal (http://earthexplorer.usgs.gov/). The acquisition date was 10th July and 27th August 2015, for the first and second campaign, respectively. For the second campaign, the date of acquisition is around one month earlier that the ground sampling, due to cloud contamination of concomitant Landsat-8 acquisitions for the September campaign. However, as ground measurements showed a high stability from July to the end of September, we assumed also stability in the radiometric signal of the image during this period.

A multivariate ordinary least square (OLS) regression was used for modeling the relationship between $fAPAR_{DHP}$ (our response variable) at the ESU level and the radiometric information of the Landsat-8 image (predictor variable) [284]. The multivariate OLS function proposed in this work uses an iteratively re-weighted least squares (IRLS) algorithm in order to minimize the influence of outliers as proposed by Martinez et al. [284]. This method allows combining the information provided by different bands and evaluating the band combination that exhibits the lowest error. This modeling approach has been recently used for up-scaling biophysical variables such as LAI, fAPAR and fCOVER over a network of cropland sites in the ImagineS project (fp7-imagines.eu/). The basis is that outliers in the sampling distribution will result in biased estimates of model parameters. The IRLS algorithm includes an additional scale factor (i.e. weight) in order to adjust the amount of influence each response value has on the model estimates [284]. The following bands were considered: B3 (green: 0.53-0.59 µm), B4 (red: 0.64-0.67 µm), B5 (NIR: 0.85-0.88 µm), B6 (SWIR1: 1.58-1.65 µm). Due to the well-known linear or approximately linear relationship between fAPAR and NDVI [45,106,120,285–287], we also used B4 and B5 to compute NDVI [43] for additionally use it as predictor variable (Equation 4.4). In addition to the ESU measurements over the forest, additional values over bare areas and prairie were used to better constrain the model for low fAPAR values. Control points included 4 bare areas that were visually selected with GoogleEarth® around the study area, with NDVI ranging between 0.06 and 0.17, and where fAPAR was set to 0. Furthermore, an additional ESU located over a prairie area with DHP measurement was used to calibrate the empirical transfer function in order to have intermediate values of fAPAR. The obtained value with CAN-EYE for the black-sky fAPAR at 10h over the prairie ESU was 0.73.

In order to assess the model performance and evaluate the optimal predictor three different errors were computed: the root mean square error (RMSE), the weighted RMSE (RW, using the weights attributed to each ESU) and the cross-validation RMSE (RC, leave-one-out method). RMSE and RW provides an estimate of the mean prediction error of the model considering all the observations, whereas RC provides a more reliable model performance since it gives an indication of how well the function will predict data not included in the data set used to derive the predictor [288]. The NDVI was chosen as input for the transfer function because it shows lower RC errors than other band combinations for the first, the second and the combined campaigns [289]. Table 4.3 shows the errors (RMSE, RW, RC) obtained for the selected transfer function using the NDVI for the first and the second campaign, as well as when the data of the two campaigns were pooled together. It can be noticed that all the different cases show very low RMSE errors, below GCOS requirement on accuracy [270], and very high correlation coefficients (> 0.99) with almost no mean bias (Table 4.3). The higher errors obtained for the second campaign could be partly attributed to the period between the collection of ground measurements (end of September) and the imagery acquisition (end of August). Finally, we selected the transfer function based on the two ground campaigns in order to reduce errors of the second campaign, with a final cross-validation RMSE of 0.049.

The empirical relationship selected for our site is the following linear relationship based on NDVI computed from Landsat red (B4) and NIR (B5) bands:

$$fAPAR = -0.1799 + 1.2258 \text{ x} \left(\frac{\rho_{NIR} - \rho_{red}}{\rho_{NIR} + \rho_{red}}\right) \tag{4.4}$$

Where ρ_{NIR} and ρ_{red} is the reflectance in the near infrared and red, respectively.

The high-resolution ground-based maps over the site are shown in Section 4.2.

Table 4.3. Performance metrics of empirical transfer function. Positive Bias indicates overestimation of the transfer function estimates. RC stands for cross-validated RMSE, RW stands for weighted RMSE.

Field campaigns	R^2	Bias	RMSE	RC	RW
8 July 2015	0.999	-0.001	0.015	0.018	0.015
25 September 2015	0.995	-0.009	0.041	0.063	0.062
Both campaigns	0.995	-0.003	0.03	0.049	0.025

Finally, the convex hull technique described by Martinez et al.[284] was applied to characterize the representativeness of ESUs and the reliability of the empirical transfer function. This technique will allow us to derive a quality assessment image to highlight areas on the fAPAR maps with higher or lower confidence of the estimates due to the model errors and sampling strategy. Briefly, this method defines a convex region defined from the data set containing the spectral information of the *in-situ* measurements and can be applied using multiple spectral bands combinations in agreement with our multivariate OLS approach for selecting the optimal band combination for the transfer function. This region delimits the domain where the transfer function behaves as interpolator (namely ‘strict convex hull’). Conversely, outside this domain, the transfer function behaves as extrapolator. However, the convex hull could be slightly expanded by ± 5% of reflectance (namely ‘large convex hull’) to allow pixels very close to the strict convex hull to be used since they are expected to provide reasonable results. Hence, this test was carried out using the red (B4) and NIR (B5) bands of the Landsat-8 images used for the NDVI computation.

4.3.5.2 Spatial Aggregation

The comparison between the ground-based maps with moderate-resolution products requires a consistent statistical support area. This apparently simple problem should be considered carefully if all uncertainties associated to satellite products are to be recognized [269]. Firstly, the satellite products and the high-resolution maps were projected to the same coordinate system. The *Plate Carrée* projection of GEOV1 product was used for the comparison at both 1 km and 500 m. A spatial window of 5 km x 5 km centered over the tower was selected for the comparison. Secondly, the high-resolution map was aggregated to the spatial resolution of the satellite product according to the effective point spread function (PSF) of the satellite product, which improves the performance of the evaluation as compared to ordinary average [290]. The equivalent PSF results from a number of steps that need to be considered. The instrument PSF depends on several components: the electronic PSF, the detector PSF, the image motion PSF, and the optical PSF [291]. According to Duveiller et al. [292], electronic and image motion PSFs can be neglected. The PSF for the MODIS and PROBA-V instruments can be approximated by the convolution of a Gaussian function characterizing the optical PSF. The ground-based map equivalent PSF was computed by maximizing the correlation coefficient between the low resolution (LR) product (i.e. GEOV1, MODIS C5 and C6) and the corresponding higher resolution (HR) image. During the optimization process of the PSF, we used an iterative approach in which we combined the extension of the pixel size and the PSF characterized by the Full Width at Maximum (FWHM) of the two Gaussian functions in both directions x and y. The extension of the pixel was combined in steps of 30 m (HR) up to the pixel size of the corresponding LR product.

4.3.5.3 Correlation analysis

The accuracy assessment between the ground-based maps and the satellite products to be validated was performed at the resolution of the satellite product to evaluate on a pixel per pixel basis. The comparison was performed between the closest product date to the field campaign. The accuracy was quantified by several validation metrics reporting the goodness of fit between the products. Total measurement uncertainty (i.e., root mean square error, RMSE) includes systematic measurement error (i.e. Bias) and random measurement error (i.e., Standard deviation of bias). RMSE corresponds to the accuracy as there is only one product estimate for each mapping unit [293]. RMSE is recommended as the overall performance statistic. Linear model fits were also used to quantify the goodness of fit. For this purpose, Major Axis Regression (MAR) was computed instead of OLS because it is specifically formulated to handle error in both the x and y variables [294]. Finally, the number of pixels within the GCOS requirements was quantified. Table 4.4 summarizes the uncertainty metrics associated with the scatter-plots.

Table 4.4. Uncertainty metrics for product validation.

Gaussian Statistics	Comment
N: Number of samples	Indicative of the power of the validation
RMSE: Root Mean Square Error	Indicates the Accuracy (Total Error). Relative values between the average of x and y were also computed.
B: Mean Bias	Mean difference between pair of values (y-x) Indicative of accuracy and possible offset. Relative values between the average of x and y were also computed.
S: Standard deviation	Indicates precision.
R^2: Correlation coefficient.	Indicates descriptive power of the linear accuracy test. Pearson coefficient was used.
Major Axis Regression (slope, offset)	Indicates possible bias.
% GCOS requirements	Percentage of pixels matching the GCOS requirements.

4.4. Results

4.4.1. Consistency of ground fAPAR estimates

We investigated the temporal course of PASTIS sensors by comparing $fAPAR_{PASTIS-ESU1}$ with $fAPAR_{APOGEE}$ at ESU1 during 2015. Figure 4.4 shows synchronism between $fAPAR_{APOGEE}$, which represented our benchmark, and $fAPAR_{PASTIS-ESU1}$. At the end of April (DOY 110-120), $fAPAR_{APOGEE}$ values ranged between 0.55 to 0.65. Starting from the last decade of May (DOY 139) until the first decade of October (DOY 283), $fAPAR_{APOGEE}$ presented fairly constant values of 0.93-0.96 during the whole period. During this phase, both the average of $fAPAR_{APOGEE}$ and $fAPAR_{PASTIS}$ was 0.94, with a standard deviation (σ) of 0.007 for $fAPAR_{APOGEE}$ and 0.010 for $fAPAR_{PASTIS}$. The longest gap of our dataset occurred from DOY 210 to 230 when values were presumably stable as included in the peak-season. $fAPAR_{APOGEE}$ values started to decline at mid-October decreasing constantly and continuously until the end of the year, except for the first two weeks of November when values appear constant around 0.78-0.79. While the evolution between $fAPAR_{APOGEE}$ and $fAPAR_{PASTIS}$ was in agreement during the peak-season, both fAPAR values fluctuated more evidently during the senescence phase (DOY 266-280). Peak value detected by both techniques was 0.96 associated to DOY 198 for Apogee sensors and to DOY 194 for PASTIS sensors. fAPAR values measured with PASTIS sensors strongly correlated with those measured with Apogee sensor (R^2 = 0.84; RMSE=0.01), although a bigger fluctuation was observed in the senescence phase (fAPAR<0.9, Figure 4.5) as formerly evidenced by the seasonal patterns (Figure 4.4).

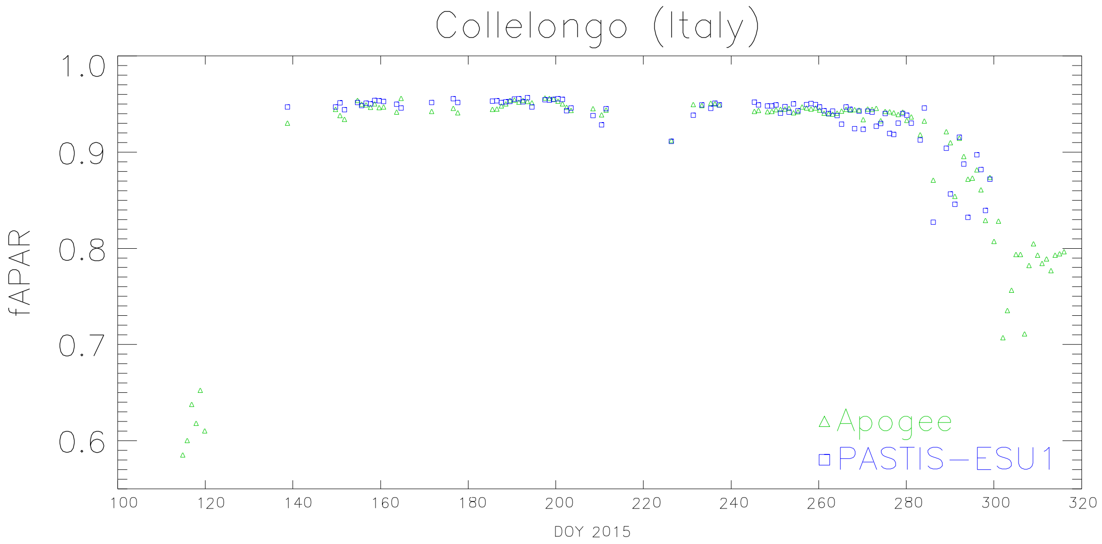

Figure 4.4. Temporal course of $\mathrm{fAPAR}_{\mathrm{APOGEE}}$ (green triangles) and $\mathrm{fAPAR}_{\mathrm{PASTIS\text{-}ESU1}}$ (blue squares) at ESU 1 during 2015 (DOY = Day Of Year).

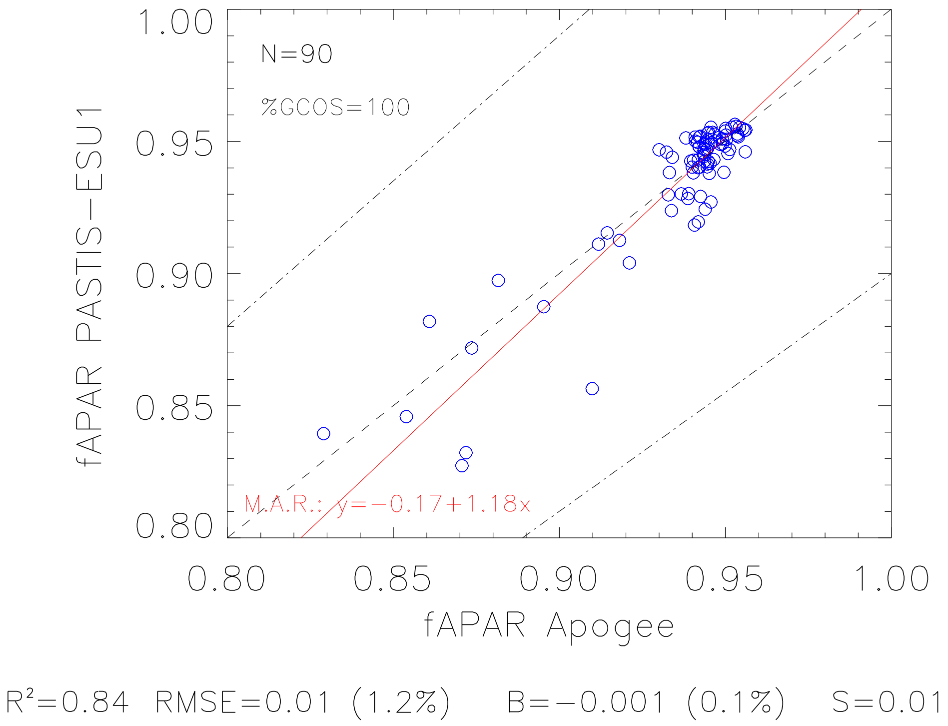

Figure 4.5. Correlation between $\mathrm{fAPAR}_{\mathrm{PASTIS\text{-}ESU1}}$ and $\mathrm{fAPAR}_{\mathrm{APOGEE}}$ for Collelongo site in 2015 (DOY 139-300). Number of samples (N), Major Axis Regression (M.A.R.), correlation (R^2value), RMSE, Bias (B) and Standard deviation (S), and percentage of values matching the GCOS requirements (%GCOS) are displayed. Dashed lines correspond to the 1:1 line and GCOS uncertainty levels, red continuous line corresponds to the M.A.R.

Data from PASTIS and DHP sensors at the different ESUs were compared for the two DHP sampling campaigns. $fAPAR_{DHP}$ ranged from 0.92 to 0.96 for the campaign in July, while $fAPAR_{PASTIS}$ presented values between 0.95 and 0.96 (Figure 4.6a). Generally, $fAPAR_{PASTIS}$ was higher than $fAPAR_{DHP}$ and in agreement with it, except for ESU 5-8. During September campaign, $fAPAR_{DHP}$ resulted generally lower than $fAPAR_{PASTIS}$ (Figure 4.6b). In the late summer campaign, while $fAPAR_{PASTIS}$ varied between 0.94 and 0.96, $fAPAR_{DHP}$ spanned from 0.89 to 0.96. Analyzing the standard deviation (errors bars) of the measurements, it appeared that $fAPAR_{PASTIS}$ had less variability among the single replicates compared to $fAPAR_{DHP}$ during both campaigns (Figure 4.6). Nevertheless, fAPAR estimated from DHP based on gap fraction was consistent with $fAPAR_{PASTIS}$ within the range of accuracy required for satellite products (max(0.05, 10%)).

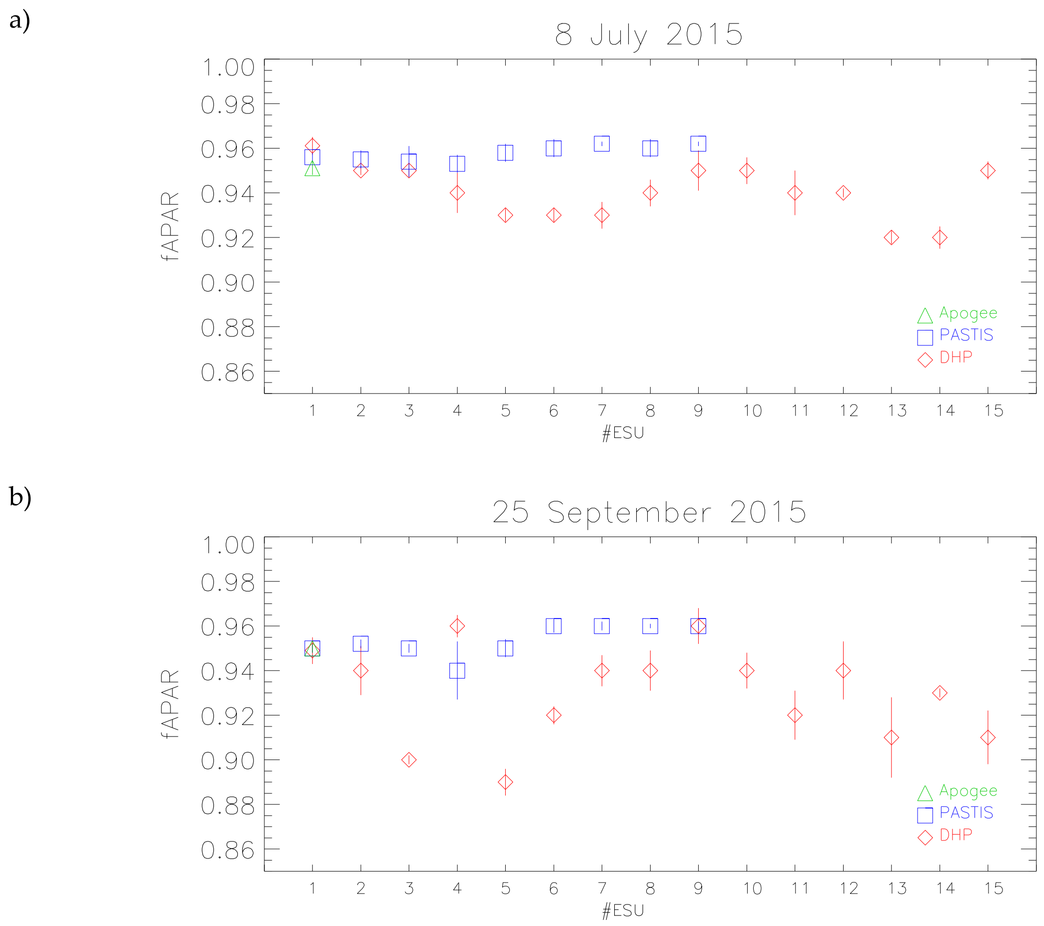

Figure 4.6. Spatial variation of $fAPAR_{APOGEE}$, $fAPAR_{PASTIS}$ and $fAPAR_{DHP}$ values distributed by ESUs on 8 July 2015 (**a**) and 25 September 2015 (**b**). Error bars are expressed as standard deviation.

4.4.2. High-resolution ground-based maps

High-resolution ground-based fAPAR maps were computed with a single transfer function for both dates (Equation (4.4)). Figure 4.7a shows the spatial distribution of the retrievals over the study area, which displayed homogeneous areas of dense vegetation with high fAPAR values and some patches of low photosynthetic activity that correspond to montane prairie and/or bare rock/soil areas.

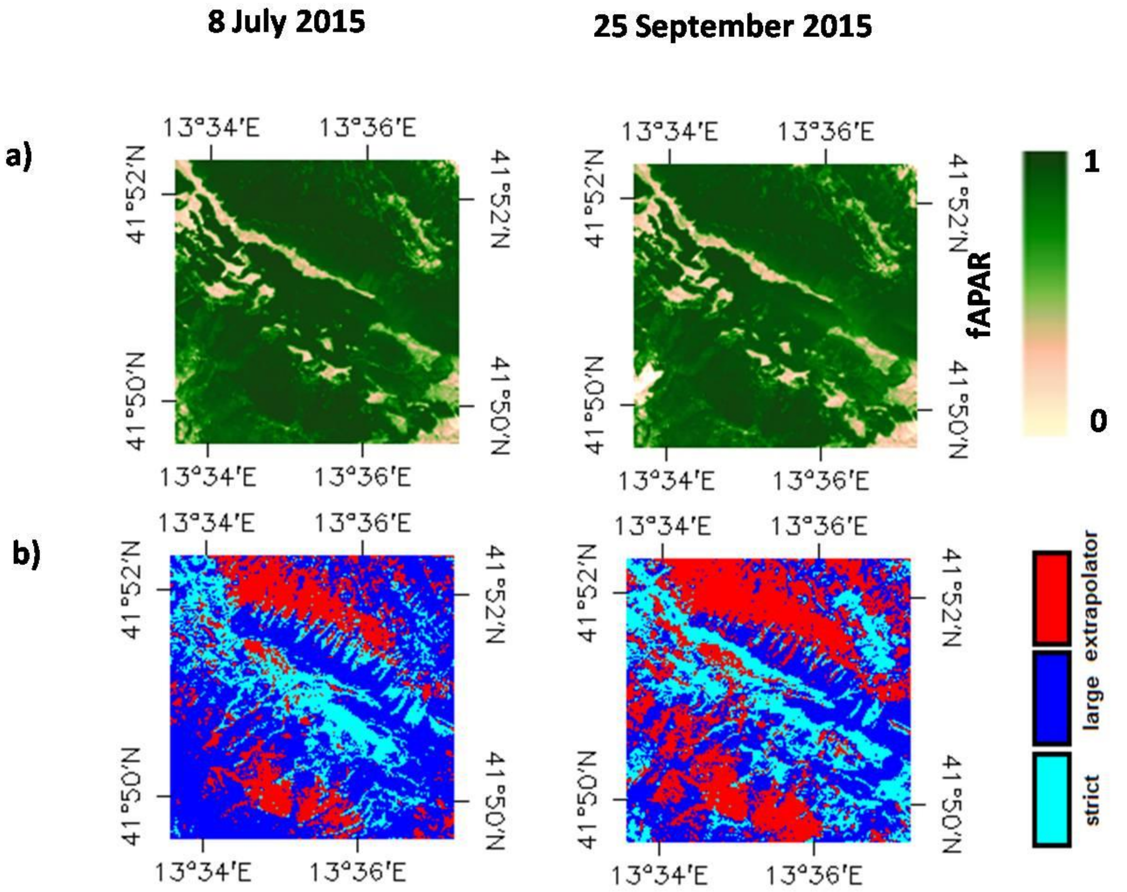

Figure 4.7. (a) Ground-based high-resolution maps (5 km x 5 km) of instantaneous black-sky fAPAR at 10:00 a.m. over Collelongo site (Italy). (b) Convex Hull test over 5 km x 5 km: clear and dark blue correspond to the pixels belonging to the 'strict' and 'large' convex hulls, respectively. Red corresponds to the pixels for which the transfer function behaves as extrapolator. Left: First field campaign (8 July 2015). Right: Second field campaign (25 September 2015).

Mean fAPAR value over 3-km x 3-km centered at the tower was 0.85 (σ=0.13) for the July campaign and 0.85 (σ=0.14) for the September campaign. The scatter-plot between ground observations (DHP) and the corresponding transfer function estimate showed the good agreement achieved (RMSE = 0.03) with a slight over-estimation for bare areas' control points of less than 0.05 units, and some scattering for ESUs in the second campaign (Figure 4.8). The only ESU over prairie shows good agreement very close to the 1:1 line. The stability of fAPAR values between July and September was supported by net ecosystem exchange (NEE) values, which also presented a limited difference between the two dates (NEE between 10 a.m. and 11 a.m. equal to -16.9 and -14.1 for 8 July and 25 September 2015, respectively).

The quality assessment images (Figure 4.7b) derived from the convex hull technique are informative of the reliability of the estimates, showing higher reliability for those pixels inside of the 'strict' (in clear blue) and 'large' (in dark blue) convex hull. Blue pixels are mainly located around the tower site where the sampling was performed. The 'strict' and 'large' convex-hulls reached 79% and 65% of the pixels for the first and second field campaign, respectively. There is a quite consistent red area at the top and the bottom of the image that corresponds to the pixels where the transfer function behaves as extrapolator. This red area corresponds to areas with different topography or to montane prairie areas which were not included in our spatial sampling scheme. Note that the convex-hull test provides information on the representativeness of the sampling, but does not necessarily imply poor extrapolation capabilities of the transfer function, mainly on the same land cover type.

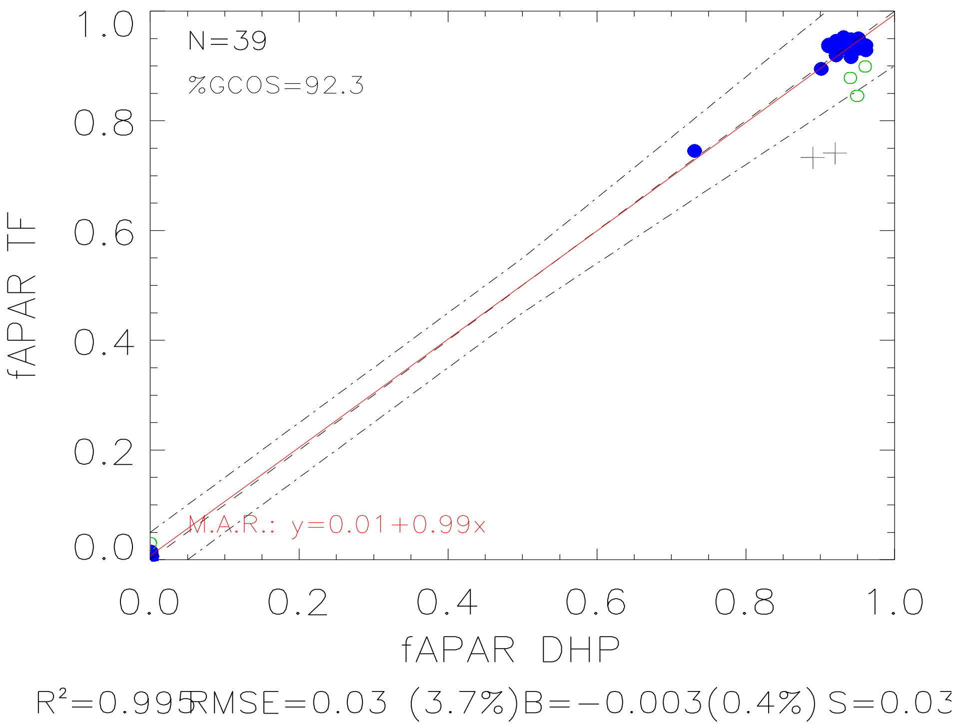

Figure 4.8. Scatter-plot of ground-based map data (fAPAR-TF) *vs* ground estimates ($fAPAR_{DHP}$). Filled blue dots: Weight > 0.7. Empty green dots: 0 < Weight < 0.7. Grey Crosses: outliers. First field campaign on 8 July 2015 and second field campaign on 25 September 2015.Number of samples (N), Major Axis Regression (M.A.R.), correlation (R^2value), RMSE, Bias (B) and Standard deviation (S), and percentage of values matching the GCOS requirements (%GCOS) are displayed. Dashed lines correspond to the 1:1 line and GCOS uncertainty levels, red continuous line corresponds to the M.A.R.

4.4.3. Validation of satellite fAPAR products

4.4.3.1. Temporal consistency

The temporal variations of the three satellite products under study was evaluated over ESU 1, located at the Collelongo flux tower, where continuous fAPAR measurements were acquired (Figure 4.9) during the 2014-2015 period. Figure 4.9 displayed ground and satellite acquisitions at daily temporal frequency during the stable season (from the end of May till the end of September) and during the vegetation decrease season (from early October onwards). The initial phase of the growing season was not captured by ground measurements in any of the two years.

During the stable vegetative season, PROBA-V GEOV1 fAPAR product provided very stable temporal trajectories, in line with ground acquisitions. However, a negative bias (PROBA-V GEOV1 fAPAR < ground fAPAR) was observed, that could be partly explained due to the different footprint of satellite pixel (1 km) as compared to ground data (observations at the station level). Regarding both MODIS fAPAR products, lower discrepancies in magnitude were found against ground observations as compared to that for GEOV1, particularly in 2015. In line with previous studies [258,265], noisy temporal retrievals were found for MODIS products over forest areas, with variations of ±0.1 fAPAR units.

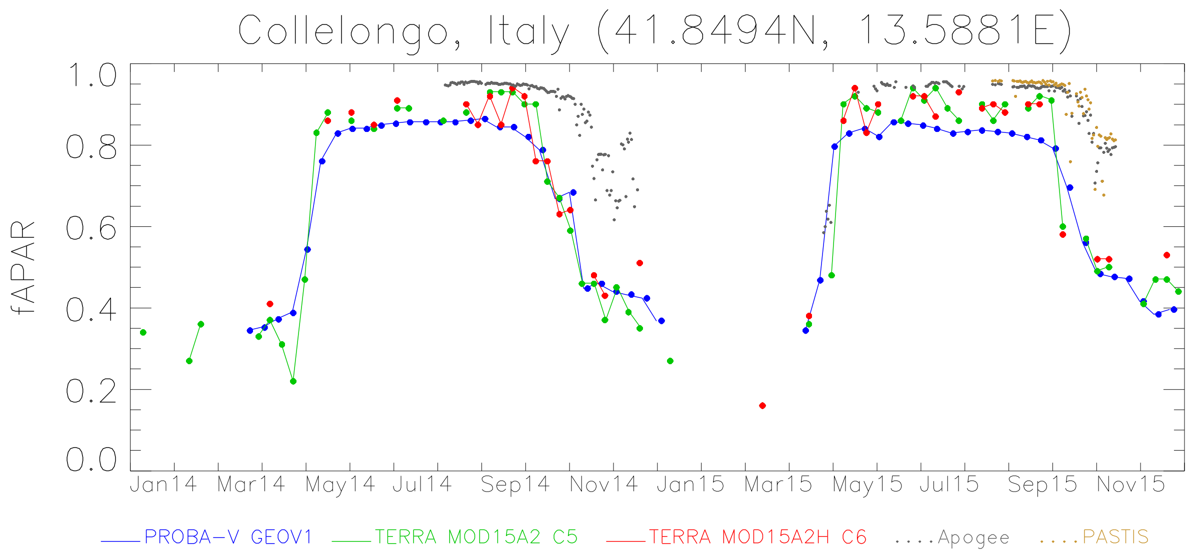

Figure 4.9. Temporal trends of fAPAR from GEOV1, MODIS C5 and MODIS C6 satellite products over Collelongo flux tower (ESU 1), and continuous ground values of $fAPAR_{APOGEE}$ and $fAPAR_{PASTIS-AVG}$. Note that only pixels classified as 'High Quality' and 'Useful' according to Table 2 are displayed.

4.4.3.2. Accuracy Assessment

Figure 4.10 shows the scatter-plots between different satellite products and ground-based high-resolution maps. The validation metrics are provided in Table 4.5 considering all data points or only high quality and useful pixels.

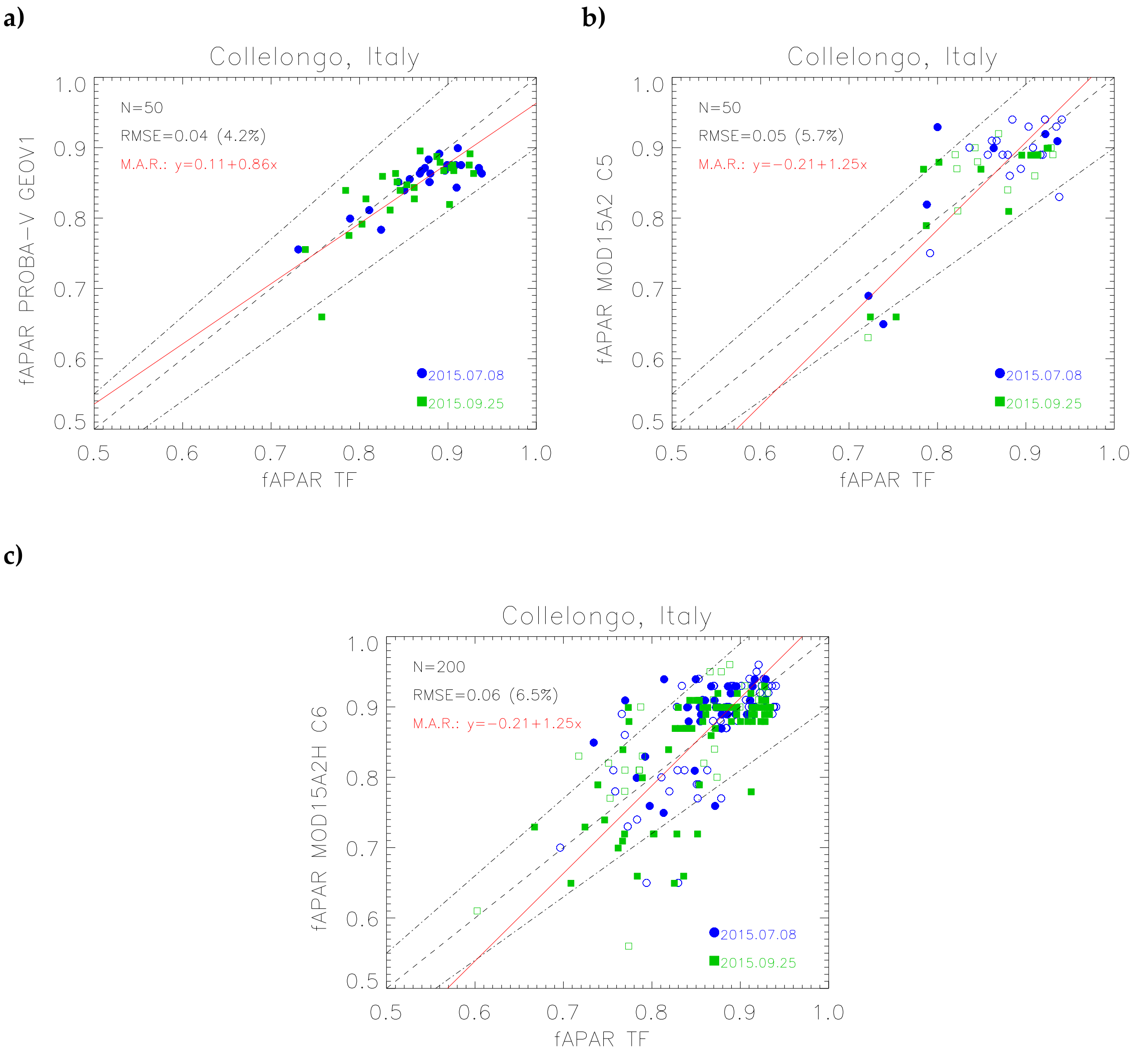

Figure 4.10. Direct validation results: comparison of GEOV1 (panel a), MODIS C5 (panel b) and MODIS C6 (panel c) fAPAR products with the fAPAR ground-based maps at the each satellite product resolution (1km for both GEOV1 and MODIS C5, and 500 m for MODIS C6). Filled symbols correspond to 'high quality' and 'useful' pixels, non-filled symbols correspond to 'Poor quality' pixels. Number of samples (N), Major Axis Regression (M.A.R.), correlation (R^2 value), RMSE, Bias (B) and Standard deviation (S), and percentage of values matching the GCOS requirements (%GCOS) are displayed. Dashed lines correspond to the 1:1 line and GCOS uncertainty levels, red continuous line corresponds to the M.A.R.

PROBA-V GEOV1 fAPAR product showed the lowest RMSE of 0.04 with low negative bias (-2.6%) mostly observed for the highest values. Almost all the points (98%) lied within the GCOS requirements on accuracy (dashed lines in Figure 4.10). On the other hand, similar accuracy was obtained for MODIS C5 and C6 products, with RMSE of 0.05 and 0.06 respectively, considering all pixels, almost no mean bias and a percentage of pixels within the GCOS requirements of 90 and 88%, respectively. The slightly lower accuracy was expected due to the lower precision (i.e., higher fluctuations) previously observed in MODIS products. The finer spatial resolution of MODIS C6 (500m) as compared to MODIS C5 (1km) had only a minor impact on accuracy. In terms of the major axis regression (MAR) lineal model, GEOV1 product has slight better performance as compared to MODIS C5 and C6, with low offset and slope closer to 1. MODIS C6 and C5 provides good match for highest values but shows a tendency to provide lower fAPAR retrievals for the lower values. The validation metrics were very similar when considering all pixels or only high quality and useful pixels, which indicates that in this case the MODIS back-up algorithm based on NDVI performs quite well, even if the quality flag informed on cirrus, cloud or cloud shadow detected.

Table 4.5. Performance metrics of each fAPAR satellite product versus ground-based maps. For RMSE and Bias (negative value means underestimation of the satellite product and vice versa), the relative values are displayed in brackets.

	PROBA-V GEOV1	**MODIS C5 (All points)**	**MODIS C5 (High quality and Useful)**	**MODIS C6 (All points)**	**MODIS C6 (High quality and Useful)**
N	50	50	20	200	113
RMSE	0.04 (4.2%)	0.05 (5.7%)	0.06 (6.7%)	0.06 (6.5%)	0.06 (6.5%)
R^2	0.63	0.6	0.63	0.46	0.41
Bias	-0.02 (2.6%)	-0.001 (0.2%)	0.005 (0.6%)	0.003 (0.3%)	0.003 (0.3%)
S	0.03	0.05	0.06	0.06	0.06
Offset (MAR)	0.011	-0.21	-0.23	-0.21	-0.23
Slope (MAR)	0.86	1.25	1.26	1.25	1.25
% GCOS	98	90	85	88	88

4.5. Discussion

4.5.1. Consistency of ground fAPAR estimates

Seasonal dynamics of different ground fAPAR were compared to check their consistency. First, we compared fAPAR$_{APOGEE}$ and fAPAR$_{PASTIS}$ at ESU 1 ($R^2 = 0.84$; RMSE=0.01), which are the continuous datasets available at the Collelongo site. In general, despite considerable gaps that hindered the green-up observation, it was possible to evaluate the temporal evolution from May to November. This is also confirmed by the good agreement between the seasonal maximum values of fAPAR which are only 4 days shifted (DOY 198 for Apogee and DOY 194 for PASTIS). Recently, PASTIS sensors were also used to collect continuous ground measurements mainly in croplands and grasslands [295]. Although few studies [84,85] consider PASTIS performance for tracking seasonality over crop sites, we are not aware of any study checking PASTIS performance in a deciduous forest site. Our study reveals that $fAPAR_{PASTIS}$ appropriately followed the seasonal trends depicted by $fAPAR_{APOGEE}$. Fluctuations in fAPAR values within DOY 266 and 280 were due to falling leaves, senescence and gaps that can lead to more variable averages compared to the fully leafy season (Figure 4.4). In our formulation of $fAPAR_{PASTIS}$, we used PASTIS sensors just to calculate PAR transmitted through the canopy at the different ESUs, while other PAR components (incident, reflected by the canopy and reflected by the soil) were computed from Apogee sensors at ESU 1. Congruent with the results at ESU 1 (Figure 4.4), we support that one PASTIS system made up of six quantum sensors spatially distributed under a dense canopy cover such as in our forest, can be used to monitor transmittance as, especially in the peak season, it gives results in agreement with the 15 Apogee sensors measuring below canopy transmittance.

Next, $fAPAR_{PASTIS}$ and $fAPAR_{DHP}$ at the different ESUs were compared for the two DHP sampling campaigns. The measurements presented in this study indicate a homogeneous canopy structure for Collelongo forest site within 1 km x 1 km of ground sampling area, with stable values for $fAPAR_{PASTIS}$ over the ESUs and more varying values for $fAPAR_{DHP}$ (Figure 4.6). This slight dissimilarity could be primarily attributed to three reasons: 1) different retrieval approach and definition, 2) different sampling strategy (Figure 4.2) and spectral range and 3) the classification errors during image processing (required to compute gap fraction) which could be the main source of variability in DHP processing as it is partly subjective (depending on the operator) [281,296]. In general, as highlighted by Majasalmi et al.[266], few studies have accurate ground truth measurements in forest ecosystems. Regarding the scarcity of ground reference data, we found that, for example, in the context of the On Line Interactive Validation Exercise (OLIVE) platform, no ground fAPAR reference data are available in Italy and only one site outside Europe is available for deciduous broadleaf forest within the 113 DIRECT sites dedicated to the validation of global biophysical products [268]. Being *Fagus sylvatica* one of the major forest trees in Europe [297], our ground reference data results relevant in the context of validation of satellite products in this kind of ecosystem. In our work, radiometric values of decametric images (Landsat-8) were extracted over the ESUs and used to develop empirical transfer functions for upscaling the ground measurements. As noted by Cohen et al. [298], the selection of the optimal transfer function is site specific. Our empirical transfer function is a linear relationship with the NDVI, in agreement with other works [99,106,287], that has been calibrated using maximum fAPAR values collected in the forest and minimum values of identified bare soils. This linear relationship shows also good results for the one control point of the mountain prairie, which seems to confirm the validity of the empirical function over prairie areas. However, one control point is not enough to verify the validity of the transfer function over mountain prairie and some uncertainties remains over these small areas

4.5.2. Accuracy Assessment

Seasonal variations of the satellite products have been compared to the Apogee and PASTIS ground measurements. The three satellite products displayed a rapid increase at the start of the season as observed in other deciduous forest sites [32]. In addition, slightly smoother variations were observed in GEOV1 due to its larger compositing period. The decline of the vegetation season started earlier for satellite products as compared to ground acquisitions, which was mainly observed in 2014. This can be partly explained by the different temporal composition of satellite products, but also due to the fact that satellite products are defined to be sensitive to photosynthetically active elements whereas ground devices are measuring total canopy fAPAR, and the contribution of NPV elements is significant during the fall [280]. Small changes in the concentration of chlorophyll pigments at the end of the season could have a stronger impact in the satellite products, designed to be sensitive to this absorption band, than in the ground fAPAR where the absorption of PAR in green-to-yellow leaves vary in a smooth way as observed in Figure 4.9.

Accuracy assessment results shows a good agreement with ground-based fAPAR values for the three satellite products (GEOV1, MODIS C5, MODIS C6) with more than 85% of the samples within GCOS requirement on accuracy, and up to 98% of the samples in the case of GEOV1. The good match for highest values confirms the ability of the satellite products under study to retrieve very high fAPAR values. The largest values obtained for GEOV1 (around 0.9) are slightly lower than those of the ground-based measurements (around 0.95), whereas MODIS C5 and C6 reached similar larger values than ground-based maps with the backup algorithm. The ground measurement is however a measure of the total canopy fAPAR. A limitation of this validation exercise is that it was not able to decouple green fAPAR (close to satellite definition) from total canopy fAPAR in ground measurements, although the relative contribution of NPV elements to the canopy fAPAR is expected to be very small (<0.1) during the peak season [66]. Even with this uncertainty on NPV contribution to the canopy fAPAR, and other uncertainties regarding ground measurement, up-scaling process and match-ups, our validation results for this complex, montane, beech forest and prairie site are encouraging. Our results demonstrate that in a large number of GEOV1 and MODIS C5 and C6 fAPAR retrievals, GCOS requirements are met.

4.6. Conclusions

In this study PROBA-V GEOV1 (1 km), MODIS C5 (1 km) and MODIS C6 (500 m) fAPAR satellite products were validated against ground references at a broadleaf deciduous forest site in Italy. This type of forest is an example of an ecosystem where a lack of field data and validation studies is widely recognized. The ground measurements were collected using Apogee PAR sensors, PASTIS-PAR sensors and digital hemispherical photographs (DHPs), following different spatial and temporal sampling schemes. Apogee PAR sensors installed over the Collelongo tower were used as a benchmark for continuous fAPAR measurements. PASTIS sensor installed around the site were calibrated with Apogee for obtaining continuous fAPAR values representative of an extended area. Finally, hemispherical photographs were collected over 15 ESUs in two intensive campaigns. The accuracy assessment exercise was successfully carried out following the bottom up approach proposed by the CEOS LPV sub-group using high-resolution imagery and robust regression methods to up-scale the ground fAPAR measurements from ESU values to the site level. All $fAPAR_{DHP}$ measurements plus additional bare and prairie points were used together for deriving the empirical transfer function.

A good consistency among three ground devices was found. PASTIS-PAR sensors were found reliable for monitoring the canopy transmittance, showing very good agreement with Apogee (RMSE=0.01). $fAPAR_{DHP}$ estimates were also found reliable and consistent with PASTIS with absolute differences typically lower than 0.03, making this device particularly suitable for experimental campaigns over forest sites with no permanent instrumentation.

The three satellite products under study showed good accuracy results over the peak season, with RMSE values of 0.04, 0.05 and 0.06 for GEOV1, MODIS C5 and MODIS C6, respectively. The three fAPAR satellite products meet GCOS requirements on accuracy in more than 85% of cases for MODIS products, and up to 98% of samples for GEOV1, in this mosaic of deciduous beech forest and mountain prairie landscape. Very good consistency was found between MODIS C5 and C6, with slightly larger dispersion found for C6 due to the enhanced spatial resolution, which does not introduce systematic differences.

The temporal courses were also found reliable for the three satellite products, showing smoother GEOV1 profiles due to its longer compositing period. Larger discrepancies were observed at the end of the season as the contribution of non-photosynthetically active vegetation to the ground fAPAR values increases, showing a more rapid decrease in satellite products than in-situ measurements.

The ground measurements and up-scaled ground maps are part of the ImagineS ground database freely available. The averaged values over 3 km x 3 km is expected to contribute to the updated of the CEOS LPV Direct database for validation of coarse satellite products. As a concluding remark, increasing efforts in ground truthing collection at more long term research forest sites are desirable to increase the accuracy of satellite derived fAPAR estimation, useful for modeling ecosystem productivity.

General conclusions

This research focused on the integration of different techniques to monitore vegetation productivity and plant status in two ecosystems, a prairie grassland and deciduous broadleaf forest. All the specific objectives of the work were reached combining different datasets together that are, in summary, eddy covariance, remote sensing, optical sensing, and various field sampling. The experiment presented in Chapter 2 provided a basis for assessing seasonal ecosystem productivity and gap filling of tower flux data comparing harvested biomass, net CO_2 flux, and NDVI values at a grassland site in Canada. The strong correlations between optical measurements and independently measured fluxes demonstrate the utility of integrating optical with flux measurements for gap filling, and provide a foundation for using remote sensing to extrapolate from the flux tower to larger regions (upscaling) for regional analysis of net carbon uptake by grassland ecosystems. While in the second chapter, the experiment was limited to three formulation of the most widely used index, the NDVI, in Chapter 3 we explored more than 20 different vegetation indices in relation with changes in C fluxes, pigments pools and chlorophyll fluorescence in a Mediterranean beech forest. An unexpected result was that, similarly to the grassland ecosystems, spectral indices mainly related to structure were the best proxies of C fluxes at the forest site. Considering the great diversity of the two kind of ecosystems, differing in latitude and climate, this finding suggested that structural parameters (leaf area, leaf status) are one of the main drivers of the C uptake capacity in both study sites, albeit ecosystem diversity. In Chapter 2, the grassland site showed comparable values of productivity between the two years of study. Differently, a clear difference in C sink capacity was evidenced at the beech site in the two years investigated (Chapter 3). This difference, supported also by the meteorological dataset, allowed further analysis of ecosystem functionality that lead to interesting relationships between leaf functional traits (electron transport rate, leaf chlorophyll and carotenoid composition) and spectral indices, proving that physiological changes occurring in a forest canopy can be captured by proximal sensing at seasonal scale. Spectral indices computed with optical measurements resulted to be reliable proxies for monitoring C fluxes and vegetation dynamics in abiotic environmental stress conditions. Thus, proximal remote sensing offered the possibility for a meaningful, physiological examination of whole ecosystem function, and can be seen as an emerging ecophysiological approach. In Chapter 2 and Chapter 3 spectral indices were computed using both broadband dual channel low-cost sensors and a hyperspectral sensors in the former case, and a multispectral sensor in the second case. In agreement with the proximal sensing community that do not draw attention on one particular instrument to be used for vegetation monitoring, we found reliable results for all the proximal sensors used, independently from the spectral bandwidth features (spectral resolution). Consequently, although hyperspectral data permit a detailed description of the investigated vegetation target, broadband low-cost sensors can replace more complex and expensive hyperspectral sensors at eddy covariance sites when the choice is limited by economic constrains. It is clear that the choice has to be done accordingly with the specific objective of the study. For example, broad band sensors are appropriate if the aim is to monitor vegetation greenness of the study site but spectral resolution could impact the results when more in deep and complicated phenomena are considered (i.e., far red fluorescence). However, in all the chapters field measurements (e.g., biomass harvesting, fluorescent parameters and pigment determinations at leaf level, ground fAPAR data) resulted essential for validation of proximal and remote sensing to larger area of investigations. Likewise, the integration of remote sensing with flux measurements improves our understanding of both fluxes and remote sensing.

The relationship between the NDVI and vegetation productivity is widely recognized at several ecosystem types, and the link between this index and the fAPAR has been well documented, theoretically and empirically. In Chapter 2 and Chapter 4 several methods of ground fAPAR measurements are presented. Clearly, measuring fAPAR at a forest site (Chapter 4) was more challenging and required additional efforts compared to short canopies (e.g., grasslands, Chapter 2). Especially in Chapter 4, proximal sampling was related to conventional remote sensing, providing critical validation (e.g., “ground truthing”) and extrapolation of fine-scale measurements to larger regions (“upscaling”). The productivity of a vegetated surface is related to fAPAR and remotely sensed fAPAR data are widely used as input in carbon productivity models. In this context, the focus on ground and satellite fAPAR (Chapter 4) lay the foundations and open future possibilities for estimating the productivity using the LUE model at the forest site, similarly to what has been done for the grassland site in Chapter 2. This could provide interesting opportunities for new advances in the framework of the rich history of the LUE approach, exploring different potential parameterizations of this model in a complex ecosystem such a mature deciduous forest site.

The overall conclusion of this study is that blending different approaches is a key benefit in our challenge to understand the fundamental “breathing” of the planet, moving away from rigid areas of expertise towards interconnected scientific communities. This integration offers greater comprehension of the underlying controls on biospheric-atmospheric fluxes than possible with either method alone.

Acknowledgements

The PhD research was possible thanks to a grant co-financed by the Department for Innovation in Biological, Agro-Food and Forest Systems (DIBAF) – Univesity of Tuscia, Viterbo, and the Institute of Agro-Environmental & Forest Biology (IBAF) – Italian National Research Council (CNR). The research was also possible thanks to several projects and grants: MIUR-CNR Next data project, Erasmus+ Higher Education Mobility Program, FP7 ImagineS project (FP7-SPACE-2012-311766), H2020 Ecopotential (grant agreement No. 641762), Rangeland Research University (University of Alberta), NSERC, iCORE/AITF, COST Action ESO903.

Particular thanks are due to Jorge Sánchez-Zapero, Consuelo Latorre, John Gamon, Giorgio Matteucci, Carlo Calfapietra, Fernando Camacho, Craig Emmerton, Christopher Wong, Donnette Thayer, Francesco Mazzenga, Daniela di Baccio and Antonella Castagna who highly contributed to this research.

In particular, I am very grateful to John Gamon who gave me the opportunity to collaborate with him at the University of Alberta, Canada. His personal and scientific guidance and knowledge have been invaluable for my PhD path. I would like to express sincere thanks to Fernando Camacho for providing me with the challenging occasion to collaborate with EOLAB during the last intense and productive summer in Valencia.

I also wish to thank Loris Vescovo, Saulo Castro, Akli Benali, Sofia Cerasoli, Duarte Oom, Gilberto Pastorello, Adrienne Tastad, Peter Carlson, Edwin and Ruth Mattheis, Piero Paris, Frédéric Baret, Marie Weiss, Giovanni De Simoni, Giuseppe Santarelli, María del Carmen Piñó Alcaide, Chris Mollica and Luca Leonardi. Thanks to all IBAF colleagues, especially to Guglielmo Santi, Luca Tosi, Marcello De Vitis, Francesca Brizi, and Michele Mattioni for their precious friendship and support.

I wish to thank my supervisor Carlo for his guidance and for being so demanding and rigorous during these years because it push me to give the best of me.

Thanks Andrea for your contagious passion and enthusiasm for science. Thanks for your stubbornness, advices, tips and late work in the office.

Thanks Daniela for being an example of professionality, dedication, commitment and precision in our work every day.

Thanks Giorgio for sharing your invaluable experience with me and support my activities during the PhD.

Finally, a very special thanks to my family, grandparents and Gregorio for handling the distance, being patience and supporting during these years mostly dedicated to PhD work.

References

1. McCallum, I.; Wagner, W.; Schmullius, C.; Shvidenko, A.; Obersteiner, M.; Fritz, S.; Nilsson, S. Satellite-based terrestrial production efficiency modeling. *Carbon Balance Manag.* **2009**, *4*, 8.

2. Thenkabail, P. S. *Land resources monitoring, modeling, and mapping with remote sensing*; II.; CRC Press, Taylor and Francis Group: New York, 2015.

3. Reichstein, M.; Bahn, M.; Ciais, P.; Frank, D.; Mahecha, M. D.; Seneviratne, S. I.; Zscheischler, J.; Beer, C.; Buchmann, N.; Frank, D. C.; Papale, D.; Rammig, A.; Smith, P. Climate extremes and the carbon cycle. *Nature* **2013**, *500*, 287–295.

4. Heimann, M.; Reichstein, M. Terrestrial ecosystem carbon dynamics and climate feedbacks. *Nature* **2008**, *451*, 289–292.

5. Ciais, P.; Sabine, C.; Bala, G.; Bopp, L.; Brovkin, V.; Canadell, J.; Chhabra, A.; DeFries, R.; Galloway, J.; Heimann, M.; Jones, C.; Le Quéré, C.; Myneni, R. B.; Piao, S. L.; Thornton, P. Carbon and Other Biogeochemical Cycles. In *Climate Change 2013: The Physical Science Basis. Contribution of Working Group I to the Fifth Assessment Report of the Intergovernmental Panel on Climate Change*; Stocker, T.F. D. Qin, G.-K. Plattner, M. Tignor, S.K. Allen, J. Boschung, A. Nauels, Y. Xia, V. B. and P. M. M., Ed.; Cambridge University Press: Cambridge, UK and New York, USA, 2013.

6. Frank, D.; Reichstein, M.; Bahn, M.; Thonicke, K.; Frank, D.; Mahecha, M. D.; Smith, P.; van der Velde, M.; Vicca, S.; Babst, F.; Beer, C.; Buchmann, N.; Canadell, J. G.; Ciais, P.; Cramer, W.; Ibrom, A.; Miglietta, F.; Poulter, B.; Rammig, A.; Seneviratne, S. I.; Walz, A.; Wattenbach, M.; Zavala, M. A.; Zscheischler, J. Effects of climate extremes on the terrestrial carbon cycle: Concepts, processes and potential future impacts. *Glob. Chang. Biol.* **2015**, *21*, 2861–2880.

7. Trumper, K.; Bertzky, M.; Dickson, B.; van der Heijden, G.; Jenkins, M.; Manning, P. *The Natural Fix? The role of ecosystems in climate mitigation. A UNEP rapid response assessment.*; United Nations Environment Programme, UNEP- WCMC: Cambridge, UK, 2009.

8. Le Quéré, C.; Raupach, M. R.; Canadell, J. G.; Marland, G.; Bopp, L.; Ciais, P.; Conway, T. J.; Doney, S. C.; Feely, R. A.; Foster, P.; Friedlingstein, P.; Gurney, K.; Houghton, R. A.; House, J. I.; Huntingford, C.; Levy, P. E.; Lomas, M. R.; Majkut, J.; Metzl, N.; Ometto, J. P.; Peters, G. P.; Prentice, I. C.; Randerson, J. T.; Running, S. W.; Sarmiento, J. L.; Schuster, U.; Sitch, S.; Takahashi, T.; Viovy, N.; van der Werf, G. R.; Woodward, F. I. Trends in the sources and sinks of carbon dioxide. *Nat. Geosci.* **2009**, *2*, 831–836.

9. Amundson, R. The carbon budget in soils. *Annu. Rev. Earth Planet Sci.* **2001**, *29*, 535–562.

10. Janssens, I. A.; Freibauer, A.; Ciais, P.; Smith, P.; Nabuurs, G.; Folberth, G.; Schlamadinger, B.; Hutjes, R. W. A.; Ceulemans, R.; Schulze, E.; Valentini, R.; Dolman, A. J. Europe ' s Terrestrial Biosphere Anthropogenic CO 2 Emissions. *Science (80-.).* **2003**, *300*, 1538–1542.

11. J. G. Canadell; M. R. Raupach Managing Forests for Climate Change Mitigation. *Science (80-.).* **2008**, *320*, 1456–1458.

12. Howden, S. M.; Crimp, S. J.; Stokes, C. J. Climate change and Australian livestock systems: Impacts, research and policy issues. *Aust. J. Exp. Agric.* **2008**, *48*, 780–788.

13. Wohlfahrt, G.; Fenstermaker, L. F.; Arnone Iii, J. A. Large annual net ecosystem CO2 uptake of a Mojave Desert ecosystem. *Glob. Chang. Biol.* **2008**, *14*, 1475–1487.

14. Ahlström, A.; Raupach, M. R.; Guy Schurgers; Smith, B.; Arneth, A.; Jung, M.; Reichstein, M.; Canadell, J.; Friedlingstein, P.; Jain, A. K.; Kato, E.; Poulter, B.; Sitch, S.; Stocker, B. D.; Zeng, N. The dominant role of semi-arid ecosystems in the trend and variability of the land CO2 sink. *Science (80-.).* **2015**, *348*, 895–899.

15. Lewis, S. L.; Lopez-Gonzalez, G.; Sonke, B.; Affum-Baffoe, K.; Baker, T. R.; Ojo, L. O.; Phillips, O. L.; Reitsma, J. M.; White, L.; Comiskey, J. A.; Djuikouo, K. M.; Ewango, C. E.; Feldpausch, T. R.; Hamilton, A. C.; Gloor, M.; Hart, T.; Hladik, A.; Lloyd, J.; Lovett, J. C.; Makana, J. R.; Malhi, Y.; Mbago, F. M.; Ndangalasi, H. J.; Peacock, J.; Peh, K. S.; Sheil, D.; Sunderland, T.; Swaine, M. D.; Taplin, J.; Taylor, D.; Thomas, S. C.; Votere, R.; Woll, H. Increasing carbon storage in intact African tropical forests. *Nature* **2009**, *457*, 1003–1006.

16. Nepstad, D. C.; Tohver, I. M.; Ray, D.; Moutinho, P.; Cardinot, G. Mortality of Large Trees and Lianas following Experimental Drought in an Amazon Forest. *Ecology* **2007**, *88*, 2259–2269.

17. Phillips, O. L.; Aragão, L. E. O. C.; Lewis, S. L.; Fisher, J. B.; Lloyd, J.; López-González, G.; Malhi, Y.; Monteagudo, A.; Peacock, J.; Quesada, C. a; van der Heijden, G.; Almeida, S.; Amaral, I.; Arroyo, L.; Aymard, G.; Baker, T. R.; Bánki, O.; Blanc, L.; Bonal, D.; Brando, P.; Chave, J.; de Oliveira, A. C. A.; Cardozo, N. D.; Czimczik, C. I.; Feldpausch, T. R.; Freitas, M. A.; Gloor, E.; Higuchi, N.; Jiménez, E.; Lloyd, G.; Meir, P.; Mendoza, C.; Morel, A.; Neill, D. a; Nepstad, D.; Patiño, S.; Peñuela, M. C.; Prieto, A.; Ramírez, F.; Schwarz, M.; Silva, J.; Silveira, M.; Thomas, A. S.; Steege, H. Ter; Stropp, J.; Vásquez, R.; Zelazowski, P.; Alvarez Dávila, E.; Andelman, S.; Andrade, A.; Chao, K.; Erwin, T.; Di Fiore, A.; Honorio C, E.; Keeling, H.; Killeen, T. J.; Laurance, W. F.; Peña Cruz, A.; Pitman, N. C. a; Núñez Vargas, P.; Ramírez-Angulo, H.; Rudas, A.; Salamão,

R.; Silva, N.; Terborgh, J.; Torres-Lezama, A.; Heijden, G. Van Der; Cristina, Á.; Oliveira, A. De; Dávila, E. A.; Fiore, A. Di; C, E. H.; Cruz, A. P.; Vargas, P. N. Drought Sensitivity of the Amazon Rainforest. *Science (80-.).* **2009**, *323*, 1344–1347.

18. Canadell, J. G.; Le Quéré, C.; Raupach, M. R.; Field, C. B.; Buitenhuis, E. T.; Ciais, P.; Conway, T. J.; Gillett, N. P.; Houghton, R. A.; Marland, G. Contributions to accelerating atmospheric CO2 growth from economic activity, carbon intensity, and efficiency of natural sinks. *Proc. Natl. Acad. Sci. U. S. A.* **2007**, *104*, 18866–70.

19. Rautiainen, M.; Heiskanen, J.; Eklundh, L.; MÕttus, M.; Lukeš, P.; Stenberg, P. Ecological applications of physically based remote sensing methods. *Scand. J. For. Res.* **2010**, *25*, 325–339.

20. Peñuelas, J.; Garbulsky, M. F.; Filella, I. Photochemical reflectance index (PRI) and remote sensing of plant CO2 uptake. *New Phytol.* **2011**, *191*, 596–599.

21. Song, C.; Dannenberg, M. P.; Hwang, T. Optical remote sensing of terrestrial ecosystem primary productivity. *Prog. Phys. Geogr.* **2013**, *37*, 834–854.

22. Chapin, F. S.; Matson, P. a; Mooney, H. a *Principles of Terrestrial Ecosystem Ecology*; 2002; Vol. 21.

23. Schimel, D. S. Terrestrial ecosystems and the carbon cycle. *Glob. Chang. Biol.* **1995**, 77–91.

24. Baldocchi, D. D. Assessing the eddy covariance technique for evaluating carbon dioxide exchange rates of ecosystems: Past, present and future. **2003**, 479–492.

25. Baldocchi, D.; Meyers, T. On using eco-phyiscal, micrometeorological and biogeochemical theory to evaluate carbon dioxide, water vapor and tracve gas fluxes over vegetation: a perspective. *Agric. an For. Meteorol.* **1998**, *90*, 1–25.

26. Aubinet, M.; Grelle, A.; Ibrom, A.; Rannik, U.; Moncrieff, J.; Foken, T.; Kowalski, A. S.; Martin, P. H.; Berbigier, P.; Bernhofer, C.; Clement, R.; Elbers, J.; Granier, A.; Grunwald, T.; Morgenstern, K.; Pilegaard, K.; Rebmann, C.; Snijders, W.; Valentini, R.; Vesala, T. Estimates of the annual net carbon and water exchange of forests: the EUROFLUX methodology. *Adv. Ecol. Res.* **2000**, *30*, 113–175.

27. Aubinet, M., Clement, R., Elbers, J. A., Foken, T., Grelle, A., Ibrom, A., Moncrieff, J., Pilegaard, K., Rannik, U., Rebmann, C. Methodology for Data Acquisition, Storage and Treatment. In *Fluxes of carbon, Water and Energy of European Forests*; Valentini, R., Ed.; Springer-Verlag: Berlin, Germany, 2003.

28. Papale, D.; Reichstein, M.; Aubinet, M.; Canfora, E.; Bernhofer, C.; Kutsch, W.; Longdoz, B.; Rambal, S.; Valentini, R.; Vesala, T.; Yakir, D. Towards a standardized processing of Net Ecosystem Exchange measured with eddy covariance technique: algorithms and uncertainty estimation. *Biogeosciences* **2006**, *3*, 571–583.

29. Homolová, L.; Malenovský, Z.; Clevers, J. G. P. W.; García-Santos, G.; Schaepman, M. E. Review of optical-based remote sensing for plant trait mapping. *Ecol. Complex.* **2013**, *15*, 1–16.

30. Lanfri, S. *Vegetation analysis using remote sensing*; Cordoba National University (UNC): Cordoba, Argentina, 2010.

31. Ustin, S. L.; Gitelson, A. A.; Jacquemoud, S.; Schaepman, M.; Asner, G. P.; Gamon, J. A.; Zarco-Tejada, P. Retrieval of foliar information about plant pigment systems from high resolution spectroscopy. *Remote Sens. Environ.* **2009**, *113*, S67–S77.

32. Kokaly, R. F.; Asner, G. P.; Ollinger, S. V.; Martin, M. E.; Wessman, C. A. Characterizing canopy biochemistry from imaging spectroscopy and its application to ecosystem studies. *Remote Sens. Environ.* **2009**, *113*, S78–S91.

33. Jensen, J. R. *Remote Sensing of the Environment: An Earth Resource Perspective*; Pearson Prentice Hall: Upper Saddle River, New Jersey, 2000.

34. Sahoo, R. N.; Ray, S. S.; Manjunath, K. R. Hyperspectral remote sensing of agriculture. *Curr. Sci.* **2015**, *108*.

35. Gitelson, A. a; Zur, Y.; Chivkunova, O. B.; Merzlyak, M. N. Assessing carotenoid content in plant leaves with reflectance spectroscopy. *Photochem. Photobiol.* **2002**, *75*, 272–281.

36. Asner, G. P. Biophysical and Biochemical Sources of Variability in Canopy Reflectance. *Remote Sens. Environ.* **1998**, *64*, 234–253.

37. Guyot, G. Optical properties of vegetation canopies. In *Applications of Remote Sensing in Agriculture*; Steven, M. D.; Clark, J. A., Eds.; Butterworths: London, UK, 1990; pp. 19–43.

38. Lichtenthaler, H. K.; Gitelson, A.; Lang, M. Non-Destructive Determination of Chlorophyll Content of Leaves of a Green and an Aurea Mutant of Tobacco by Reflectance Measurements. *J. Plant Physiol.* **1996**, *148*, 483–493.

39. Zhang, F.; Zhou, G. Estimation of Canopy Water Content by Means of Hyperspectral Indices Based on Drought Stress Gradient Experiments of Maize in the North Plain China. *Remote Sens.* **2015**, *7*, 15203–15223.

40. Horler, D. N. H.; Dockray, M.; Barber, J.; Barringer, A. R. Red edge measurements for remotely sensing plant chlorophyll content. *Adv. Sp. Res.* **1983**, *3*, 273–277.

41. Bannari, A.; Morin, D.; Bonn, F.; Huete, A. R. A review of vegetation indices. *Remote Sens. Rev.* **1995**, *13*, 95–120.

42. Delegido, J.; Verrelst, J.; Meza, C. M.; Rivera, J. P.; Alonso, L.; Moreno, J. A red-edge spectral index for remote sensing estimation of green LAI over agroecosystems. *Eur. J. Agron.* **2013**, *46*, 42–52.

43. Rouse, J. W.; Haas, R. H.; Schell, J. A.; Deering, D. W. Monitoring vegetation systems in the Great Plains with ERTS. In *Third Earth Resources Technology Satellite-1 Symposium*; NASA: Washington, DC, USA, 1974; pp. 309–317.

44. Baret, F.; Guyot, G. Potentials and limits of vegetation indices for LAI and APAR assessment. *Remote Sens. Environ.* **1991**, *35*, 161–173.

45. Myneni, R. B., Hall, F. G., Sellers, P. J., Marshak, A. L. The Interpretation of Spectral Vegetation Indexes. *Ieee T. Geosci. Remote* **1995**, *33*, 481–486.

46. Gitelson, A. a; Gritz, Y.; Merzlyak, M. N. Relationships between leaf chlorophyll content and spectral reflectance and algorithms for non-destructive chlorophyll assessment in higher plant leaves. *J. Plant Physiol.* **2003**, *160*, 271–282.

47. Clevers, J. G. P. W.; Gitelson, A. Remote estimation of crop and grass chlorophyll and nitrogen content using red-edge bands on Sentinel-2 and -3. *Int. J. Appl. Earth Obs. Geoinf.* **2013**, *23*, 344–351.

48. Balzarolo, M.; Anderson, K.; Nichol, C.; Rossini, M.; Vescovo, L.; Arriga, N.; Wohlfahrt, G.; Calvet, J. C.; Carrara, A.; Cerasoli, S.; Cogliati, S.; Daumard, F.; Eklundh, L.; Elbers, J. a.; Evrendilek, F.; Handcock, R. N.; Kaduk, J.; Klumpp, K.; Longdoz, B.; Matteucci, G.; Meroni, M.; Montagnani, L.; Ourcival, J. M.; Sánchez-Cañete, E. P.; Pontailler, J. Y.; Juszczak, R.; Scholes, B.; Pilar Martín, M. Ground-based optical measurements at European flux sites: A review of methods, instruments and current controversies. *Sensors* **2011**, *11*, 7954–7981.

49. Govender, M.; Chetty, K.; Bulcock, H. A review of hyperspectral remote sensing and its application in vegetation and water resource studies. *Water SA* **2006**, *33*, 145–152.

50. Gamon, J. a.; Kovalchuck, O.; Wong, C. Y. S.; Harris, a.; Garrity, S. R. Monitoring seasonal and diurnal changes in photosynthetic pigments with automated PRI and NDVI sensors. *Biogeosciences*

2015, *12*, 4149–4159.

51. Lillesand, T. M.; Kiefer, R. W. *Remote Sensing and Image Analysis*; John Wiley and Sons: New York, 1979; Vol. 46.

52. Gullino, M. L.; Bonants, P. J. M. Detection and Diagnostics of Plant Pathogens. In *Plant Pathology in the 21st Century*; Springer Verlag: New York, 2014; pp. 1–200.

53. Hoffman, R. R.; Markman, A. B. *Interpreting Remote Sensing Imagery: Human Factors*; CRC Press, Taylor and Francis Group, 2001.

54. Long, S. P.; Farage, P. K.; Garcia, R. L. Measurement of leaf and canopy photosynthetic CO2 exchange in the field. *J. Exp. Bot.* **1996**, *47*, 1629–1642.

55. Long, S. P.; Bernacchi, C. J. Gas exchange measurements, what can they tell us about the underlying limitations to photosynthesis? Procedures and sources of error. *J. Exp. Bot.* **2003**, *54*, 2393–2401.

56. Bernacchi, C.; Diaz-Espejo, A.; Flexas, J. Gas-exchange analysis: basics and problemGas-exchange analysis: basics and problemss. In *Terrestrial Photosynthesis in a Changing Environment A Molecular, Physiological and Ecological Approach*; Flexas, J.; Loreto, F.; Medrano, H., Eds.; Cambridge University Press: Cambridge, UK, 2012; pp. 1–728.

57. Butler, W. L. Energy Distribution in the Photochemical Apparatus of Photosynthesis. *Annu. Rev. Plant Physiol.* **1978**, *29*, 345–378.

58. Murchie, E. H.; Lawson, T. Chlorophyll fluorescence analysis: A guide to good practice and understanding some new applications. *J. Exp. Bot.* 2013, *64*, 3983–3998.

59. Baker, N. R. Chlorophyll Fluorescence: A Probe of Photosynthesis In Vivo. *Annu. Rev. Plant Biol* **2008**, *59*, 89–113.

60. Bolhàr-Nordenkampf, H. R.; Long, S. P.; Baker, N. R.; Oquist, G.; Schreiber, U.; Lechner, E. G. Chlorophyll fluorescence as a probe of the photosynthetic competence of leaves in the field: A review of current instrumentation. *Funct. Ecol.* **1989**, *3*, 497–514.

61. Porcar-Castell, A.; Tyystjärvi, E.; Atherton, J.; Van Der Tol, C.; Flexas, J.; Pfündel, E. E.; Moreno, J.; Frankenberg, C.; Berry, J. A. Linking chlorophyll a fluorescence to photosynthesis for remote sensing applications: mechanisms and challenges. *J. Exp. Bot.* **2014**, *65*, 4065–4095.

62. Damm, A.; Elbers, J.; Erler, A.; Gioli, B.; Hamdi, K.; Hutjes, R.; Kosvancova, M.; Meroni, M.;

Miglietta, F.; Moersch, A.; Moreno, J.; Schickling, A.; Sonnenschein, R.; Udelhoven, T.; Van Der LINDEN, S.; Hostert, P.; Rascher, U. Remote sensing of sun-induced fluorescence to improve modeling of diurnal courses of gross primary production (GPP). *Glob. Chang. Biol.* **2010**, *16*, 171–186.

63. Gitelson, A. a.; Gamon, J. a. The need for a common basis for defining light-use efficiency: Implications for productivity estimation. *Remote Sens. Environ.* **2015**, *156*, 196–201.

64. Tubuxin, B.; Rahimzadeh-Bajgiran, P.; Ginnan, Y.; Hosoi, F.; Omasa, K. Estimating chlorophyll content and photochemical yield of photosystem II (Φ_{PSII}) using solar-induced chlorophyll fluorescence measurements at different growing stages of attached leaves. *J. Exp. Bot.* **2015**, *66*, 5595–5603.

65. Damm, a.; Guanter, L.; Paul-Limoges, E.; van der Tol, C.; Hueni, a.; Buchmann, N.; Eugster, W.; Ammann, C.; Schaepman, M. E. Far-red sun-induced chlorophyll fluorescence shows ecosystem-specific relationships to gross primary production: An assessment based on observational and modeling approaches. *Remote Sens. Environ.* **2015**, *166*, 91–105.

66. Glenn, E. P.; Huete, A. R.; Nagler, P. L.; Nelson, S. G. Relationship between remotely-sensed vegetation indices, canopy attributes and plant physiological processes: What vegetation indices can and cannot tell us about the landscape. *Sensors* **2008**, *8*, 2136–2160.

67. Schmid, H. P. Footprint modeling for vegetation atmosphere exchange studies: A review and perspective. *Agric. For. Meteorol.* **2002**, *113*, 159–183.

68. Schimel, D.; Pavlick, R.; Fisher, J. B.; Asner, G. P.; Saatchi, S.; Townsend, P.; Miller, C.; Frankenberg, C.; Hibbard, K.; Cox, P. Observing terrestrial ecosystems and the carbon cycle from space. *Glob. Chang. Biol.* **2015**, *21*, 1762–1776.

69. Gamon, J. a.; Rahman, a. F.; Dungan, J. L.; Schildhauer, M.; Huemmrich, K. F. Spectral Network (SpecNet)-What is it and why do we need it? *Remote Sens. Environ.* **2006**, *103*, 227–235.

70. Porcar-Castell, A.; Mac Arthur, A.; Rossini, M.; Eklundh, L.; Pacheco-Labrador, J.; Anderson, K.; Balzarolo, M.; Martín, M. P.; Jin, H.; Tomelleri, E.; Cerasoli, S.; Sakowska, K.; Hueni, A.; Julitta, T.; Nichol, C. J.; Vescovo, L. EUROSPEC: at the interface between remote-sensing and ecosystem CO2 flux measurements in Europe. *Biogeosciences* **2015**, *12*, 6103–6124.

71. Gamon, J. a. Reviews and Syntheses: optical sampling of the flux tower footprint. *Biogeosciences* **2015**, *12*, 4509–4523.

72. Heinsch, F. A.; Zhao, M.; Running, S. W.; Kimball, J. S.; Nemani, R. R.; Davis, K. J.; Bolstad, P. V.; Cook, B. D.; Desai, A. R.; Ricciuto, D. M.; Law, B. E.; Oechel, W. C.; Kwon, H.; Luo, H.; Wofsy, S. C.; Dunn, A. L.; Munger, J. W.; Baldocchi, D. D.; Xu, L.; Hollinger, D. Y.; Richardson, A. D.; Stoy, P. C.; Siqueira, M. B. S.; Monson, R. K.; Burns, S. P.; Flanagan, L. B. Evaluation of remote sensing based terrestrial productivity from MODIS using regional tower eddy flux network observations. *IEEE Trans. Geosci. Remote Sens.* **2006**, *44*, 1908–1923.

73. Ueyama, M.; Ichii, K.; Iwata, H.; Euskirchen, E. S.; Zona, D.; Rocha, A. V.; Harazono, Y.; Iwama, C.; Nakai, T.; Oechel, W. C. Upscaling terrestrial carbon dioxide fluxes in Alaska with satellite remote sensing and support vector regression. *J. Geophys. Res. Biogeosciences* **2013**, *118*, 1266–1281.

74. Cogliati, S.; Rossini, M.; Julitta, T.; Meroni, M.; Schickling, A.; Burkart, A.; Pinto, F.; Rascher, U.; Colombo, R. Continuous and long-term measurements of reflectance and sun-induced chlorophyll fluorescence by using novel automated field spectroscopy systems. *Remote Sens. Environ.* **2015**, *164*.

75. Monteith, J. L. Solar radiation and productivity in tropical ecosystems. *J. Appl. Ecol.* **1972**, *9*, 747–766.

76. Running, S. W. Climate change. Ecosystem disturbance, carbon, and climate. *Science* **2008**, *321*, 652–653.

77. Fang, C.; Moncrieff, J. B. The dependence of soil CO2 efflux on temperature. *Soil Biol. Biochem.* **2001**, *33*, 155–165.

78. Lynch, D. H.; Cohen, R. D. H.; Fredeen, a.; Patterson, G.; Martin, R. C. Management of Canadian prairie region grazed grasslands: Soil C sequestration, livestock productivity and profitability. *Can. J. Soil Sci.* **2005**, *85*, 183–192.

79. Bonan, G. B. Forests and climate change: forcings, feedbacks, and the climate benefits of forests. *Science (80-.).* **2008**, *320*, 1444–1449.

80. Friedel M. H., Laycock W. A., B. G. N. Assessing rangeland condition and trend. In *Field and laboratory Methods for Grassland and Animal Production Research*; ‘t Mannetje L. and Jones R. M., Ed.; Wallingford, UK, 2000; pp. 227–262.

81. Adams, B. W.; Ehlert, G.; Stone, C.; Lawrence, D.; Alexander, M.; Willoughby; Hincz, C.; Moisey, D.; Burkinshaw, A.; Carlson, J. *Rangeland Health Assessment for Grassland, Forest, And Tame Pasture*; Alberta Sustainable Resource Development, Public Lands Division, R. M. B., Ed.; Edmonton, Alberta, Canada, 2009.

82. Allen, V. G.; Batello, C.; Berretta, E. J.; Hodgson, J.; Kothmann, M.; Li, X.; McIvor, J.; Milne, J.; Morris, C.; Peeters, a.; Sanderson, M. An international terminology for grazing lands and grazing animals. *Grass Forage Sci.* **2011**, *66*, 2–28.

83. Downing, D. J. *Natural Regions and Subregions of Alberta*; Natural Regions Commitee. Governement of Alberta, 2006.

84. Adams, B. W.; Richman, J.; Poulin-Klein, L.; France, K.; Moisey, D.; McNeil, R. L. *Rangeland Plant Communities for the Dry Mixedgrass Natural Subregion of Alberta*; Rangeland Management Branch, Policy Division, A. E. and S. R. D., Ed.; Lethbridge, 2013.

85. Conant, R. T. *Challenges and opportunities for carbon sequestration in grassland systems*; 2010; Vol. 9.

86. Solomon, A. M.; Prentice, I. C.; Leemans, R.; Cramer, W. The interaction of climate and land use in future terrestrial carbon storage and release. *Water, Air Soil Pollut.* **1993**, *70*, 595–614.

87. Wehlage, D. C. Monitoring year-to-year variability in dry mixed-grass prairie yield using multi-sensor remote sensing, University of Alberta, 2012.

88. Frank, D. a. Drought effects on above- and belowground production of a grazed temperate grassland ecosystem. *Oecologia* **2007**, *152*, 131–139.

89. Hovenden, M. J.; Newton, P. C. D.; Wills, K. E. Seasonal not annual rainfall determines grassland biomass response to carbon dioxide. *Nature* **2014**, *511*, 583–586.

90. Brookshire, E. N. J.; Weaver, T. Long-term decline in grassland productivity driven by increasing dryness. *Nat. Commun.* **2015**, *6*, 7148.

91. Stohlgren, T. J.; Bull, K. a; Otsuki, Y. Comparison of rangeland vegetation sampling techniques in the Central Grasslands. *J. range Manag.* **1998**, *51*, 164–172.

92. Lieth, H. Modeling the primary productivity of the world. In *Primary Productivity of the Biosphere*; Lieth, H.; Whittaker, R. H., Eds.; Springer Verlag: Berlin, 1975; Vol. 14, p. 339.

93. Wu, C.; Munger, J. W.; Niu, Z.; Kuang, D. Comparison of multiple models for estimating gross primary production using MODIS and eddy covariance data in Harvard Forest. *Remote Sens. Environ.* **2010**, *114*, 2925–2939.

94. Schimel, D. S.; Braswell, B. H.; Holland, E. a.; McKeown, R.; Ojima, D. S.; Painter, T. H.; Parton, W. J.; Townsend, A. R. Climatic, edaphic, and biotic controls over storage and turnover of carbon in

soils. *Global Biogeochem. Cycles* **1994**, *8*, 279.

95. Ramoelo, A.; Skidmore, A. K.; Schlerf, M.; Heitkönig, I. M. a; Mathieu, R.; Cho, M. a. Savanna grass nitrogen to phosphorous ratio estimation using field spectroscopy and the potential for estimation with imaging spectroscopy. *Int. J. Appl. Earth Obs. Geoinf.* **2013**, *23*, 334–343.

96. Baldocchi, D.D., Hincks, B.B., Meyers, T. P. Measuring Biosphere-Atmosphere Exchanges of Biologically Related Gases with Micrometeorological Methods. *Ecology* **1988**, *69*, 1331–1340.

97. Valentini, R., Gamon, J., Field, C. Ecosystem Gas Exchange in a California Grassland : Seasonal Patterns and Implications for Scaling. *Ecology* **1995**, *76*, 1940–1952.

98. Soussana, J. F.; Allard, V.; Pilegaard, K.; Ambus, P.; Amman, C.; Campbell, C.; Ceschia, E.; Clifton-Brown, J.; Czobel, S.; Domingues, R.; Flechard, C.; Fuhrer, J.; Hensen, A.; Horvath, L.; Jones, M.; Kasper, G.; Martin, C.; Nagy, Z.; Neftel, A.; Raschi, A.; Baronti, S.; Rees, R. M.; Skiba, U.; Stefani, P.; Manca, G.; Sutton, M.; Tuba, Z.; Valentini, R. Full accounting of the greenhouse gas (CO2, N2O, CH4) budget of nine European grassland sites. *Agric. Ecosyst. Environ.* **2007**, *121*, 121–134.

99. Running, S. W.; Nemani, R. R.; Heinsch, F. A.; Zhao, M.; Reeves, M.; Hashimoto, H. A Continuous Satellite-Derived Measure of Global Terrestrial Primary Production. *Bioscience* **2004**, *54*, 547–560.

100. Huemmrich, K. F.; Gamon, J. a.; Tweedie, C. E.; Campbell, P. K. E.; Landis, D. R.; Middleton, E. M. Arctic tundra vegetation functional types based on photosynthetic physiology and optical properties. *IEEE J. Sel. Top. Appl. Earth Obs. Remote Sens.* **2013**, *6*, 265–275.

101. Gamon, J. a.; Coburn, C.; Flanagan, L. B.; Huemmrich, K. F.; Kiddle, C.; Sanchez-Azofeifa, G. a.; Thayer, D. R.; Vescovo, L.; Gianelle, D.; Sims, D. a.; Rahman, a. F.; Pastorello, G. Z. SpecNet revisited: Bridging flux and remote sensing communities. *Can. J. Remote Sens.* **2010**, *36*.

102. Monteith, J. L. Climate and the efficiency of crop production in Britain. *Philos. Trans. R. Soc. B Biol. Sci.* **1977**, *281*, 277–294.

103. Rossini, M.; Meroni, M.; Migliavacca, M.; Manca, G.; Cogliati, S.; Busetto, L.; Picchi, V.; Cescatti, A.; Seufert, G.; Colombo, R. High resolution field spectroscopy measurements for estimating gross ecosystem production in a rice field. *Agric. For. Meteorol.* **2010**, *150*, 1283–1296.

104. Lobell, D. B.; Asner, G. P.; Ortiz-Monasterio, J. I.; Benning, T. L. Remote sensing of regional crop production in the Yaqui Valley, Mexico: Estimates and uncertainties. *Agric. Ecosyst. Environ.*

2003, *94*, 205–220.

105. Hilker, T.; Coops, N. C.; Wulder, M. A.; Black, T. A.; Guy, R. D. The use of remote sensing in light use efficiency based models of gross primary production: A review of current status and future requirements. *Sci. Total Environ.* **2008**, *404*, 411–423.

106. Myneni, R. B.; Williams, D. L. On the relationship between FAPAR and NDVI. *Remote Sens. Environ.* **1994**, *49*, 200–211.

107. Becker, S. *Mattheis Ranch vegetation and soil inventory*; Rangelands Research Institute. University of Alberta, 2013.

108. Huemmrich, K. F.; Black, T. a.; Jarvis, P. G.; McCaughey, J. H.; Hall, F. G. High temporal resolution NDVI phenology from micrometeorological radiation sensors. *J. Geophys. Res.* **1999**, *104*, 27935.

109. Gamon, J. a.; Cheng, Y.; Claudio, H.; MacKinney, L.; Sims, D. a. A mobile tram system for systematic sampling of ecosystem optical properties. *Remote Sens. Environ.* **2006**, *103*, 246–254.

110. Webb, E. K., Pearman, G. I., Leuning, R. Correction of flux measurements for density effects due to heat and water-vapor transfer. *Q. J. R. Meteorol. Soc.* **1980**, *106*, 85–100.

111. Moncrieff, J., Clement, R., Finnigan, J. J., and Meyers, T. Averaging, detrending, and filtering of eddy covariance time series. In *Handbook of Micrometeorology: A Guide for Surface Flux Measurement and Analysis*; Springer Netherlands, 2005; pp. 7–31.

112. Ibrom, A.; Dellwik, E.; Flyvbjerg, H.; Jensen, N. O.; Pilegaard, K. Strong low-pass filtering effects on water vapour flux measurements with closed-path eddy correlation systems. *Agric. For. Meteorol.* **2007**, *147*, 140–156.

113. Wille, C.; Kutzbach, L.; Sachs, T.; Wagner, D.; Pfeiffer, E. M. Methane emission from Siberian arctic polygonal tundra: Eddy covariance measurements and modeling. *Glob. Chang. Biol.* **2008**, *14*, 1395–1408.

114. Mauder, M.; Foken, T. Impact of post-field data processing on eddy covariance flux estimates and energy balance closure. *Meteorol. Zeitschrift* **2006**, *15*, 597–609.

115. Cheng, Y.; Gamon, J. a.; Fuentes, D. a.; Mao, Z.; Sims, D. a.; Qiu, H. L.; Claudio, H.; Huete, A.; Rahman, A. F. A multi-scale analysis of dynamic optical signals in a Southern California chaparral ecosystem: A comparison of field, AVIRIS and MODIS data. *Remote Sens. Environ.* **2006**, *103*, 369–378.

116. Falge, E.; Baldocchi, D.; Tenhunen, J.; Aubinet, M.; Bakwin, P.; Berbigier, P.; Bernhofer, C.; Burba, G.; Clement, R.; Davis, K. J.; Elbers, J. a.; Goldstein, A. H.; Grelle, A.; Granier, A.; Gumundsson, J.; Hollinger, D.; Kowalski, A. S.; Katul, G.; Law, B. E.; Malhi, Y.; Meyers, T.; Monson, R. K.; Munger, J. W.; Oechel, W.; Paw U, K. T.; Pilegaard, K.; Rannik, Ü.; Rebmann, C.; Suyker, A.; Valentini, R.; Wilson, K.; Wofsy, S. Seasonality of ecosystem respiration and gross primary production as derived from FLUXNET measurements. *Agric. For. Meteorol.* **2001**, *113*, 53–74.

117. Moffat, A. M.; Papale, D.; Reichstein, M.; Hollinger, D. Y.; Richardson, A. D.; Barr, A. G.; Beckstein, C.; Braswell, B. H.; Churkina, G.; Desai, A. R.; Falge, E.; Gove, J. H.; Heimann, M.; Hui, D.; Jarvis, A. J.; Kattge, J.; Noormets, A.; Stauch, V. J. Comprehensive comparison of gap-filling techniques for eddy covariance net carbon fluxes. *Agric. For. Meteorol.* **2007**, *147*, 209–232.

118. Wohlfahrt, G.; Pilloni, S.; Hörtnagl, L.; Hammerle, A. Estimating carbon dioxide fluxes from temperate mountain grasslands using broad-band vegetation indices. *Biogeosciences* **2010**, *7*, 683–694.

119. Running, S. W. Estimating terrestrial primary productivity by combining remote sensing and ecosystem simulation. In *Remote Sensing of Biosphere Functioning*; Hobbs, R. J., Mooney, H. A., Ed.; Springer-Verlag: New York, 1990.

120. Gamon, J. A.; Field, C. B.; Goulden, M. L.; Griffin, K. L.; Hartley, A. E.; Joel, G.; Peñuelas, J.; Valentini, R. Relationships Between NDVI , Canopy Structure , and Photosynthesis in Three Californian Vegetation Types. *Ecol. Appl.* **1995**, *5*, 28–41.

121. Pettorelli, N.; Vik, J. O.; Mysterud, A.; Gaillard, J. M.; Tucker, C. J.; Stenseth, N. C. Using the satellite-derived NDVI to assess ecological responses to environmental change. *Trends Ecol. Evol.* **2005**, *20*, 503–510.

122. Gamon, J. a.; Huemmrich, K. F.; Stone, R. S.; Tweedie, C. E. Spatial and temporal variation in primary productivity (NDVI) of coastal Alaskan tundra: Decreased vegetation growth following earlier snowmelt. *Remote Sens. Environ.* **2013**, *129*, 144–153.

123. Peng, Y.; Gitelson, A. a.; Keydan, G.; Rundquist, D. C.; Moses, W. Remote estimation of gross primary production in maize and support for a new paradigm based on total crop chlorophyll content. *Remote Sens. Environ.* **2011**, *115*, 978–989.

124. Rossini, M.; Cogliati, S.; Meroni, M.; Migliavacca, M.; Galvagno, M.; Busetto, L.; Cremonese, E.; Julitta, T.; Siniscalco, C.; Morra Di Cella, U.; Colombo, R. Remote sensing-based estimation of

gross primary production in a subalpine grassland. *Biogeosciences* **2012**, *9*, 2565–2584.

125. Gitelson, A. A., Peng, Y., Arkebauer, T. J., Schepers, J. Relationships between gross primary production, green LAI, and canopy chlorophyll content in maize: Implications for remote sensing of primary production. *Remote Sens. Environ.* **2014**, *144*, 65–72.

126. Gamon, J. A., Field, C. B. Roberts, D. A., Ustin, S. L., Valentini, R. Functional patterns in an annual grassland during an AVIRIS overflight. *Remote Sens. Environ.* **1993**, *44*, 239–253.

127. Balzarolo, M.; Vescovo, L.; Hammerle, a.; Gianelle, D.; Papale, D.; Wohlfahrt, G. On the relationship between ecosystem-scale hyperspectral reflectance and CO_2 exchange in European mountain grasslands. *Biogeosciences Discuss.* **2014**, *11*, 10323–10363.

128. Sakowska, K.; Vescovo, L.; Marcolla, B.; Juszczak, R.; Olejnik, J.; Gianelle, D. Review_Monitoring of carbon dioxide fluxes in a subalpine grassland ecosystem of the Italian Alps using a multispectral sensor. *Biogeosciences* **2014**, *11*, 4695–4712.

129. Field, C. B.; Randerson, J. T.; Malmström, C. M. Global net primary production: Combining ecology and remote sensing. *Remote Sens. Environ.* **1995**, *51*, 74–88.

130. Zhang, Q.; Cheng, Y.-B.; Lyapustin, A. I.; Wang, Y.; Zhang, X.; Suyker, A.; Verma, S.; Shuai, Y.; Middleton, E. M. Estimation of crop gross primary production (GPP): II. Do scaled MODIS vegetation indices improve performance? *Agric. For. Meteorol.* **2015**, *200*, 1–8.

131. Turner, D. P.; Ritts, W. D.; Cohen, W. B.; Maeirsperger, T. K.; Gower, S. T.; Kirschbaum, A. a.; Running, S. W.; Zhao, M.; Wofsy, S. C.; Dunn, A. L.; Law, B. E.; Campbell, J. L.; Oechel, W. C.; Kwon, H. J.; Meyers, T. P.; Small, E. E.; Kurc, S. a.; Gamon, J. a. Site-level evaluation of satellite-based global terrestrial gross primary production and net primary production monitoring. *Glob. Chang. Biol.* **2005**, *11*, 666–684.

132. Turner, D. P., Ritts, W. D., Cohen, W. B., Gower, S. T., Running, S. W., Zhao, M., Costa, M. H., Kirschbaum, A. A., Ham, J. M., Saleska, S. R., Ahl, D. E. Evaluation of MODIS NPP and GPP products across multiple biomes. *Remote Sens. Environ.* **2006**, *102*, 282–292.

133. Wu, C.; Niu, Z.; Tang, Q.; Huang, W.; Rivard, B.; Feng, J. Remote estimation of gross primary production in wheat using chlorophyll-related vegetation indices. *Agric. For. Meteorol.* **2009**, *149*, 1015–1021.

134. Ardö, J. Comparison between remote sensing and a dynamic vegetation model for estimating terrestrial primary production of Africa. *Carbon Balance Manag.* **2015**, *10*, 8.

135. Ruimy, a; Saugier, B. Methodology for the estimation of terrestrial net primary production from remotely sensed data. *J. Geophys. Res.* **1994**, *99*, 5263–5283.

136. Garbulsky, M. F.; Peñuelas, J.; Gamon, J.; Inoue, Y.; Filella, I. The photochemical reflectance index (PRI) and the remote sensing of leaf, canopy and ecosystem radiation use efficiencies. A review and meta-analysis. *Remote Sens. Environ.* **2011**, *115*, 281–297.

137. Gitelson, A. a.; Peng, Y.; Masek, J. G.; Rundquist, D. C.; Verma, S.; Suyker, A.; Baker, J. M.; Hatfield, J. L.; Meyers, T. Remote estimation of crop gross primary production with Landsat data. *Remote Sens. Environ.* **2012**, *121*, 404–414.

138. Garbulsky, M. F.; Peñuelas, J.; Papale, D.; Ardö, J.; Goulden, M. L.; Kiely, G.; Richardson, A. D.; Rotenberg, E.; Veenendaal, E. M.; Filella, I. Patterns and controls of the variability of radiation use efficiency and primary productivity across terrestrial ecosystems. *Glob. Ecol. Biogeogr.* **2010**, *19*, 253–267.

139. Gilmanov, T. G.; Baker, J. M.; Bernacchi, C. J.; Billesbach, D. P.; Burba, G. G.; Castro, S.; Chen, J.; Eugster, W.; Fischer, M. L.; Gamon, J. a.; Gebremedhin, M. T.; Glenn, A. J.; Griffis, T. J.; Hatfield, J. L.; Heuer, M. W.; Howard, D. M.; Leclerc, M. Y.; Loescher, H. W.; Marloie, O.; Meyers, T. P.; Olioso, A.; Phillips, R. L.; Prueger, J. H.; Skinner, R. H.; Suyker, A. E.; Tenuta, M.; Wylie, B. K. Productivity and Carbon Dioxide Exchange of Leguminous Crops: Estimates from Flux Tower Measurements. *Agron. J.* **2014**, *106*, 545.

140. Flanagan, L. B.; Sharp, E. J.; Gamon, J. A. Application of the photosynthetic light-use efficiency model in a northern Great Plains grassland. *Remote Sens. Environ.* **2015**, *168*, 239–251.

141. Hilker, T.; Nesic, Z.; Coops, N. C.; Lessard, D. a New, Automated, Multiangular Radiometer Instrument for Tower-Based Observations of Canopy Reflectance (Amspec Ii). *Instrum. Sci. Technol.* **2010**, *38*, 319–340.

142. Wang, R.; Gamon, J. A.; Emmerton, C. A.; Li, H.; Nestola, E.; Pastorello, G. Z.; Menzer, O. Integrated analysis of productivity and biodiversity in a southern Alberta prairie. *Remote Sensing(under Rev.*

143. Heath, J.; Kerstiens, G. Effects of elevated CO2 on leaf gas exchange in beech and oak at two levels of nutrient supply: Consequences for sensitivity to drought in beech. *Plant, Cell Environ.* **1997**, *20*, 57–68.

144. Dang, Q. L.; Margolis, H. A.; Coyea, M. R.; Sy, M.; Collatz, G. J. Regulation of branch-level gas exchange of boreal trees: roles of shoot water potential and vapor pressure difference. *Tree*

Physiol. **1997**, *17*, 521–535.

145. Scott, R. L.; Huxman, T. E.; Cable, W. L.; Emmerich, W. E. Partitioning of evapotranspiration and its relation to carbon dioxide exchange in a Chihuahuan Desert shrubland. *Hydrol. Process.* **2006**, *20*, 3227–3243.

146. Gower, S. T.; Kucharik, C. J.; Norman, J. M. Direct and indirect estimation of leaf area index, fAPAR, and net primary production of terrestrial ecosystems. *Remote Sens. Environ.* **1999**, *70*, 29–51.

147. Garbulsky, M. F.; Peñuelas, J.; Ogaya, R.; Filella, I. Leaf and stand-level carbon uptake of a Mediterranean forest estimated using the satellite-derived reflectance indices EVI and PRI. *Int. J. Remote Sens.* **2013**, *34*, 1282–1296.

148. Huemmrich, K. F.; Gamon, J. a.; Tweedie, C. E.; Oberbauer, S. F.; Kinoshita, G.; Houston, S.; Kuchy, a.; Hollister, R. D.; Kwon, H.; Mano, M.; Harazono, Y.; Webber, P. J.; Oechel, W. C. Remote sensing of tundra gross ecosystem productivity and light use efficiency under varying temperature and moisture conditions. *Remote Sens. Environ.* **2010**, *114*, 481–489.

149. Zarco-Tejada, P. J.; Morales, a; Testi, L.; Villalobos, F. J. Spatio-temporal patterns of chlorophyll fluorescence and physiological and structural indices acquired from hyperspectral imagery as compared with carbon fluxes measured with eddy covariance. *Remote Sens. Environ.* **2013**, *133*, 102–115.

150. Gianelle, D.; Vescovo, L.; Marcolla, B.; Manca, G.; Cescatti, a. Ecosystem carbon fluxes and canopy spectral reflectance of a mountain meadow. *Int. J. Remote Sens.* **2009**, *30*, 435–449.

151. Running, S. W.; Coughlan, J. C. A general model of forest ecosystem processes for regional applications I. Hydrologic balance, canopy gas exchange and primary production processes. *Ecol. Modell.* **1988**, *42*, 125–154.

152. Le Maire, G.; Davi, H.; Soudani, K.; François, C.; Le Dantec, V.; Dufrêne, E. Modeling annual production and carbon fluxes of a large managed temperate forest using forest inventories, satellite data and field measurements. *Tree Physiol.* **2005**, *25*, 859–872.

153. Coops, N. C.; Ferster, C. J.; Waring, R. H.; Nightingale, J. Comparison of three models for predicting gross primary production across and within forested ecoregions in the contiguous United States. *Remote Sens. Environ.* **2009**, *113*, 680–690.

154. Alton, P. B. Agricultural and Forest Meteorology The sensitivity of models of gross primary

productivity to meteorological and leaf area forcing : A comparison between a Penman – Monteith ecophysiological approach and the MODIS Light-Use Efficiency algorithm. *Agric. For. Meteorol.* **2016**, *218–219*, 11–24.

155. Maxwell, K.; Johnson, G. N. Chlorophyll fluorescence--a practical guide. *J. Exp. Bot.* **2000**, *51*, 659–668.

156. Stylinski, C. D.; Gamon, J. a.; Oechel, W. C. Seasonal patterns of reflectance indices, carotenoid pigments and photosynthesis of evergreen chaparral species. *Oecologia* **2002**, *131*, 366–374.

157. Zarco-Tejada, P. J.; Pushnik, J. C.; Dobrowski, S.; Ustin, S. L. Steady-state chlorophyll a fluorescence detection from canopy derivative reflectance and double-peak red-edge effects. *Remote Sens. Environ.* **2003**, *84*, 283–294.

158. Harris, A.; Owen, S. M.; Sleep, D.; Pereira, M. D. G. D. S. Constitutive changes in pigment concentrations: implications for estimating isoprene emissions using the photochemical reflectance index. *Physiol. Plant.* **2015**, n/a-n/a.

159. Ollinger, S. V Sources of variability in canopy reflectance and the convergent properties of plants. *New Phytol.* **2011**, *189*, 375–94.

160. Huete, a.; Didan, K.; Miura, T.; Rodriguez, E. P.; Gao, X.; Ferreira, L. G. Overview of the radiometric and biophysical performance of the MODIS vegetation indices. *Remote Sens. Environ.* **2002**, *83*, 195–213.

161. Wu, C.; Han, X.; Ni, J.; Niu, Z.; Huang, W. Estimation of gross primary production in wheat from in situ measurements. *Int. J. Appl. Earth Obs. Geoinf.* **2010**, *12*, 183–189.

162. Jiang, Z.; Huete, a; Didan, K.; Miura, T. Development of a two-band enhanced vegetation index without a blue band. *Remote Sens. Environ.* **2008**, *112*, 3833–3845.

163. Dong, J.; Xiao, X.; Wagle, P.; Zhang, G.; Zhou, Y.; Jin, C.; Torn, M. S.; Meyers, T. P.; Suyker, A. E.; Wang, J.; Yan, H.; Biradar, C.; Moore, B. Comparison of four EVI-based models for estimating gross primary production of maize and soybean croplands and tallgrass prairie under severe drought. *Remote Sens. Environ.* **2015**, *162*, 154–168.

164. Haboudane, D.; Miller, J. R.; Pattey, E.; Zarco-Tejada, P. J.; Strachan, I. B. Hyperspectral vegetation indices and novel algorithms for predicting green LAI of crop canopies: Modeling and validation in the context of precision agriculture. *Remote Sens. Environ.* **2004**, *90*, 337–352.

165. Van Gaalen, K. E.; Flanagan, L. B.; Peddle, D. R. Photosynthesis, chlorophyll fluorescence and

spectral reflectance in Sphagnum moss at varying water contents. *Oecologia* **2007**, *153*, 19–28.

166. Soudani, K.; Hmimina, G.; Dufrêne, E.; Berveiller, D.; Delpierre, N.; Ourcival, J. M.; Rambal, S.; Joffre, R. Relationships between photochemical reflectance index and light-use efficiency in deciduous and evergreen broadleaf forests. *Remote Sens. Environ.* **2014**, *144*, 73–84.

167. Sims, D. A.; Gamon, J. A. Relationships between leaf pigment content and spectral reflectance across a wide range of species,leaf structures and developmental stages 2002.pdf. **2002**, *81*, 337–354.

168. Gitelson, A.; Merzlyak, M. N. Quantitative estimation of chlorophyll-a using reflectance spectra: Experiments with autumn chestnut and maple leaves. *J. Photochem. Photobiol. B Biol.* **1994**, *22*, 247–252.

169. Gitelson, A. a.; Viña, A.; Ciganda, V.; Rundquist, D. C.; Arkebauer, T. J. Remote estimation of canopy chlorophyll content in crops. *Geophys. Res. Lett.* **2005**, *32*, 1–4.

170. Merzlyak, M. N.; Solovchenko, A. E.; Gitelson, A. a. Reflectance spectral features and non-destructive estimation of chlorophyll, carotenoid and anthocyanin content in apple fruit. *Postharvest Biol. Technol.* **2003**, *27*, 197–211.

171. Gamon, J. a.; Peñuelas, J.; Field, C. B. A narrow-waveband spectral index that tracks diurnal changes in photosynthetic efficiency. *Remote Sens. Environ.* **1992**, *41*, 35–44.

172. Pötzelsberger, E.; Wolfslehner, B.; Hasenauer, H. Climate change impacts on key forest functions of the Vienna Woods. *Eur. J. For. Res.* **2015**, 481–496.

173. Knapp, A. K.; Fay, P. A.; Blair, J. M.; Collins, S. L.; Smith, M. D.; Carlisle, J. D.; Harper, C. W.; Danner, B. T.; Lett, M. S.; Mccarron, J. K. Rainfall Variability , Carbon Cycling , and Plant Species Diversity in a Mesic Grassland. *Science (80-.).* **2002**, *298*, 2202–2206.

174. Scartazza, A.; Mata, C.; Matteucci, G.; Yakir, D.; Moscatello, S.; Brugnoli, E. Comparisons of δ13 C of photosynthetic products and ecosystem respiratory CO2 and their responses to seasonal climate variability. *Oecologia* **2004**, *140*, 340–351.

175. Aubinet, M.; Grelle, A.; Ibrom, Andreas; Rannik, U.; Noncrieff, J.; Foken, T.; Kowalski, A.S.; Martin, P.H.; Berbigier, P.; Bernhofer, C.; Clement, R.; Elbers, J.; Granier, A.; Grunwald, T.; Morgenstern, K.; Pilegaard, K.; Rebmann, C.; Snijders, W.; Valen, R. Estimates of the annual net Carbon and Water Exchange of Forests- The EUROFLUX Methodology. *Adv. Ecol. Res.* **2000**, *30*, 113–175.

176. Matteucci, G.; Masci, A.; Valentini, R.; Scarascia, G. The response of forests to global change:

measurements and modelling simulations in a mountain forest of the Mediterranean region. In *Scientific Tools and Research Needs for Multifunctional Mediterranean Forest Ecosystem Management*; Palahi, M.; Byrot, Y.; Rois, M., Eds.; EFI Proceedings: Joensuu, Finland, 2007; pp. 11–23.

177. Chiti, T.; Papale, D.; Smith, P.; Dalmonech, D.; Matteucci, G.; Yeluripati, J.; Rodeghiero, M.; Valentini, R. Predicting changes in soil organic carbon in mediterranean and alpine forests during the Kyoto Protocol commitment periods using the CENTURY model. *Soil Use Manag.* **2010**, *26*, 475–484.

178. Scartazza, A.; Di Baccio, D.; Bertolotto, P.; Gavrichkova, O.; Matteucci, G. Investigating the European beech (Fagus sylvatica L.) leaf characteristics along the vertical canopy profile: leaf structure, photosynthetic capacity, light energy dissipation and photoprotection mechanisms. *Tree Physiol.* **2016**, *36*, 1060–1076.

179. Guidolotti, G.; Rey, A.; D'andrea, E.; Matteucci, G.; De Angelis, P. Effect of environmental variables and stand structure on ecosystem respiration components in a Mediterranean beech forest. *Tree Physiol.* **2013**, *33*, 960–972.

180. Scartazza, A.; Moscatello, S.; Matteucci, G.; Battistelli, A.; Brugnoli, E. Seasonal and inter-annual dynamics of growth, non-structural carbohydrates and C stable isotopes in a Mediterranean beech forest. *Tree Physiol.* **2013**, *33*, 730–742.

181. Mazzenga, F. Analisi di lungo termine sui fattori di controllo dello scambio di carbonio in una faggeta dell' Italia centromeridionale, Università della Tuscia, 2016.

182. Scartazza, A.; Baccio, D. Di; Bertolotto, P.; Gavrichkova, O.; Matteucci, G. Investigating the European beech (Fagus sylvatica L .) leaf characteristics along the vertical canopy profile : leaf structure , photosynthetic capacity , light energy dissipation and photoprotection mechanisms. **2016**, 1–17.

183. Aubinet, M.; Grelle, A.; Ibrom, A.; Rannik, Ü.; Moncrieff, J.; Foken, T.; Kowalski, A. S.; Martin, P. H.; Berbigier, P.; Bernhofer, C.; Clement, R.; Elbers, J.; Granier, A.; Grünwald, T.; Morgenstern, K.; Pilegaard, K.; Rebmann, C.; Snijders, W.; Valentini, R.; Vesala, T. Estimates of the Annual Net Carbon and Water Exchange of Forests: The EUROFLUX Methodology. *Adv. Ecol. Res.* **1999**, *30*, 113–175.

184. Jordan, C. F. Derivation of Leaf-Area Index from Quality of Light on the Forest Floor. *Ecology* **1969**, *50*, 663–666.

185. Tucker, C. J. Red and photographic infrared linear combinations for monitoring vegetation. *Remote Sens. Environ.* **1979**, *8*, 127–150.

186. Rondeaux, G.; Steven, M.; Baret, F. Optimization of soil-adjusted vegetation indices. *Remote Sens. Environ.* **1996**, *55*, 95–107.

187. Gitelson, A. a Wide Dynamic Range Vegetation Index for remote quantification of biophysical characteristics of vegetation. *J. Plant Physiol.* **2004**, *161*, 165–173.

188. Zarco-Tejada, P. J.; Miller, J. R.; Noland, T. L.; Mohammed, G. H.; Sampson, P. H. Scaling-up and model inversion methods with narrowband optical indices for chlorophyll content estimation in closed forest canopies with hyperspectral data. *IEEE Trans. Geosci. Remote Sens.* **2001**, *39*, 1491–1507.

189. Gitelson, A.; Merzlyak, M. N. Remote estimation of chlorophyll content in higher plant leaves. *Int. J. Remote Sens.* **1997**, *18*, 2691–2697.

190. Gitelson, A. A.; Kaufman, Y. J.; Merzlyak, M. N. Use of a green channel in remote sensing of global vegetation from EOS-MODIS. *Remote Sens. Environ.* **1996**, *58*, 289–298.

191. Gitelson, A. a. Remote estimation of leaf area index and green leaf biomass in maize canopies. *Geophys. Res. Lett.* **2003**, *30*, 4–7.

192. Haboudane, D.; Miller, J. R.; Tremblay, N.; Zarco-Tejada, P. J.; Dextraze, L. Integrated narrow-band vegetation indices for prediction of crop chlorophyll content for application to precision agriculture. *Remote Sens. Environ.* **2002**, *81*, 416–426.

193. Dash, J.; Curran, P. J. The MERIS terrestrial chlorophyll index The MERIS terrestrial chlorophyll index. *Int. J. Remote Sens.* **2004**, *25*, 5403–5413.

194. Datt, B. A New Reflectance Index for Remote Sensing of Chlorophyll Content in Higher Plants: Tests using Eucalyptus Leaves. *J. Plant Physiol.* **1999**, *154*, 30–36.

195. Blackburn, G. A. Spectral indices for estimating photosynthethic pigment concentrations : a test using senescent tree leaves. *Int. J. Remote Sens.* **1998**, *19*, 657–675.

196. Merzlyak, M. N.; Gitelson, A. a; Chivkunova, O. B.; Rakitin, V. Y. U. Non-destructive optical detection of pigment changes during leaf senescence and fruit ripening. *Physiol. Plant.* **1999**, *106*, 135–141.

197. Penuelas, J.; Pinol, J.; Ogaya, R.; Filella, I. Estimation of plant water concentration by the

reflectance Water Index WI (R900/R970). *Int. J. Remote Sens.* **1997**, *18*, 2869–2875.

198. Castagna, A.; Di Baccio, D.; Tognetti, R.; Ranieri, A.; Sebastiani, L. Differential ozone sensitivity interferes with cadmium stress in poplar clones. *Biol. Plant.* **2013**, *57*, 313–324.

199. Di Baccio, D.; Castagna, A.; Tognetti, R.; Ranieri, A.; Sebastiani, L. Early responses to cadmium of two poplar clones that differ in stress tolerance. *J. Plant Physiol.* **2014**, *171*, 1693–1705.

200. Wellburn, A. The spectral determination of chlorophyll a and chlorophyll b, as well as total carotenoids, using various solvents with spectrophotometers of different resolution. *J. Plant Physiol.* **1994**, *144*, 307–313.

201. Zhang, C. J.; Chen, G. X.; Gao, X. X.; Chu, C. J. Photosynthetic decline in flag leaves of two field-grown spring wheat cultivars with different senescence properties. *South African J. Bot.* **2006**, *72*, 15–23.

202. Ruban, A. V. Evolution under the sun: Optimizing light harvesting in photosynthesis. *J. Exp. Bot.* **2015**, *66*, 7–23.

203. Maina, J. N.; Wang, Q. Seasonal Response of Chlorophyll a/b Ratio to Stress in a Typical Desert Species: Haloxylon ammodendron. *Arid L. Res. Manag.* **2015**, *29*, 321–334.

204. Kitajima, K.; Hogan, K. P. Increases of chlorophyll a / b ratios during acclimation of tropical woody s ... Increases of chlorophyll a / b ratios during acclimation of tropical woody s ... *Plant Cell Environ.* **2003**, *26*, 857–865.

205. Dall’Osto, L.; Lico, C.; Alric, J.; Giuliano, G.; Havaux, M.; Bassi, R. Lutein is needed for efficient chlorophyll triplet quenching in the major LHCII antenna complex of higher plants and effective photoprotection in vivo under strong light. *BMC Plant Biol.* **2006**, *6*, 32.

206. Junker, L. V.; Ensminger, I. Relationship between leaf optical properties, chlorophyll fluorescence and pigment changes in senescing Acer saccharum leaves. *Tree Physiol.* **2016**, *36*, 694–711.

207. Yamamoto, H. Y.; Bassi, R. Carotenoids: localization and function. In *Advances in photosynthesis—oxygenic photosynthesis: the light reactions.*; Ort, D.; Yocum, C., Eds.; Kluwer Academic Publishers: Dordrecht, The Netherlands, 1996; Vol. 4, p. 1996.

208. Demmig-Adams, B.; Adams, W. W. Photoprotection in an ecological context: The remarkable complexity of thermal energy dissipation. *New Phytol.* **2006**, *172*, 11–21.

209. Tanaka, Y.; Sasaki, N.; Ohmiya, A. Biosynthesis of plant pigments: Anthocyanins, betalains and carotenoids. *Plant J.* **2008**, *54*, 733–749.

210. Rabhi, M.; Castagna, A.; Remorini, D.; Scattino, C.; Smaoui, A.; Ranieri, A.; Abdelly, C. Photosynthetic responses to salinity in two obligate halophytes: Sesuvium portulacastrum and Tecticornia indica. *South African J. Bot.* **2012**, *79*, 39–47.

211. Baroli, I.; Niyogi, K. K. Molecular genetics of xanthophyll-dependent photoprotection in green algae and plants. *Philos. Trans. R. Soc. Lond. B. Biol. Sci.* **2000**, *355*, 1385–1394.

212. Murthy, K. N. C.; Vanitha, A.; Rajesha, J.; Swamy, M. M.; Sowmya, P. R.; Ravishankar, G. A. In vivo antioxidant activity of carotenoids from Dunaliella salina - A green microalga. *Life Sci.* **2005**, *76*, 1381–1390.

213. Inoue, Y.; Peñuelas, J.; Miyata, A.; Mano, M. Normalized difference spectral indices for estimating photosynthetic efficiency and capacity at a canopy scale derived from hyperspectral and CO2 flux measurements in rice. *Remote Sens. Environ.* **2008**, *112*, 156–172.

214. Sims, D.; Luo, H.; Hastings, S.; Oechel, W.; Rahman, A.; Gamon, J. Parallel adjustments in vegetation greenness and ecosystem CO2 exchange in response to drought in a Southern California chaparral ecosystem. *Remote Sens. Environ.* **2006**, *103*, 289–303.

215. Xiao, X.; Zhang, Q.; Braswell, B.; Urbanski, S.; Boles, S.; Wofsy, S.; Moore, B.; Ojima, D. Modeling gross primary production of temperate deciduous broadleaf forest using satellite images and climate data. *Remote Sens. Environ.* **2004**, *91*, 256–270.

216. Nakaji, T.; Ide, R.; Oguma, H.; Saigusa, N.; Fujinuma, Y. Utility of spectral vegetation index for estimation of gross CO2 flux under varied sky conditions. *Remote Sens. Environ.* **2007**, *109*, 274–284.

217. Vescovo, L.; Wohlfahrt, G.; Balzarolo, M.; Pilloni, S.; Sottocornola, M.; Rodeghiero, M.; Gianelle, D. New spectral vegetation indices based on the near-infrared shoulder wavelengths for remote detection of grassland phytomass. *Int. J. Remote Sens.* **2012**, *33*, 37–41.

218. Mutanga, O.; Skidmore, A. K. Narrow band vegetation indices overcome the saturation problem in biomass estimation. *Int. J. Remote Sens.* **2004**, *25*, 3999–4014.

219. Wu, C.; Niu, Z.; Tang, Q.; Huang, W. Estimating chlorophyll content from hyperspectral vegetation indices: Modeling and validation. *Agric. For. Meteorol.* **2008**, *148*, 1230–1241.

220. Gitelson, A. A.; Merzlyak, M. N. Signature Analysis of Leaf Reflectance Spectra: Algorithm

Development for Remote Sensing of Chlorophyll. *J. Plant Physiol.* 1996, *148*, 494–500.

221. Gitelson, A.; Buschmann, C.; Lichtenthaler, H. The Chlorophyll Fluorescence Ratio F 735/ F 700 as an Accurate Measure of the Chlorophyll Content in Plants. *Remote Sens. Environ.* **1999**, *69*, 296–302.

222. Zarco-Tejada, P. J.; Miller, J. R.; Morales, a.; Berjón, a.; Agüera, J. Hyperspectral indices and model simulation for chlorophyll estimation in open-canopy tree crops. *Remote Sens. Environ.* **2004**, *90*, 463–476.

223. Steele, M.; Gitelson, A.; Rundquist, D. Nondestructive estimation of leaf chlorophyll content in grapes. *Am. J. Enol. Vitic.* **2008**, *59*, 299–305.

224. Main, R.; Azong, M.; Mathieu, R.; Kennedy, M. M. O.; Ramoelo, A.; Koch, S. ISPRS Journal of Photogrammetry and Remote Sensing An investigation into robust spectral indices for leaf chlorophyll estimation. *ISPRS J. Photogramm. Remote Sens.* **2011**, *66*, 751–761.

225. Strachan, I. B.; Pattey, E.; Boisvert, J. B. Impact of nitrogen and environmental conditions on corn as detected by hyperspectral reflectance. *Remote Sens. Environ.* **2002**, *80*, 213–224.

226. Clevers, J. G. P. W.; Kooistra, L. Using Hyperspectral Remote Sensing Data for Retrieving Canopy Chlorophyll and Nitrogen Content. *IEEE J. Sel. Top. Appl. Earth Obs. Remote Sens.* **2012**, *5*, 574–583.

227. Schlemmer, M.; Gitelson, A.; Schepers, J.; Ferguson, R.; Peng, Y.; Shanahan, J.; Rundquist, D. Remote estimation of nitrogen and chlorophyll contents in maize at leaf and canopy levels. *Int. J. Appl. Earth Obs. Geoinf.* **2013**, *25*, 47–54.

228. Perez-Priego, O.; Guan, J.; Rossini, M.; Fava, F.; Wutzler, T.; Moreno, G.; Carvalhais, N.; Carrara, a.; Kolle, O.; Julitta, T.; Schrumpf, M.; Reichstein, M.; Migliavacca, M. Sun-induced Chlorophyll fluorescence and PRI improve remote sensing GPP estimates under varying nutrient availability in a typical Mediterranean savanna ecosystem. *Biogeosciences Discuss.* **2015**, *12*, 11891–11934.

229. Demming-Adams, B.; Adams, W. W. The role of xanthophyll cycle carotenoids in the protection of photosynthesis. *Trends Plant Sci.* **1996**, *1*, 21–26.

230. Wong, C. Y. S.; Gamon, J. A. The photochemical reflectance index provides an optical indicator of spring photosynthetic activation in evergreen conifers. **2015**.

231. Wong, C. Y. S.; Gamon, J. A. Three causes of variation in the photochemical reflectance index

(PRI) in evergreen conifers. **2015**, 187–195.

232. Gitelson, A. A.; Gamon, J. A.; Solovchenko, A. Multiple drivers of seasonal change in PRI : Implications for photosynthesis 1 . Leaf level. *Remote Sens. Environ.* **2017**, *191*, 110–116.

233. Solovchenko, A. *Photoprotection in Plants: Optical Screening-Based Mechanisms.*; 1st ed.; Springer-Verlag Berlin Heidelberg: New York, 2010.

234. Hernández-Clemente, R.; Navarro-Cerrillo, R. M.; Zarco-Tejada, P. J. Carotenoid content estimation in a heterogeneous conifer forest using narrow-band indices and PROSPECT+DART simulations. *Remote Sens. Environ.* **2012**, *127*, 298–315.

235. GTOS 52. *Terrestrial Essential Climate Variables for climate change assessment, mitigation and adaptation*; Food and Agriculture Organization, United Nations: Rome, Italy, 2008.

236. Gobron, N.; Verstraete, M. M. *ECV T10: Fraction of Absorbed Photosynthetically Active Radiation (FAPAR)*; Food and Agriculture Organization, United Nations: Rome, Italy, 2009.

237. Weiss, M.; Baret, F. fAPAR (fraction of Absorbed Photosynthetically Active Radiation) estimates at various scale. *34th Int. Symp. Remote Sens. Environ.* **2011**.

238. Weiss, M.; Baret, F.; Garrigues, S.; Lacaze, R. LAI and fAPAR CYCLOPES global products derived from VEGETATION. Part 2: validation and comparison with MODIS collection 4 products. *Remote Sens. Environ.* **2007**, *110*, 317–331.

239. Asner, G. P.; Wessman, C. A.; Archer, S. Scale Dependence of Absorption of Photosynthetically Active Radiation in Terrestrial Ecosystems. *Ecol. Appl.* **1998**, *8*, 1003–1021.

240. Gobron, N.; Pinty, B.; Taberner, M.; Mélin, F.; Verstraete, M. M.; Widlowski, J. L. Monitoring the photosynthetic activity of vegetation from remote sensing data. *Adv. Sp. Res.* **2006**, *38*, 2196–2202.

241. Gond, V.; De Pury, D. G. G.; Veroustraete, F.; Ceulemans, R. Seasonal variations in leaf area index, leaf chlorophyll, and water content; scaling-up to estimate fAPAR and carbon balance in a multilayer, multispecies temperate forest. *Tree Physiol.* **1999**, *19*, 673–679.

242. Gobron, N.; Pinty, B.; Mélin, F.; Taberner, M.; Verstraete, M. M.; Belward, A.; Lavergne, T.; Widlowski, J. L. The state of vegetation in Europe following the 2003 drought. *Int. J. Remote Sens.* **2005**, 2013–2020.

243. Senna, M. C. a. Fraction of photosynthetically active radiation absorbed by Amazon tropical

forest: A comparison of field measurements, modeling, and remote sensing. *J. Geophys. Res.* **2005**, *110*, 1–8.

244. Jung M, Verstraete M, Gobron N, Reichstein M, Papale D, Bondeau A, Robustelli M, P. B. Diagnostic assessment of European gross primary production. *Glob. Chang. Biol.* **2008**, 2349–2364.

245. Seixas, J.; Carvalhais, N.; Nunes, C.; Benali, A. Comparative analysis of MODIS-FAPAR and MERIS-MGVI datasets: Potential impacts on ecosystem modeling. *Remote Sens. Environ.* **2009**, *113*, 2547–2559.

246. Hanan, N. P.; Bégué, A. A method to estimate instantaneous and daily intercepted photosynthetically active radiation using a hemispherical sensor. *Agric. an For. Meteorol.* **1995**, *74*.

247. Widlowski, J. L. On the bias of instantaneous FAPAR estimates in open-canopy forests. *Agric. For. Meteorol.* **2011**, *1501–1522*.

248. Xiao, X.; Zhang, Q.; Hollinger, D.; Aber, J.; Moore III, B. Modelling gross primary production of an evergreen needleleaf forest using modis and climate data. *Ecol. Appl.* **2005**, *15*, 954–969.

249. Myneni, R. B.; Hoffman, S.; Knyazikhin, Y.; Privette, J. L.; Glassy, J.; Tian, Y.; Wang, Y.; Song, X.; Zhang, Y.; Smith, G. R.; Lotsch, a.; Friedl, M.; Morisette, J. T.; Votava, P.; Nemani, R. R.; Running, S. W. Global products of vegetation leaf area and fraction absorbed PAR from year one of MODIS data. *Remote Sens. Environ.* **2002**, *83*, 214–231.

250. Zhang, Q.; Xiao, X.; Braswell, B.; Linder, E.; Baret, F.; Moore, B. Estimating light absorption by chlorophyll, leaf and canopy in a deciduous broadleaf forest using MODIS data and a radiative transfer model. *Remote Sens. Environ.* **2005**, *99*, 357–371.

251. Knyazikhin, Y.; Martonchik, J. V.; Myneni, R. B.; Diner, D. J.; Running, S. W. Synergistic algorithm for estimating vegetation canopy leaf area index and fraction of absorbed photosynthetically active radiation from MODIS and MISR data. *J. Geophys. Res.* **1998**, *103*, 32257–32276.

252. Gobron, N.; Pinty, B.; Aussedat, O.; Chen, J. M.; Cohen, W. B.; Fensholt, R.; Gond, V.; Huemmrich, K. F.; Lavergne, T.; Mélin, F.; Privette, J. L.; Sandholt, I.; Taberner, M.; Turner, D. P.; Verstraete, M. M.; Widlowski, J. L. Evaluation of fraction of absorbed photosynthetically active radiation products for different canopy radiation transfer regimes: Methodology and results using Joint Research Center products derived from SeaWiFS against ground-based estimations. *J. Geophys. Res. Atmos.* **2006**, *111*, 1–15.

253. Plummer, S.; Arino, O.; Simon, M.; Steffen, W. Establishing a earth observation product service for the terrestrial carbon community: The globcarbon initiative. *Mitig. Adapt. Strateg. Glob. Chang.* **2006**, *11*, 97–111.

254. Pinty, B.; Lavergne, T.; Voßbeck, M.; Kaminski, T.; Aussedat, O.; Giering, R.; Gobron, N.; Taberner, M.; Verstraete, M. M.; Widlowski, J. L. Retrieving surface parameters for climate models from Moderate Resolution Imaging Spectroradiometer (MODIS)-Multiangle Imaging Spectroradiometer (MISR) albedo products. *J. Geophys. Res. Atmos.* **2007**, *112*, 1–23.

255. Baret, F.; Hagolle, O.; Geiger, B.; Bicheron, P.; Miras, B.; Huc, M.; Berthelot, B.; Niño, F.; Weiss, M.; Samain, O.; Roujean, J. L.; Leroy, M. LAI, fAPAR and fCover CYCLOPES global products derived from VEGETATION. Part 1: Principles of the algorithm. *Remote Sens. Environ.* **2007**, *110*, 275–286.

256. Donohue, R. J.; Roderick, M. L.; McVicar, T. R. Deriving consistent long-term vegetation information from AVHRR reflectance data using a cover-triangle-based framework. *Remote Sens. Environ.* **2008**, *112*, 2938–2949.

257. Baret, F.; Weiss, M.; Lacaze, R.; Camacho, F.; Makhmara, H.; Pacholcyzk, P.; Smets, B. GEOV1: LAI and FAPAR essential climate variables and FCOVER global time series capitalizing over existing products. Part1: Principles of development and production. *Remote Sens. Environ.* **2013**, *137*, 299–309.

258. Camacho, F.; Cernicharo, J.; Lacaze, R.; Baret, F.; Weiss, M. GEOV1: LAI, FAPAR essential climate variables and FCOVER global time series capitalizing over existing products. Part 2: Validation and intercomparison with reference products. *Remote Sens. Environ.* **2013**, *137*, 310–329.

259. Yang, W.; Tan, B.; Huang, D.; Rautiainen, M.; Shabanov, N. V.; Wang, Y.; Privette, J. L.; Huemmrich, K. F.; Fensholt, R.; Sandholt, I.; Weiss, M.; Ahl, D. E.; Gower, S. T.; Nemani, R. R.; Knyazikhin, Y.; Myneni, R. B. MODIS leaf area index products: From validation to algorithm improvement. *IEEE Trans. Geosci. Remote Sens.* **2006**, *44*, 1885–1896.

260. Martínez, B.; Camacho, F.; Verger, A.; García-haro, F. J.; Gilabert, M. A. Intercomparison and quality assessment of MERIS , MODIS and SEVIRI FAPAR products over the Iberian Peninsula. *Int. J. Appl. Earth Obs. Geoinf.* **2013**, *21*, 463–476.

261. Pickett-Heaps, C. A.; Canadell, J. G.; Briggs, P. R.; Gobron, N.; Haverd, V.; Paget, M. J.; Pinty, B.; Raupach, M. R. Evaluation of six satellite-derived Fraction of Absorbed Photosynthetic Active Radiation (FAPAR) products across the Australian continent. *Remote Sens. Environ.* **2014**, *140*, 241–

256.

262. McCallum, A.; Wagner, W.; Schmullius, C.; Shvidenko, A.; Obersteiner, M.; Fritz, S.; Nilsson, S. Comparison of four global FAPAR datasets over Northern Eurasia for the year 2000. *Remote Sens. Environ.* **2010**, *114*.

263. Yan, K.; Park, T.; Yan, G.; Chen, C.; Yang, B.; Liu, Z.; Nemani, R.; Knyazikhin, Y.; Myneni, R. Evaluation of MODIS LAI/FPAR Product Collection 6. Part 1: Consistency and Improvements. *Remote Sens.* **2016**, *8*, 359.

264. Yan, K.; Park, T.; Yan, G.; Liu, Z.; Yang, B.; Chen, C.; Nemani, R.; Knyazikhin, Y.; Myneni, R. Evaluation of MODIS LAI/FPAR Product Collection 6. Part 2: Validation and Intercomparison. *Remote Sens.* **2016**, *8*, 460.

265. D'Odorico, P.; Gonsamo, A.; Pinty, B.; Gobron, N.; Coops, N.; Mendez, E.; Schaepman, M. E. Intercomparison of fraction of absorbed photosynthetically active radiation products derived from satellite data over Europe. *Remote Sens. Environ.* **2014**, *142*, 141–154.

266. Majasalmi, T.; Rautiainen, M.; Stenberg, P.; Manninen, T. Validation of MODIS and GEOV1 fPAR products in a boreal forest site in Finland. *Remote Sens.* **2015**, *7*, 1359–1379.

267. Tao, X.; Liang, S.; Wang, D. Assessment of five global satellite products of fraction of absorbed photosynthetically active radiation: Intercomparison and direct validation against ground-based data. *Remote Sens. Environ.* **2015**, *163*, 270–285.

268. Weiss, M.; Baret, F.; Block, T.; Koetz, B.; Burini, A.; Scholze, B.; Lecharpentier, P.; Brockmann, C.; Fernandes, R.; Plummer, S.; Myneni, R.; Gobron, N.; Nightingale, J.; Schaepman-Strub, G.; Camacho, F.; Sanchez-Azofeifa, A. On line validation exercise (OLIVE): A web based service for the validation of medium resolution land products. application to FAPAR products. *Remote Sens.* **2014**, *6*, 4190–4216.

269. Morisette, J. T.; Baret, F.; Privette, J. L.; Myneni, R. B.; Nickeson, J.; Garrigues, S.; Shabanov, N.; Weiss, M.; Fernandes, R.; Leblanc, S.; Kalacska, M.; Sánchez-azofeifa, G. A.; Chubey, M.; Rivard, B.; Stenberg, P.; Rautiainen, M.; Voipio, P.; Manninen, T.; Pilant, A. N.; Lewis, T. E.; Iiames, J. S.; Colombo, R.; Meroni, M.; Busetto, L.; Cohen, W.; Turner, D. P.; Warner, E. D.; Petersen, G. W.; Seufert, G.; Cook, R. Validation of Global Moderate-Resolution LAI Products: A Framework Proposed Within the CEOS Land Product Validation Subgroup. *IEEE Trans. Geosci. Remote Sens.* **2006**, *44*, 1–14.

270. GCOS. *Systematic Observation Requirements For Satellite-Based Data Products for Climate -*

2011 Update; Geneva, Switzerland, 2011.

271. VITO Gio Global Land Component - Lot I “Operation of the G Lobal Land Component” 2014, 88.

272. Hagolle, O.; Lobo, A.; Maisongrande, P.; Cabot, F.; Duchemin, B.; De Pereyra, A. Quality assessment and improvement of temporally composited products of remotely sensed imagery by combination of VEGETATION 1 and 2 images. *Remote Sens. Environ.* **2005**, *94,* 172–186.

273. Vermote, E. F.; Tanrè, D.; Deuzè, J. L.; Herman, M.; Morcrette, J.-J. Second Simulation of the Satellite Signal in the Solar Spectrum , 6s : An Overview. *IEEE Trans. Geosci. Remote Sens.* **1997**, *35*, 675–686.

274. Apogee Instruments Inc. Owner’s Manual. Apogee Instruments. Quantum sensor (Models SQ-110 and SQ-300 Series) 2016, 1–17.

275. Weiss, M.; Baret, F.; De Solan, B.; Hemmerlé, M. Monitoring Plant Area Index at ground level: PAI autonomous system from transmittance sensors (PASTIS). In *Fourth Recent Advances in Quantitative Remote Sensing*; Sobrino, J. A., Ed.; Publicacions de la Universitat de València: València, Spain, 2014.

276. Weiss, M.; Baret, F. *Can-eye V 6.1 User Manual*; Avignon, France, 2010.

277. Weiss, M.; Baret, F.; Smith, G. J.; Jonckheere, I.; Coppin, P. Review of methods for in situ leaf area index (LAI) determination. *Agric. For. Meteorol.* **2004**, *121,* 37–53.

278. Liang, S., Li, X., & Wang, J. Fraction of absorbed photosynthetically active radiation by green vegetation. In *Advanced remote sensing: Terrestrial information extraction and applications*; Elsevier Inc.: Oxford, UK, 2012; pp. 383–414.

279. Wang, Y.; Xie, D.; Liu, S.; Hu, R.; Li, Y.; Yan, G. Scaling of FAPAR from the Field to the Satellite. *Remote Sens.* **2016**, *8*, 310.

280. Zhang, Q.; Middleton, E. M.; Cheng, Y. Ben; Landis, D. R. Variations of foliage chlorophyll fAPAR and foliage non-chlorophyll fAPAR (fAPARchl, fAPARnonchl) at the Harvard Forest. *IEEE J. Sel. Top. Appl. Earth Obs. Remote Sens.* **2013**, *6,* 2254–2264.

281. Jonckheere, I.; Fleck, S.; Nackaerts, K.; Muys, B.; Coppin, P.; Weiss, M.; Baret, F. Review of methods for in situ leaf area index determination Part I. Theories, sensors and hemispherical photography. *Agric. For. Meteorol.* **2004**, *121,* 19–35.

282. Andrieu, B.; Baret, F. Indirect methods of estimating crop structure from optical measurements. In *Crop Structure and Light Microclimate—Characterization and Applications*; Varlet-Grancher, R.B.C., Sinoquet, H., Ed.; INRA: Paris, France, 1993; pp. 285–322.

283. Weiss, M. CAN-EYE Output Variables. Definitions and theoretical background. 1. 2. https://www4.paca.inra.fr/can-eye/Documentation- Publications/Documentation (accessed Nov 13, 2016).

284. Martínez, B.; García-Haro, F. J.; Camacho-de Coca, F. Derivation of high-resolution leaf area index maps in support of validation activities: Application to the cropland Barrax site. *Agric. For. Meteorol.* **2009**, *149*, 130–145.

285. Goward, S. N.; Huemmrich, K. F. Vegetation canopy PAR absorptance and the normalized difference vegetation index - An assessment using the SAIL model. *Remote Sens. Environ.* **1992**, *39*, 119–140.

286. Nestola, E.; Calfapietra, C.; Emmerton, C.; Wong, C.; Thayer, D.; Gamon, J. Monitoring Grassland Seasonal Carbon Dynamics, by Integrating MODIS NDVI, Proximal Optical Sampling, and Eddy Covariance Measurements. *Remote Sens.* **2016**, *8*, 260.

287. Fensholt, R.; Sandholt, I.; Rasmussen, M. S. Evaluation of MODIS LAI, fAPAR and the relation between fAPAR and NDVI in a semi-arid environment using in situ measurements. *Remote Sens. Environ.* **2004**, *91*, 490–507.

288. Ronchetti, E.; Field, C.; Blanchard, W. Robust linear model selection by cross-validation. *J. Am. Stat. Assoc.* **1997**, *92*, 1017–1023.

289. Latorre, C. Vegetation Field Data and Production of Ground-Based Maps : “Collelongo site - Selvapiana, Italy” 8th July and 25th September, 2015. http://fp7-imagines.eu/media/Documents (accessed Sep 13, 2016).

290. Mira, M.; Weiss, M.; Baret, F.; Courault, D.; Hagolle, O.; Gallego-Elvira, B.; Olioso, A. The MODIS (collection V006) BRDF/albedo product MCD43D: Temporal course evaluated over agricultural landscape. *Remote Sens. Environ.* **2015**, *170*, 216–228.

291. Schowengerdt, R. A. *Remote Sensing: Models and Methods for Image Processing*; 3rd ed.; Academic Press: San Diego, 2007.

292. Duveiller, G.; Baret, F.; Defourny, P. Crop specific green area index retrieval from MODIS data at regional scale by controlling pixel-target adequacy. *Remote Sens. Environ.* **2011**, *115*, 2686–2701.

293. Fernandes, R.; Plummer, S.; Nightingale, J.; Baret, F.; Camacho, F.; Fang, H.; Garrigues, S.; Gobron, N.; Lang, M.; Lacaze, R.; LeBlanc, S.; Meroni, M.; Martinez, B.; Nilson, T.; Pinty, B.; Pisek, J.; Sonnentag, O.; Verger, A.; Welles, J.; Weiss, M.; Widlowski, J. L. Global Leaf Area Index Product Validation Good Practices. In *Best Practice for Satellite-Derived Land Product Validation. Land Product Validation Subgroup (WGCV/CEOS)*; Schaepman-Strub, G.; Román, M.; Nickeson, J., Eds.; CEOS: Zurich, Switzerland, 2014; pp. 1–78.

294. Harper, W. V. Reduced major axis regression: Teaching alternatives to least squares. In *Sustainability in statistics education. Proceedings of the Ninth International Conference on Teaching Statistics (ICOTS9, July, 2014), Flagstaff, Arizona, USA*; Makar, K.; De Sousa, B.; Gould, R., Eds.; Voorburg, The Netherlands: International Statistical Instutute: Flagstaff, Arizona,USA, 2014; pp. 1–4.

295. Camacho, F.; Lacaze, R.; Latorre, C.; Baret, F.; De la Cruz, F.; Demarez, V.; Di Bella, C.; Fang, H.; García-Haro, J.; Gonzalez, M. P.; Kussul, N.; Lopez-Baeza, E.; Mattar, C.; Nestola, E.; Pattey, E.; Piccard, I.; Rudiger, C.; Savin, I.; Sanchez-Azofeifa, A.; Boschetti, M.; Bossio, D.; Weiss, M.; Castrignano, A.; Zribi, M. A Network of Sites for Ground Biophysical Measurements in support of Copernicus Global Land Product Validation. In *Fourth Recent Advances in Quantitative Remote Sensing*; Sobrino, J., Ed.; Publicacions de la Universitat de València: València, Spain, 2014; pp. 1–6.

296. Raymaekers, D.; Garcia, A.; Di Bella, C.; Beget, M. E.; Llavallol, C.; Oricchio, P.; Straschnoy, J.; Weiss, M.; Baret, F. SPOT-VEGETATION GEOV1 biophysical parameters in semi-arid agro-ecosystems. *Int. J. Remote Sens.* **2014**, *35*, 2534–2547.

297. Brunet, J.; Fritz, Ö.; Richnau, G. Biodiversity in European beech forests – a review with recommendations for sustainable forest management. *Ecol. Bull.* **2010**, *53*, 77–94.

298. Cohen, W. B.; Maiersperger, T. K.; Gower, S. T.; Turner, D. P. An improved strategy for regression of biophysical variables and Landsat ETM+ data. *Remote Sens. Environ.* **2003**, *84*, 561–571.